



**Max-Planck-Institut für Metallforschung**  
Stuttgart

---

# **Synthesis and Characterization of Carbon Nanotube-Reinforced Copper Thin Films**

Cornelia Otto

Dissertation  
an der  
**Universität Stuttgart**

---

Bericht Nr. 194  
November 2006

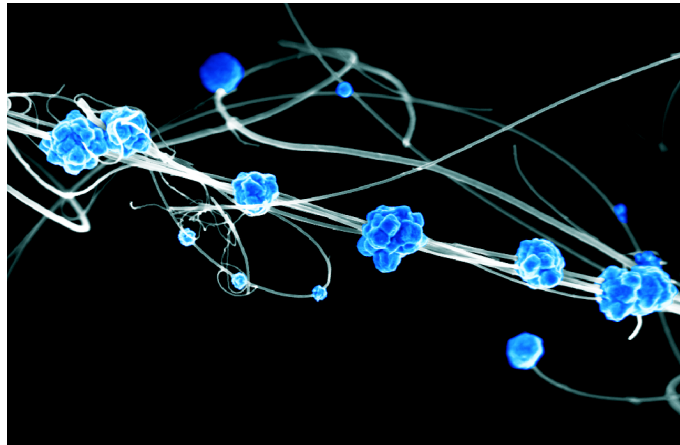




---

Synthesis and Characterization  
of  
Carbon Nanotube-Reinforced Copper Thin Films

---



Von der Fakultät Chemie der Universität Stuttgart  
zur Erlangung der Würde eines Doktors der  
Naturwissenschaften (Dr. rer. nat.) genehmigte Abhandlung

vorgelegt von

**Cornelia Otto**

aus Mühlacker

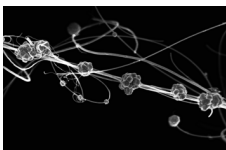
Hauptberichter: Prof. Dr. E. Arzt  
Mitberichter: Prof. Dr. M. Rühle  
Tag der mündlichen Prüfung: 16. November 2006

Max-Planck-Institut für Metallforschung, Stuttgart

2007



## Für Stephan



The cover picture shows carbon nanotubes which had been modified chemically before being used in an electrolysis experiment. In the course of this experiment, carbon from the graphite anode deposited at the modified sites. Scientifically, this experiment turned out to be a dead end, but the samples provided beautiful images, and the image shown here won the 2006 Nano&Arts competition.



# Acknowledgements

A dissertation is too heavy a load for one person alone. Many people have helped me in the course of the past three years and I am much indebted to all of them.

First of all, I want to thank Prof. Eduard Arzt as my advisor and Prof. Manfred Rühle as the chairman of the Graduiertenkolleg which provided my financial support. Without them, this dissertation would not have been possible.

Over the course of my dissertation, four scientists have advised me in all arising problems and provided encouragement and fruitful discussion. I am deeply grateful for all their help. In chronological order, these four were Dr. Nicole Grobert, Dr. John Balk, Dr. Gerhard Dehm and finally Dr. Julie Nucci, who took the longest turn.

The thin films group of the department Arzt was always a good platform for discussing new results. Thank you for listening so patiently to all my nanotubes problems even if they didn't concern your own work.

Dr. Andrei Matveev and his knowledge on electrodeposition were of immeasurable help for the studies on the electrolytically produced samples. Thank you very much.

Dr. Steffen Orso, Dr. Gunther Richter, Ulrike Eigenthaler and Birgit Heiland helped me immensely in making some last-minute samples. With all my heart I appreciate the effort they have made, finding time for my samples at short notice and running late hours. In addition, I want to thank all the technicians who have helped me with their expertise and experience and also Mrs. Hess for all her help in administrative matters.

I want to thank Linda, who has shared my problems and successes since our first day at the university, my office mates Tobi, Petra and Chris, the Max-Planck role playing group and all my colleagues at the department for their friendship and for all the good times we had together.

Finally, I want to thank my parents, my brother and my godfather for their support during the three years of the dissertation and all the time before. But my deepest love and gratefulness goes to my husband Stephan, who has supported me and endured me when the stress got to me. This work is dedicated to him.

# Contents

<b>Contents</b>	<b>9</b>
<b>List of symbols and abbreviations</b>	<b>13</b>
<b>Deutsche Zusammenfassung</b>	<b>15</b>
<b>Abstract</b>	<b>27</b>
<b>1 Introduction</b>	<b>29</b>
<b>2 Literature Review</b>	<b>31</b>
2.1 Carbon nanotubes . . . . .	31
2.1.1 Structure . . . . .	31
2.1.2 Production methods . . . . .	34
2.1.3 Mechanical properties . . . . .	37
2.1.4 Wetting . . . . .	42
2.1.5 Nitrogen doping . . . . .	43
2.2 Composites . . . . .	46
2.2.1 Composite theory . . . . .	46
2.2.2 Composites with CNTs . . . . .	50
2.2.3 Metal matrix composites with CNTs . . . . .	51
2.3 Motivation . . . . .	56
<b>3 Carbon nanotubes in sputtered copper films</b>	<b>59</b>
3.1 Motivation . . . . .	59
3.2 Experimental Procedure . . . . .	60
3.2.1 Synthesis of CNTs . . . . .	60
3.2.2 Parameters for the deposition of the copper layers . . . . .	62
3.2.3 Deposition of nanotubes . . . . .	63

3.2.4	Dispersing nanotubes . . . . .	63
3.2.5	Deposition Methods . . . . .	64
3.3	Results . . . . .	66
3.3.1	Quality of nanotube dispersion . . . . .	67
3.3.2	Conformity . . . . .	67
3.4	Discussion and Outlook . . . . .	71
<b>4</b>	<b>Cu/CN<sub>x</sub> microcolumns: compression testing and TEM analysis</b>	<b>75</b>
4.1	Introduction . . . . .	75
4.2	Experimental procedure . . . . .	78
4.2.1	Preparation of micron-sized columns . . . . .	78
4.2.2	<i>In situ</i> compression testing . . . . .	79
4.2.3	<i>Ex situ</i> compression testing . . . . .	80
4.2.4	Preparation of TEM specimens and TEM analysis . . . . .	81
4.3	Results and discussion . . . . .	82
4.3.1	Stress-strain measurements . . . . .	84
4.3.2	Matrix deformation mechanisms . . . . .	88
4.3.3	Matrix-nanotube interactions . . . . .	94
4.4	Summary and outlook . . . . .	100
<b>5</b>	<b>Preferential deposition of copper on CNTs</b>	<b>105</b>
5.1	Introduction . . . . .	105
5.2	Experimental procedure . . . . .	106
5.2.1	Isolated CN <sub>x</sub> on copper . . . . .	106
5.2.2	Aligned CNT-carpets on non-conductive substrate . . . . .	107
5.2.3	Tangled CNT-carpets on conductive substrate . . . . .	108
5.3	Results . . . . .	108
5.3.1	Isolated CN <sub>x</sub> on copper . . . . .	108
5.3.2	Aligned CNT-carpets on non-conductive substrate . . . . .	109
5.3.3	Tangled CNT-carpets on conductive substrate . . . . .	112
5.4	Discussion . . . . .	115
5.4.1	Samples with isolated CN <sub>x</sub> . . . . .	115
5.4.2	Samples with CNT-carpets . . . . .	115
5.5	Summary and outlook . . . . .	117



---

<b>6</b>	<b>Tensile testing of electrodeposited composite samples</b>	<b>119</b>
6.1	Experimental procedure . . . . .	119
6.1.1	Sample preparation . . . . .	120
6.1.2	Tensile testing and microscopical analysis . . . . .	122
6.2	Results . . . . .	124
6.2.1	Sample appearance . . . . .	124
6.2.2	Density of carbon nanotubes . . . . .	128
6.2.3	Microscopical observations of the fracture site . . . . .	130
6.2.4	Coated and uncoated nanotubes . . . . .	135
6.2.5	Stress-strain measurements . . . . .	137
6.3	Discussion . . . . .	139
6.3.1	Increased fracture resistance in reinforced samples . . . . .	139
6.3.2	Signs of adhesion between nanotubes and matrix . . . . .	141
6.3.3	Implications for further research . . . . .	142
6.4	Summary and Conclusion . . . . .	143
<b>7</b>	<b>Summary and outlook</b>	<b>145</b>
	<b>List of Figures</b>	<b>151</b>
	<b>List of Tables</b>	<b>155</b>
	<b>Bibliography</b>	<b>155</b>



# List of symbols and abbreviations

$\alpha$	tapering angle of microcolumns
$b$	width of electrodeposited tensile test samples at gauge length
$\beta$	proportionality constant between $l_c$ and $l_d$
CNT	carbon nanotubes
CN <sub><i>x</i></sub>	nitrogen-doped carbon nanotube
CVD	Chemical Vapor Deposition
$\bar{d}$	average diameter of nanotubes (in chapter 3)
$\bar{d}$	average diameter of microcolumn (in chapter 4)
$d_f$	fiber diameter
$d_{\text{bottom}}$	diameter at the Si/Cu interface of the microcolumn
$d_{\text{top}}$	diameter at the top of the microcolumn
$E$	Young's modulus
$\varepsilon_c$	strain in the composite
$\varepsilon_{\text{bottom}}$	compressive strain in lower layer of microcolumns
$\varepsilon_{\text{top}}$	compressive strain in upper layer of microcolumns
EDX	Energy Dispersive X-ray spectroscopy
EELS	Electron Energy Loss Spectroscopy
FIB	Focused Ion Beam microscopy
$\Delta G_c$	pull-out work per unit area of fiber
$h$	total height of microcolumns (in chapter 4)
$h$	thickness of electrodeposited Cu samples (in chapter 6)
$h_{\text{bottom}}$	height of lower layer in microcolumns
$h_{\text{top}}$	height of upper layer in microcolumns
HV	High Vacuum
$I_d$	deposition current

---

$\bar{l}$	average length of nanotubes
$l_c$	critical fiber length
$l_d$	debond length
$\Delta m$	mass increase during electrodeposition
MWNT	multi-walled carbon nanotube
PVD	Physical Vapor Deposition
$\rho$	density
RT	room temperature
$\sigma_f(\varepsilon_c)$	stress in the fiber at certain strain in the composite
$\sigma_{\max}$	tensile strength
SDS	sodium dodecyl sulfate
SEM	Scanning Electron Microscopy
SFE	Stacking Fault Energy
SWNT	single-walled carbon nanotube
$\tau_i$	interfacial shear strength
$T_s$	reaction time of CNT synthesis
TEM	Transmission Electron Microscopy
UHV	Ultra High Vacuum
$V_f$	volume fraction of fiber

# Deutsche Zusammenfassung

## Motivation

Kohlenstoffnanoröhrchen (carbon nanotubes - CNTs) sind seit ihrer Entdeckung im Jahr 1991 der Gegenstand von großem wissenschaftlichem Interesse. Ihre außergewöhnlichen Eigenschaften lassen sie als die idealen Verstärkungsfasern für Metallmatrix-Verbundwerkstoffe erscheinen und dies wurde auch schon mehrfach im Experiment bestätigt. Bislang ist jedoch unklar, welche Mechanismen hinter dieser verstärkenden Wirkung stecken und was sich genau im Werkstoff abspielt. Ziel dieser Arbeit war es, einen Modellverbundwerkstoff zu entwickeln, der es erlaubt, diese Fragestellung im Experiment zu untersuchen.

## Literatur

Kohlenstoffnanoröhrchen bestehen aus zusammengerollten Graphitebenen, die an den Enden durch halbkugelige Kappen abgeschlossen werden. Liegt nur eine einzelne solche Röhre vor, spricht man von "single-walled nanotubes" (SWNT), sind mehrere ineinander geschoben, nennt man das "multi-walled nanotubes" (MWNT). Aufgrund der starken Atombindungen in den Graphitebenen und deren perfekte Ausrichtung in den Kohlenstoffnanoröhrchen, zeichnen sich CNTs durch außergewöhnliche mechanische Eigenschaften aus. Die genauen Zahlenwerte für die verschiedenen Eigenschaften sind noch unklar, da die Ergebnisse stark streuen. So finden sich z.B. für den E-Modul Werte zwischen 18 GPa und 4150 GPa. In der Regel geht man jedoch davon aus, dass der E-Modul von CNTs etwa bei 1000 GPa liegt. Auch die Zugfestigkeit ist vergleichbar hoch (ca. 150 GPa). Darüber hinaus zeigen CNTs

aber auch noch eine außergewöhnliche Flexibilität und sind nahezu unzerstörbar in Biegebelastung.

Nach außen hin zeigen Kohlenstoffnanoröhrchen eine fast perfekte Graphitebene, in der alle Atome vollständig abgesättigt sind. Dementsprechend reaktionsträge sind sie. Versuche haben gezeigt, dass sie nur von Flüssigkeiten mit einer Oberflächenspannung von weniger als  $200 \text{ mJ/m}^2$  benetzt werden. Das schließt die Metalle, die üblicherweise in Verbundwerkstoffen verwendet werden, aus. Tatsächlich wurden bis jetzt kaum Benetzungsexperimente mit technisch wichtigen Metallen gemacht. Deswegen muss auf Erfahrungen zurückgegriffen werden, die mit Graphit und konventionellen Kohlefasern gemacht wurden. Demnach sollten CNTs nur von den Metallen benetzt werden, die Carbide bilden können. Kupfer gehört nicht zu diesen Metallen, es sollte also CNTs nicht benetzen und dementsprechend sollte auch die Adhäsion an den Grenzflächen niedrig sein.

Eine Möglichkeit, die perfekte Struktur der Nanoröhrchen aufzubrechen, besteht darin, sie mit Stickstoff zu dotieren. Stickstoff hat ein Valenzelektron mehr als Kohlenstoff. Solchermaßen dotierte Nanoröhrchen zeigen einen bambusartigen Aufbau (Bild 2.8 auf S. 45), und insgesamt eine weniger perfekte Struktur. Diese Defekte können aber auch als Ankerpunkte für die Matrix dienen, und damit Benetzbarkeit und Grenzflächenfestigkeit erhöhen.

Ohne hier genauer auf die Theorie der Verbundwerkstoffe eingehen zu wollen, sollen hier die wichtigsten Anforderung an eine Faser für Metallmatrix-Verbundwerkstoffe kurz aufgeführt werden. Da Metalle von Haus aus recht zäh sind, wird meistens mit dem Ziel der Festigkeitssteigerung verstärkt. Dafür brauchen die Fasern einen hohen E-Modul, sowie hohe Streckgrenze und Zugfestigkeit. All das ist bei CNTs vorhanden. Für eine erfolgreiche Kraftübertragung von der Matrix auf die Faser sind aber noch zwei weitere Dinge von Bedeutung, die Grenzflächenscherfestigkeit, die bereits erwähnt wurde, und das Aspektverhältnis. CNTs haben einen sehr kleinen Durchmesser (ca. 10 - 100 nm), verbunden mit einer recht großen Länge von bis zu 2 mm. Ihr Aspektverhältnis kann demnach bis zu 100.000 betragen, ein Wert, der sonst maximal von Endlosfasern erreicht wird, die aber viel aufwändiger in der Verarbeitung sind.

Von verschiedenen Gruppen wurden in den letzten Jahren Verbundwerkstoffe aus Kohlenstoffnanoröhrchen und verschiedenen Metallen hergestellt. In der Regel zeigte sich eine deutliche Verbesserung der mechanischen Eigenschaften, jedoch bereitet die Herstellung der Proben, und insbesondere die homogene Verteilung der Nanoröhrchen noch große Probleme. Systematische Untersuchungen zu den Verstärkungsmechanismen, die in solchen Verbundwerkstoffen wirksam sind, gibt es keine. Diese Fragestellung sollte mit der hier vorliegenden Arbeit angegangen werden.

## Herstellung der Nanoröhrchen

Seit ihrer Entdeckung wurden verschiedene Methoden entwickelt, um Kohlenstoffnanoröhrchen herzustellen. Die in dieser Arbeit verwendeten CNTs wurden nach einer Variante der CVD-Methode hergestellt, die heutzutage am weitesten verbreitet ist. Dazu wird Ferrocen als Katalysator in Xylol (für reine Kohlenstoffnanoröhrchen) oder Benzylamin (für Stickstoff-dotierte Röhrchen) gelöst, und die Flüssigkeit über einen Piezo-Ultraschallgeber zu einem Aerosol zerstäubt. Dieses wird in einen Ofen eingeleitet, der auf etwa 800 - 900°C geheizt ist. Dort zersetzen sich die organischen Moleküle und Nanoröhrchen wachsen an den Wänden des Quartz-Ofenrohres. Um eine bessere Haftung zwischen Matrix und Nanoröhrchen zu erreichen, wurden in nahezu allen hier vorgestellten Experimenten Stickstoff-dotierte MWNTs verwendet. Wo dies nicht der Fall ist, ist es ausdrücklich vermerkt.

## Herstellung der Proben mit Schichtaufbau

Um einen Modellverbund zu erhalten, in dem die Nanoröhrchen gut vereinzelt in ein reines Metall eingebettet sind, wurde folgender Ansatz verfolgt. Auf einem Silizium-Wafer wird eine Kupferschicht durch DC-Magnetron-Sputtering abgeschieden. Auf diese Schicht werden die Nanoröhrchen aus einer Suspension aufgesprüht, bevor eine zweite Metallschicht darauf abgeschieden wird, die die Nanoröhrchen einschließt. Die Gesamtdicke beider Schichten wurde dabei zwischen 500 nm und 1500 nm variiert.

Die größte Schwierigkeit bestand darin, ein Lösungsmittel und eine Methode zu finden, die sicherstellen, dass die Probe weder übermäßig verschmutzt, noch dass die Nanoröhrchen agglomerieren. Dabei sollte zusätzlich die Dichte an CNTs möglichst hoch sein. Nach vielen Versuchen wurde hochreines Ethanol als das beste Lösungsmittel ausgemacht, da es die saubersten Proben ergibt. Ethanol ist aber ein recht schlechtes Lösungsmittel für Nanoröhrchen, weswegen die CNT-Dichte der Suspension sehr niedrig gewählt werden musste. Um trotzdem eine vergleichsweise hohe Dichte an Nanoröhrchen in der Probe zu erreichen, wurde die Probe mehrfach mit der Suspension eingesprüht. Zwischen den Sprühungen wurde die Probe jeweils getrocknet, um den Nanoröhrchen möglichst wenig Bewegungsfreiheit zu geben. Sechzehn solcher Sprühzyklen stellten sich als der optimale Kompromiss zwischen der Sauberkeit der Probe und der CNT-Dichte heraus. Die Dichte, die dabei erreicht wurde, lag bei etwa 0,005 Nanoröhrchen/ $\mu\text{m}^2$ .

Da die Konformität beim Sputtern sehr hoch ist, d.h. das Höhenprofil der Probe größtenteils erhalten bleibt, können die Nanoröhrchen auch noch nach dem Abscheiden der zweiten Kupferschicht leicht lokalisiert werden. Dies wurde ausgenutzt, um mit dem Rasterionenmikroskop (focused ion beam, FIB) Querschnitte anzufertigen. Dabei stellte sich heraus, dass die CNTs vollkommen vom Kupfer umschlossen sind, solange sie gut vereinzelt sind und flach auf der unteren Kupferschicht aufliegen. Nur an Stellen, wo sich mehrere Nanoröhrchen überkreuzen, oder wo sie sich in einem Bogen über die Grenzfläche erheben, fanden sich Poren und Abschattungseffekte (Bild 3.12 auf S. 70).

Ebenfalls mit dem FIB wurde eine Querschnittsprobe für das Transmissionselektronenmikroskop (TEM) angefertigt (Bild 3.13 auf S. 72). Der Schnitt wurde so gewählt, dass das Nanoröhrchen genau senkrecht durch die TEM-Lamelle verlief. Auf diese Weise konnte nicht nur die Grenzfläche gut betrachtet werden, auch die konzentrischen Ringe der verschiedenen Wände des MWNTs wurden sichtbar. Die Grenzflächen zwischen Kupfer und CNT waren sehr sauber, und oberhalb des Nanoröhrchens konnten die Kupferebenen bis an das Nanoröhrchen heran verfolgt werden. Nur in den Ecken unterhalb fanden sich einige amorphe Bereiche, die wohl auf Überreste des Lösungsmittels zurückzuführen sind.



## Mikrodruckversuche an säulenförmigen Proben

Aus diesen Proben mit Schichtaufbau wurden - ebenfalls mit dem FIB - Säulen mit einem Durchmesser von ca. 600 nm geschnitten. An diesen wurde daraufhin ein Mikrodruckversuch durchgeführt, wozu ein Nanoindenter mit einer flachen Spitze verwendet wurde. Vor und nach dem Versuch wurden die Säulen im Rasterelektronenmikroskop (REM) charakterisiert. Einige der Säulen enthielten Kohlenstoffnanoröhrchen, in den anderen war nichts zu sehen, was das Vorhandensein eines Nanoröhrchens allerdings nicht in letzter Bestimmtheit ausschließt, da sehr kleine Röhrchen übersehen werden könnten.

Die wahren Spannungs-Dehnungskurven aus den Druckversuchen ähneln sich sehr stark, was die erreichten Spannungen angeht (die Dehnung war durch den Weg des Indenters größtenteils vorgegeben), unterscheiden sich jedoch recht stark in der Form der Kurve. Dabei konnte allerdings kein Einfluss der Nanoröhrchen festgestellt werden. Stattdessen zeigten sich zwei andere Korrelationen, die hier kurz beschrieben sein sollen.

Einige der Säulen wiesen eine besonders starke Verformung in der oberen Schicht auf, was zu einem pilzartigen Aussehen der verformten Probe führte. Diese Proben zeigen im Spannungs-Dehnungsverhalten Bereiche von großen Dehnungssprüngen bei geringer Spannungserhöhung oder sogar einem leichten Spannungsabfall, die sich mit Bereichen mit nahezu elastischem Verhalten abwechseln. Bei genauerer Betrachtung zeigen auch die meisten anderen Säulen eine stärkere Verformung in der oberen Kupferschicht. Ein Zusammenhang mit dem Böschungswinkel der Säulen, wie in der Literatur angenommen, konnte jedoch nicht festgestellt werden.

Zum zweiten wurde zwar bei manchen Proben das aus der Literatur bekannte Verformungsbild von stark ausgeprägten Scherbändern festgestellt, es gab jedoch auch Säulen, die sich durch Zwillingsbildung verformten, was bis jetzt in der Literatur nicht berichtet wird. Es wird vermutet, dass die Versetzungsstruktur an der Grenzfläche zwischen den Kupferschichten sowie an den Korngrenzen darüber entscheidet, ob sich eine Säule durch Scherung oder durch Zwillingsbildung verformt, doch liegen hierfür nicht genügend Daten vor. Auffallend ist jedoch die flache Form

der Spannungs-Dehnungskurven der Zwillingsäulen, die nur eine sehr schwach ausgeprägte Streckgrenze zeigen und in denen Plastizität sehr viel früher einsetzt als in den anderen Säulen. Dieses Ergebnis steht im Widerspruch zu Erfahrungen aus Versuchen an makroskopischen Proben, in denen Zwillingsbildung in aller Regel eine Härtesteigerung bewirkt. Weitere Versuche wären nötig, um diesen Widerspruch zu erhellen und auch um zu klären, warum es in Kupfermikrosäulen überhaupt zu Zwillingsbildung kommt, was in makroskopischen Proben bei diesen Verformungsbedingungen nicht erwartet wird.

Zeigen die Nanoröhrchen auch keinen Einfluss auf die Form der Spannungs-Dehnungskurven, so gibt es doch eine interessante Beobachtung in den mikroskopischen Aufnahmen: erschien die Austrittsstelle des Nanoröhrchens vor dem Druckversuch vollkommen plan und in einer Ebene mit der Flanke der Säule, war sie nach dem Versuch von einer trichterförmigen Vertiefung umgeben und etwas von der Probenoberfläche zurückgesetzt. Dies ist ein Anzeichen darauf, dass es eine gewisse Haftung zwischen Nanoröhrchen und Matrix gab. Da das Nanoröhrchen viel steifer ist als das Kupfer, kann es sich nicht in dem Maße verlängern, wie die Säule beim Druckversuch an Breite zunimmt. Dadurch wird auch das Kupfer, das am Nanoröhrchen anhaftet, zurückgehalten, was zu der beobachteten Vertiefung führt (Bilder 4.13 und 4.14 auf S. 96f).

Aus zwei der Säulen wurde nach dem Druckversuch mithilfe des FIB eine TEM-Probe geschnitten (S. 90ff). Wie zu erwarten war ist der Kontrast des Nanoröhrchens inmitten des Kupfers sehr schwach. Mit Hilfe von Aufnahmen der Proben aus REM und FIB konnte die Position der Nanoröhrchen aber mit ausreichender Sicherheit bestimmt werden, auch wenn der letzte Beweis (z.B. durch Nachweis von Kohlenstoff an diesen Stellen) nicht gelang.

Unter der Annahme, dass der beobachtete Kontrast tatsächlich durch Kohlenstoffnanoröhrchen verursacht wird, und dass kein Bereich übersehen wurde, bietet sich Bild 4.15 auf S. 98. Das Nanoröhrchen liegt genau oberhalb der Grenzfläche nahezu parallel zu Oberfläche der TEM-Lamelle. Während es auf der rechten Seite einen zusammenhängenden Kontrast (wenn auch bei verschiedenen Kippwinkeln) mit ca. 30 nm Höhe und 580 nm Länge gibt, sind auf der linken Seite nur zwei kleinere Abschnitte von jeweils ca. 10 nm Höhe und 50 nm bzw. 110 nm Länge zu

sehen. Der ursprüngliche Säulendurchmesser betrug dagegen nur 690 nm (und damit weniger als alle Bereiche zusammen, aber mehr als der größere allein). Dieses Bild lässt sich mit folgender Hypothese erklären: Während des Druckversuchs erfährt die Säule eine große Querdehnung (36%), die die Bruchdehnung, die bisher für Kohlenstoffnanoröhrchen beobachtet wurde (5%) weit übersteigt. Das Nanoröhrchen bricht deshalb, wobei es zu dem bei Nanoröhrchen oft beobachteten "Schwert-in-Scheide"-Effekt kommt, bei dem die inneren Wände aus der Hülle der äußeren herausgezogen werden. Dadurch erklärt sich auch die unterschiedliche Höhe, da in diesem Fall in den beiden kleineren Bereichen weniger Kohlenstoffwände vorliegen würden.

## Teppiche und Adhäsion

Neben der Schichtherstellung durch Magnetron-Sputtern wurde auch ein elektrolytisches Verfahren verwendet. Der Elektrolyt bestand aus einer Lösung von  $\text{Cu}_2\text{SO}_4$  und  $\text{KNaC}_4\text{H}_4\text{O}_6$  in Wasser, mit einem Pyrophosphatpuffer, um den pH-Wert im Bereich zwischen 8,2 und 8,5 zu halten.

Als Substrat wurden größtenteils Stücke eines Silizium-Wafers verwendet, auf denen eine dünne Kupferschicht durch Magnetron-Sputtern abgeschieden worden war. Die Nanoröhrchen wurden auf zwei verschiedene Weisen auf diesem Substrat aufgebracht. Zum einen wurden sie einfach im Elektrolyten selbst suspendiert, woraus sie dann langsam absedimentierten. Die resultierende Nanoröhrchendichte war hierbei sehr gering. Zum anderen wurde das CNT-Pulver mit einem Spatel direkt auf das Substrat aufgedrückt, wodurch eine sehr hohe Dichte entstand.

Die restlichen Proben bestanden aus Waferstücken, auf denen Kohlenstoffnanoröhrchen solchermaßen aufgewachsen waren, dass sie einen Teppich bilden. Ein Teil dieser Proben bestand aus gut ausgerichteten "Büscheln" von Nanoröhrchen unterschiedlicher Länge (siehe Bild 5.1 auf S. 107). Der andere Teil zeigte einen sehr dichten Teppich aus verfilzten Nanoröhrchen. Beide Proben waren nicht mit Stickstoff dotiert.

Die Elektrolysedauer wurde zwischen wenigen Sekunden und knapp 4 Minuten variiert, um die Anfangsstadien der Abscheidung zu beobachten. Dabei zeigte sich,

dass sich das Kupfer bevorzugt auf den Nanoröhrchen abscheiden, obwohl zumindest im Fall der kupferbeschichteten Substrate auch das Substrat leitfähig ist (Bild 5.2 auf S. 109). Die bevorzugte Abscheidung auf den Nanoröhrchen hat wohl geometrische Gründe. Durch die Krümmung der Röhrchen ist das elektrische Feld hier stärker, was zu einer erhöhten Abscheiderate führt. Dies ist besonders deutlich bei den Proben mit den senkrecht stehenden CNT-Büscheln zu beobachten. Hier ist die Abscheiderate an den Spitzen deutlich höher als am Übergang zum Substrat und auf dem Substrat selbst findet keine Abscheidung statt. An den Spitzen existiert aber eine deutliche Feldüberhöhung. Bei den Proben mit den verfilzten Nanoröhrchen zeigte sich prinzipiell ein ähnliches Bild, jedoch variierten hier die Abscheideraten sehr stark von Probenort zu Probenort.

Die Elektrolyse an den Proben mit CNT-Büscheln wurde nicht fortgeführt, bis ein dichter Film entstand, sondern nur bis zu dem Punkt, an dem die Büschel selbst vollständig beschichtet waren (Bild 5.3 auf S. 110). Querschnitte (FIB) zeigen, dass das Kupfer die Nanoröhrchen eng umschließt, und es nur sehr wenig Porosität gibt. Allerdings zeigen sich in diesen Proben auch bereits Bereiche, die aus reinem Kupfer ohne CNTs bestehen. Mit einem Nanoindenter wurde ein Bereich einer dieser Proben verformt, und die Probe danach erneut im REM untersucht. Dabei zeigten sich an vielen Stellen Anzeichen von Adhäsion (Bild 5.4 auf S. 112 und Bild 5.5 auf S. 113). Insbesondere wurden mehrfach Nanoröhrchen gefunden, die zwar aus der Matrix herausgezogen worden waren, aber noch immer von einer dünnen Schicht Kupfer vollständig umhüllt waren. Das lässt darauf schließen, dass zumindest in einigen Fällen die Grenzflächenhaftung größer ist als die Scherfestigkeit des Kupfers. Auch bei den verfilzten Nanoröhrchen wurden Stellen gefunden, an denen die Kraftübertragung durch die Grenzfläche groß genug war, um Bruch in den Nanoröhrchen zu verursachen.

## Elektrolytische Zugproben

Mit der gleichen Elektrolytzusammensetzung wurden auch Proben für einen makroskopischen Zugversuch hergestellt. Als Substrat wurde hierbei eine Zinnfolie verwendet. Um stets eine große Anzahl an Nanoröhrchen in der Nähe der Probenober-

fläche zu haben, wurden die Proben in fusselfreies Papier eingewickelt, das dann mit einer Lösung von sehr hoher CNT-Dichte getränkt wurde. Die Elektrolyse selbst wurde dann mehrfach unterbrochen, um ein neues Papier anzubringen. Dadurch wird verhindert, dass das Papier in die Probe einwächst. Auf die Weise wurden Kupferschichten mit einer Dicke von ca. 20  $\mu\text{m}$  hergestellt.

Nach der Elektrolyse wurden die Proben auf die Knochenform für den Zugversuch zugeschnitten (Länge 5 cm, Breite des mittleren Bereichs 5 mm) und das Substrat durch Ätzen in HCl entfernt. Mit Hilfe eines Halters wurden die Proben dann in der Zugprüfmaschine eingespannt, der Halter geöffnet und die Probe bis zum Bruch gedehnt. Danach wurden die Bruchfläche im REM mikroskopisch untersucht.

Alle Proben mit einer Ausnahme zeigen ein sprödes Bruchverhalten. Die Ausnahme ist die einzige Probe, die nicht geätzt wurde, da sich die Kupferschicht aufgrund schlechter Haftung von selbst vom Substrat gelöst hatte. Wahrscheinlich versprödet das Kupfer aufgrund der starken Wasserstoffbildung beim Ätzen. Die erreichte CNT-Dichte variiert zwischen den verschiedenen Proben. Vergleicht man die Proben mit dem höchsten Gehalt mit Kontrollproben, die nach dem gleichen Verfahren hergestellt sind, aber keine Nanoröhrchen enthalten, so findet man keine signifikante Änderung des E-Moduls. Die Gesamtenergie bis zum Bruch aber (d.h. die Fläche unter der Spannungs-Dehnungskurve) nimmt um über 100% zu, und übersteigt damit selbst den Wert der nicht geätzten Probe noch um bis zu 31% (Bild 6.19 auf S. 139).

Auch die mikroskopischen Aufnahmen der Bruchfläche zeigen ein ähnliches Bild. Bei den CNT-Proben finden sich immer wieder Stellen, wo sich ein Seitenriss im rechten Winkel zur eigentlichen Bruchfläche gebildet hat. Oft sind diese Risse zu höhlenartigen Öffnungen erweitert. In diesen Höhlungen finden sich tropfsteinartige Auswüchse (Bild 6.12 auf S. 133). Viele dieser Auswüchse enthalten ein Nanoröhrchen, doch gibt es auch welche, bei denen das nicht der Fall ist. Je mehr Nanoröhrchen eine Probe enthält, desto häufiger sind die Höhlen und vor allem die Auswüchse. Auch an anderen Stellen finden sich Anzeichen für eine signifikante Grenzflächenhaftung, wie z.B. Nanoröhrchen, die einen schmalen Riss überbrücken, oder die von einem zipfelförmigen Kupfersaum umgeben sind (Bild 6.17 auf S. 137). Daneben fanden sich aber auch immer wieder Nanoröhrchen, die nur eine schlechte Haftung

zum Kupfer aufwiesen.

## Zusammenfassung und Ausblick

Entgegen den bisherigen Annahmen in der Literatur wurden in allen Versuchen deutliche Anzeichen für signifikante Grenzflächenhaftung zwischen Kohlenstoffnanoröhrchen und der Kupfermatrix festgestellt, sowohl bei den gesputterten Proben, als auch bei den durch Elektrolyse hergestellten. Dies ist ein sehr ermutigendes Ergebnis für den Einsatz von Kohlenstoffnanoröhrchen in Metallmatrix-Verbunden.

Es gibt aber noch immer viele offene Fragen, was die Wechselwirkungen zwischen Metall und Nanoröhrchen angeht. Wie lässt sich die Grenzflächenhaftung beeinflussen? Was passiert während der Verformung? Können Nanoröhrchen als Versetzungshindernisse fungieren? Die in dieser Arbeit entwickelten Modellverbundwerkstoffe eignen sich für eine Vielzahl von weiteren Versuchen:

- Querschnittspräparate mit definierter Orientierung der Nanoröhrchen in der Matrix erlauben es, die Grenzflächenchemie mit Hilfe analytischer TEM zu untersuchen.
- Eine Weiterführung der Druckversuche an den Säulchen könnte weitere Hinweise auf die Wechselwirkung zwischen Nanoröhrchen und Matrix geben. Insbesondere wären hier Versuche mit geringerer Verformung, sowie *in situ* Druckversuche im TEM von Interesse.
- Bei den elektrolytischen Zugproben ist der nächste logische Schritt, durch einen Wechsel des Substrats den Ätzschritt zu vermeiden und somit das Material weniger zu schädigen. Erst dann können verlässliche Daten über das Schädigungsverhalten dieser Proben gewonnen werden. Auch eine weitere Steigerung des CNT-Gehalts wäre von Vorteil.
- Eine Möglichkeit, einen hohen CNT-Gehalt zu erreichen, wäre die Fortführung der Versuche an den Proben mit teppichartig orientierten Nanoröhrchen. Die bis jetzt verwendeten Teppiche sind nicht ausreichend, um eine kompakte

Probe mit homogener CNT-Dichte zu erreichen. Ein zu hoher CNT-Gehalt würde aber wahrscheinlich zu Abschattungsproblemen und Porenbildung führen.

Kohlenstoffnanoröhrchen haben viele Eigenschaften, die sie als nahezu ideale Verstärkungsfasern für Metallmatrix-Verbundwerkstoffe erscheinen lassen. Bis jetzt wurde - neben der Herstellung einer homogenen Probe - die Frage der Grenzflächenhaftung als das größte Problem empfunden. Die Ergebnisse dieser Arbeit zeigen nun, dass auch dieses Problem lösbar ist, und dass Kohlenstoffnanoröhrchen durchaus halten können, was sie versprechen. Noch immer aber gibt es viele offene Fragen, zu deren Klärung die hier vorgestellten Modellverbundwerkstoffe beitragen können.





# Abstract

Two model composites of copper and carbon nanotubes were fabricated by very different depositions methods. Copper electrodeposition in a plating bath containing nanotubes created a 3D matrix of randomly oriented CNTs within a thick, 20 micron Cu film. In contrast, sandwiching a layer of well-separated nanotubes between two sub-micron, magnetron sputtered Cu layers produced a 2D composite with nanotubes lying parallel to the substrate surface.

These composites, which were mechanically tested using various techniques, proved to be well suited to explore the nature of the CNT/Cu matrix interface. Columns approximately 600 nm in diameter and 1.4 microns high were cut from the sputtered deposited composites and microcompression tested in a nanoindenter. No influence of the presence of nanotubes on the stress-strain-curves was observed, which was attributed to the low nanotube content. On the other hand, microscopic analysis showed an influence of the nanotube on the immediately surround it, resulting in funnel-like depressions on the column surface. In addition to deformation by slip, twinning was observed in some columns, which has never before been reported in the literature for micron-sized columns. Macroscopic tensile tests were performed on the electrodeposited films and the samples with the highest carbon content showed an increase in toughness of over 100% with respect to the CNT-free control samples produced by the same method. Finally, short copper electrodepositions into carbon nanotube carpets revealed large regions with conformally coated nanotubes.

Until now, it was assumed that Cu would not wet the nanotube and that the interfacial strength between the Cu and CNTs would be low, since Cu does not form a carbide. However, these experiments all revealed clear evidence of adhesion

exceeding the copper shear strength. To our knowledge, this is the first time such strong adhesion was demonstrated between a nanotube and a metal matrix. We attribute this unexpected, but highly desirable adhesion and wetting behavior to the defect structure in the nanotubes used. As a good adhesion between fiber and matrix is a prerequisite for the successful use of carbon nanotubes in metal matrix composites, these results are very encouraging. The composites and methods presented here provide a foundation for further studies needed to understand the nanotube-metal interaction in more detail and thus ultimately for successful metal-carbon nanotube composites.

# Chapter 1

## Introduction

For millennia, only two modifications of carbon have been known to mankind: graphite and diamond. Both have played an important role in technology, due to their properties, which are quite unique in the world of materials. Diamond is nature's hardest material and has been used as tip for drills, as abrasive, and of course as gemstone. Graphite was used for its electric conductance (e.g. as electrodes), for its very small interplanar shear strength (as lubricant or in pencils) and for its high intraplanar tensile strength (in carbon fibers).

Then in 1986 the fullerenes and in 1991 the carbon nanotubes were discovered as new modifications of carbon and especially the nanotubes have shown properties that could make them as technologically interesting as graphite and diamond. Due to their atomic structure, nanotubes are very strong in the direction of their axis, while remaining extremely flexible. In addition, they have interesting electronic properties - e.g. they can be either conducting or semiconducting. Finally, their small diameters make them a truly nano-sized material with a range of interesting possibilities, yet also with all the ensuing difficulties, especially concerning the handling of such tiny structures.

Early on, carbon nanotubes were being discussed as reinforcement material for composites. At first, most of the effort was concentrated on polymer matrices, later on, ceramic matrices gained influence, but it was not until quite recently that work on metal matrix composites with carbon nanotubes was being published. Such

carbon nanotube reinforced metals will be the topic of this work. Apart from the - as yet still not completely solved - problem, of how to disperse a large volume fraction of nanotubes homogeneously within the matrix, some remarkable results have been reported. Even small quantities of carbon nanotubes can significantly enhance the mechanical properties of metals. However, all the work published has been mainly phenomenological, without offering any explanations as to what mechanisms lie behind this reinforcing effect.

To gain a better understanding of these materials, it is therefore necessary to study the mechanisms of how nanotubes and metals interact. What is the chemical composition of the interface, how do dislocations interact with nanotubes, how strong are the adhesive forces at the interface... To answer such questions, model composites are needed which allow the study of small scale phenomena. The requirements for such composites are different from those of materials intended for actual use. A model composite does not need the high nanotube concentration necessary for an effect on the macroscopic properties of a composite. Instead, it is much more important that the nanotubes can be easily localized and that the materials are of high purity to exclude as many side effects as possible.

In this work, the preparation of two different model composites is reported. In addition, some experiments using these materials are presented together with preliminary results on the interaction of carbon nanotubes with a copper matrix.

# Chapter 2

## Literature Review

### 2.1 Carbon nanotubes

Ever since their discovery in 1991 [1] carbon nanotubes (CNTs) have been the subject of enormous scientific interest. Their strength, their flexibility, their electronic properties, but above all their small size make them interesting materials for a large range of applications. However, industrial integration of CNTs is limited by difficulties in handling and processing and many issues remain unresolved to this day. The following section will give a short overview of the state of the art in the fields relevant to this work.

#### 2.1.1 Structure

##### Single-walled carbon nanotubes

A single-walled carbon nanotube (SWNTs) can be visualized as a rolled-up graphene sheet. To avoid dangling bonds, the ends form closed caps. These caps are formed by replacing six of the graphene hexagons with pentagons, thus inducing the necessary curvature. Such tubes are ideally perfectly straight, but bends can be formed by pentagon-heptagon pairs along the tube length. Depending on the orientation of the graphene sheet in relation to the tube axis, SWNTs can be classified as zigzag,

armchair or chiral tubes (see fig. 2.1). This chirality is of great importance for the electronic properties of SWNTs (armchair tubes are metallic conductors whereas zigzag and chiral tubes can be either conducting or semiconducting) and to a lesser extent for the mechanical properties, which will be discussed in more detail in section 2.1.3. [2].

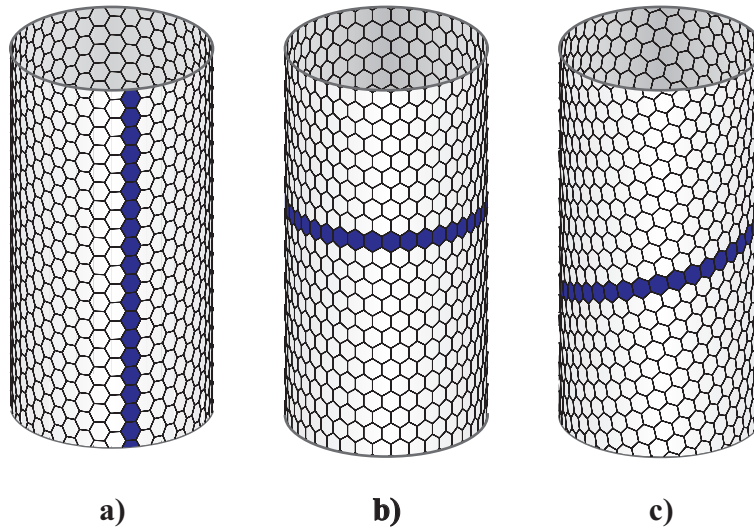


**Figure 2.1:** Different types of single-walled carbon nanotubes: a) armchair b) zigzag c) chiral.

The smallest commonly found SWNTs found regularly have a diameter of about 0.6 nm. This corresponds to 10 hexagons around the circumference, which is exactly the size of a  $C_{60}$ -fullerene. Smaller tubes are very rare as the strong curvature makes them unstable. The upper range for the diameter is around 4 nm. The tube length varies greatly. In principle, the tube length should be easily controllable through the synthesis time, but this is often not the case. Recently, Hata et al. achieved the synthesis of SWNTs of 2.5 mm in length [3].

Due to the large molecular weight of SWNTs and their high flexibility, they tend to form bundles based on Van-der-Waals-forces. Even in dispersion, they can usually not be separated completely. Instead several nanotubes will form a highly aligned bundle, which is much shorter than the average nanotube length. As each nanotube takes part in several such bundles, a net-like structure is formed.

## Multi-walled carbon nanotubes

Multi-walled nanotubes (MWNTs) consist of several SWNTs stacked in the manner of a Russian doll. The number of walls varies between 2 and several dozen and is not directly related to the tube diameter, although larger tubes tend to have more walls. The spacing between adjacent walls is usually around 0.344 nm and thus quite close to the layer spacing in graphite, which is 0.334 nm [4]. Determining the chirality of MWNT-shells experimentally is not easy, but so far it seems that in most cases the chiralities of adjacent layers are independent of each other. This results in the fact that the physical properties of MWNTs are hardly influenced by chirality effects. For example, all MWNTs are metallic conductors [5].

The diameter of MWNTs varies greatly, but most are between 10 nm and 100 nm, although larger tubes can be found. The longest MWNTs produced up till now had a length of 2.2 mm [6], thus coming very close to the record for SWNTs. Sometimes, the inner tubes are shorter than the outer ones, thus forming several compartments.

MWNTs are stiffer than SWNTs. They can therefore be separated in dispersion. If the concentration is too high, they form tangles with little, if any, parallel alignment between neighboring tubes

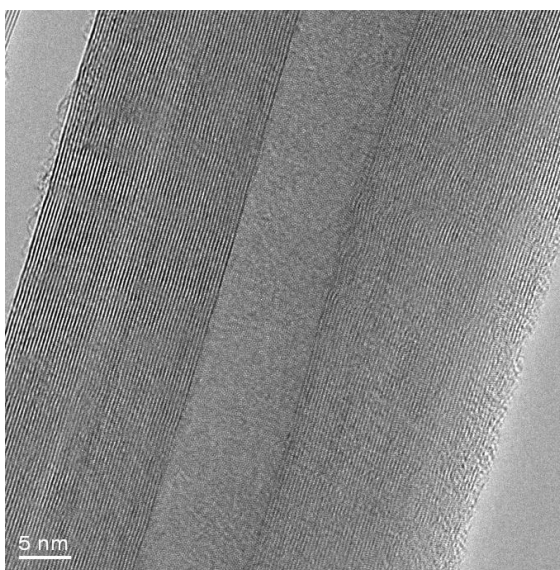


**Figure 2.2:** TEM image of a multi-walled carbon nanotube. Courtesy of Dr. Nicole Grobert, unpublished.

## 2.1.2 Production methods

### Arc discharge

Over the years, several methods have been developed to produce carbon nanotubes, both single- and multi-walled. Iijima [1] found the first CNTs in the cathode deposit after an electric arc-discharge experiment to synthesize fullerenes. If a pure carbon anode is used, multi-walled nanotubes will form. Single-walled tubes can also be synthesized by doping the electrodes with transition metals such as iron, cobalt, or nickel.

Arc-discharge-grown multi-walled nanotubes are usually straight and have few defects, which gives them excellent mechanical and electrical properties. However, they are rather short and the samples require a purification step since the CNTs are mixed with other forms of carbon. The samples are purified through an oxidizing treatment. This can be achieved by heating the sample to about 700°C in air or by using strong oxidizing agents such as nitric acid [7]. Carbon nanotubes are more resistant to oxidation than amorphous carbon or other small carbon particles, but still more than 90% of the sample is usually lost to achieve a sample virtually free of other carbonaceous species [8].

### CVD

In 1993, a method was developed to produce carbon nanotubes via a chemical vapor deposition (CVD) process [9] [10] [11]. When hydrocarbons such as benzene or methane are decomposed inside a furnace in the presence of metallic catalysts (iron, nickel, cobalt), carbon nanotubes are formed. At temperatures around 900°C, multi-walled nanotubes will be formed. Temperatures above 1000°C will result in SWNTs [8]. It is not clear what causes this switch in mechanism.

Using the right conditions, large arrays of aligned tubes can be grown [12] (see fig. 2.3). Usually, the catalyst is deposited on the substrate in the shape of a thin film or nanoparticles [9]. A different approach is used in the aerosol technique, in which the catalyst is included in the carbon source in the form of a metalorganic



compound (for example ferrocene dissolved in xylene). This precursor solution is dispersed to an aerosol by ultrasound. An inert gas stream conveys the aerosol to the hot zone of a furnace, where the organic compounds decompose. The metal atoms form small clusters, which then act as catalyst particles for the formation of CNTs [11].

The CVD-process is easy to implement, and offers the possibility to produce large nanotube samples (up to several hundred milligrams) in a single run of the experiment, yet there is still no continuous process. Purification is often not needed. As a result, CVD-grown nanotubes are cheaper than arc-discharge nanotubes. On the other hand, they have more defects, and are less rigid, which is reflected in their wavy appearance in TEM images.

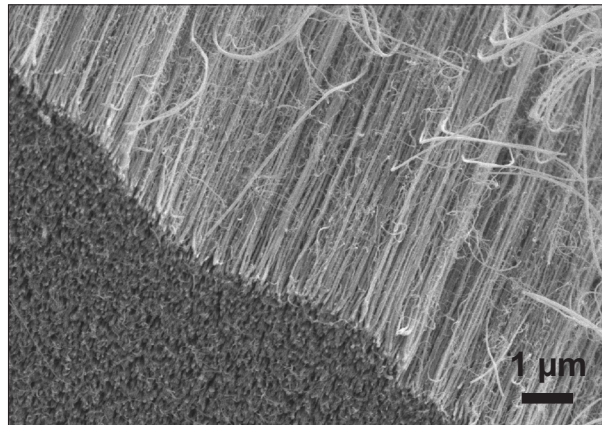


**Figure 2.3:** Nitrogen-doped nanotubes produced for this study with aerosol-based CVD. The nanotubes are clean, well aligned and form a dense carpet. The average tube length of this sample was 87  $\mu\text{m}$ , the average diameter 52 nm and the yield 265 mg.

The first step to a continuous process was accomplished by Li et al. in 2004. They spun a thread consisting of single- or multi-walled tubes directly from the reaction zone of the CVD furnace. The purity of these threads was high, with little amorphous carbon left, but the orientation was rather poor which lead to low values for the elastic modulus [13].

### Growth models

How the presence of transition metal clusters catalyzes the formation of carbon nanotubes is not yet completely clear. Two different models have been proposed,

both were originally developed for the growth of carbon fibers. (see fig. 2.4)

In the so-called tip growth model, free carbon diffuses into the catalytic particle from the gas phase. As soon as the catalyst is saturated, a CNT forms at the opposite side of the catalyst. As the tube gets longer the catalyst particle is pushed upwards. Growth is terminated when all free carbon has been used, or when the particle becomes completely covered with a hood of graphitic carbon. [14]

In the base growth model, the carbon diffuses into the catalyst particle via surface diffusion along the substrate. Again the tube forms once the particle is supersaturated. As the carbon flow is in this case reversed when compared to the tip growth model, the resulting tube grows out of the top of the particle, leaving the catalyst attached to the substrate [15].

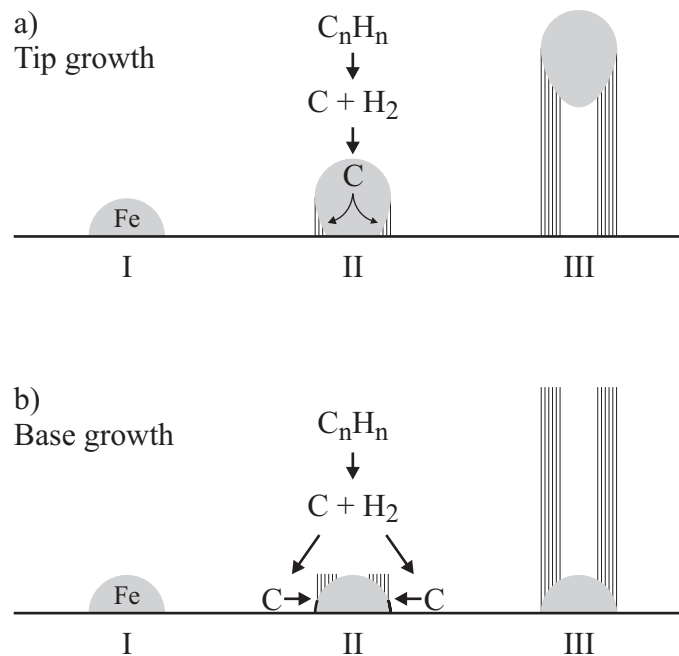


**Figure 2.4:** Schematic representation of the two growth models.

a) tip growth: I - the catalyst particle on the substrate, II - hydrocarbons decompose on the Fe surface and the carbon diffuses from the top of the particle to the bottom. As the particle supersaturates, graphitic tube walls are formed. III - the growing nanotube pushes the catalytic particle upwards [14].

b) base growth: I - the catalyst particle on the substrate, II - Carbon adsorbs to the substrate and is transported to the catalyst particle through surface diffusion. As the particle supersaturates, graphitic walls start to form at the top of the particle. III - the nanotubes grow from the top of the particle, which remains attached to the substrate. [15].

Recently, Helveg et al. [16] have shown the first *in situ* TEM images of catalytically growing carbon nanotubes. Their results support the tip growth model, but it is not yet clear, whether this model is valid under all condition as no catalyst particles were found at the top of the tubes in other experiments (see e.g. Xia et al [17]).

### 2.1.3 Mechanical properties

The carbon-carbon bond ( $sp^2$ ) within a graphene plane is considered to be the strongest interatomic bond in nature [18]. Therefore, carbon nanotubes, with their perfect alignment of the graphene planes, should possess exceptional mechanical properties parallel to the tube axis. And they do indeed. In addition to a high elastic modulus, tensile stress and breaking strain, it has been recently found that at very high temperatures (more than 2000°C) single-walled nanotubes also exhibit superplasticity. Under these conditions Huang et al. have reported a breaking strain of 280 % and reduction in diameter from 12 to 0.8 nm [19].

The small size of nanotubes, however, makes it impossible to use conventional testing equipment for mechanical measurements. Over the last fifteen years, many groups have therefore found new methods for experiments at such small dimensions. Most of them were mainly interested in the Young's modulus, but many other properties were investigated as well.

Treacy et al. [20] were the first to measure the Young's modulus of multi-walled carbon nanotubes (arc-discharge) experimentally. They used TEM images of free standing tubes attached at only one end to measure the amplitudes of their intrinsic thermal vibrations. They investigated tubes with outer diameters ranging from 5.6 nm to 24.8 nm and found an average value of  $E = 1.8$  TPa. The individual values, however, ranged from 0.40 TPa to 4.15 TPa.

Other authors studied the mechanical properties of carbon nanotubes using various techniques including the excitation of resonant frequencies in an electrostatic field, AFM, and nanoindentation or even direct tensile tests *in situ* in an electron microscope. The Young's modulus of CNTs was also the subject of several theoretical

calculations, using molecular dynamics or a force-constant model. For computational reasons, the simulations are so far limited to short tube lengths and few walls (up to four). Experimentally and theoretically determined values for  $E$  are summarized in table 2.1. All experimental values were derived from MWNTs grown in an arc-discharge, except for Cao et al. who used CVD-grown tubes. As a comparison, the in-plane modulus of graphite is given.

**Table 2.1:** Literature values for Young’s modulus of CNTs

$E$	method	author
1800 GPa	thermal vibrations (TEM)	Treacy et al. [20]
1260 GPa	beam deflection (AFM)	Wong et al. [21]
910 GPa	<i>in situ</i> tension (TEM)	Demczyk et al. [22]
810 GPa	clamped-beam (AFM)	Salvetat et al. [23]
18-68 GPa	<i>in situ</i> tension (AFM-SEM)	Yu et al. [24]
840 GPa	axial compression	Cao et al. [25]*
1110 GPa	force-constant (theor.)	Lu. [26]
870 GPa	molecular dynamics (theor.)	Liew et al. [27]
1026 GPa	graphite (in-plane)	Kelley [28]

\* value calculated from data given in the publication.

As can be seen from the table, the values - even within a single study - vary to a large extent. Some of the variation may be due to the fact that in some cases the load transfer from the outer shells to the inner ones is not perfect and that the effective cross-section therefore is actually much smaller. Yu et al. [24] found a Young’s modulus of 18-68 GPa when considering the whole cross-section, but 270-950 GPa when using only the outermost shell. Another factor seems to be the degree of crystallinity, which can vary to a large extent. Salvetat et al. measured the Young’s modulus of highly crystalline arc-grown MWNTs and of highly disordered CVD-grown MWNTs under the same conditions. They found an average value of 870 MPa for the arc-discharge tubes, but only 27 MPa for the CVD-tubes.

Due to differing experimental conditions (production method, measurement technique, temperature, tube length and diameter), the results of experimental studies

are hard to compare. Theoretical calculations, on the other hand, suffer from severe limitations due to the limited computational powers available today. As nanotubes consist literally of thousands of atoms, modeling is restricted to short tubes with few walls. So far, simulations have not treated tubes with more than four walls or an aspect ratio of more than nine. Multi-walled nanotubes, however, often have 50 walls or more and aspect ratios of well above one hundred. Therefore, theoretical and experimental results are hard to compare as well.

Many other elastic properties were measured or calculated as well. But in contrast to the Young's modulus, these are often given only in one or at the most a few papers, so that an in-depth comparison of different authors is not possible. Table 2.2 gives an overview of the literature.

As for the Young's modulus, there seems to be a great variability in the values determined for other mechanical properties. Using molecular mechanics calculations, Zhang et al. found a large influence of defects in the nanotube structure. Even small defects, such as one- or two-atom vacancies may reduce the tensile strength by as much as 20% - 33%. Torsional stresses, however, showed no influence on the tensile strength [33].

Although the absolute values for the different material properties are still unclear, valuable insight into the deformation and fracture behavior has been gained. Multi-walled carbon nanotubes are very flexible and bend at low stresses. They can accommodate large bending strains by local buckling (see fig. 2.5), a process which seems to be completely reversible [22] [21] [32]. Accordingly, carbon nanotubes are very hard to break in bending.

Recently, Cao et al. [25] have performed cyclic compression tests with films of aligned multi-walled CNTs (produced by CVD). When compressed, the nanotubes showed collective buckling (see fig. 2.6), which was to a large part reversible, even after 10,000 cycles. The recovering speed was very high, exceeding 2 mm/s (the upper limit of the measuring instrument). The critical compressive stress for buckling was found to be 92 MPa at 22% strain. The average buckling wavelength was 12  $\mu\text{m}$ , the nanotube diameter was 20 nm. Following Euler beam theory that would correspond to a Young's modulus of 840 GPa.

**Table 2.2:** Mechanical properties of carbon nanotubes - literature values

<b>property</b>	<b>value</b>	<b>source</b>
proportional strain limit (theor.)	6.3%	[27]
yield stress (theor.)	12.8 GPa	[27]
yield strain (theor.)	12%	[29]
	24.1 %	[27]
tensile strength (exp.)	150 GPa	[22]
	11-63 GPa	[24]‡
tensile strength (theor.)	40 - 50 GPa	[29]
	13.3 GPa	[27]
breaking strain (exp.)	5%	[22]
breaking strain (theor.)	28%	[27]
long. buckling stress (exp.)	92 MPa	[25]
long. buckling strain (exp.)	22 %	[25]
bending modulus (exp.)	1200 GPa	[30]†
	200 GPa	[30]‡
bending strength (exp.)	14.2 GPa	[21]
torsion shear modulus (theor.)	541 GPa	[26]
transv. compressive modulus (exp.)	9.7 GPa to 80 GPa	[31]*
transv. compressive strength (exp.)	99.9 GPa to 151 GPa	[32]

‡ value calculated only for outermost shell

† for nanotubes smaller than 8 nm in diameter

‡ for nanotubes larger than 30 nm in diameter

\* compressive modulus dependant on compressive strain

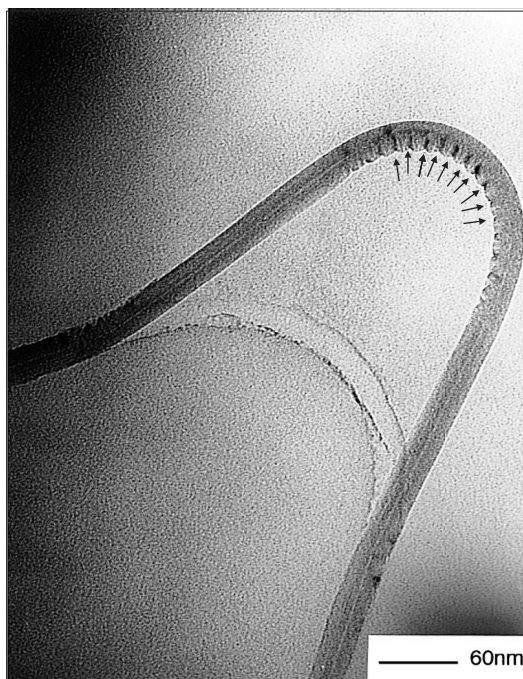


**Figure 2.5:** MWNT showing extensive buckling to accommodate large bending strains [32].

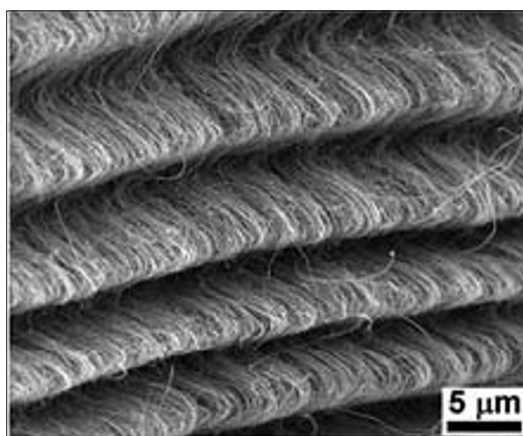


**Figure 2.6:** collective buckling in aligned MWNT-film after cyclic compression [25].



In tension, carbon nanotubes can be readily broken. Several authors [24] [22] report fracture by a "sword-in-sheath" mechanism, in which inner tubes are pulled out after the fracture of the outer tubes. This mechanism is also sometimes referred to as the "telescope effect". Due to this effect, it is often not possible to measure the remaining plastic strain of a tube after fracture. This mechanism can be explained by the low inter-planar shear strength of graphite of only 0.48 MPa [34]. Bichoutskaia et al. however find in their density functional theory calculations that although the shear stress between two non-chiral nanotubes is very low, it is much higher between tubes of two different chiralities [35]

#### 2.1.4 Wetting

Ebbesen et al. were the first to study the wetting behavior of carbon nanotubes [36] [37]. Several materials were tested for their ability to wet arc-grown MWNTs. These materials include a range of metallic melts, but unfortunately none of the metals used regularly for metal-matrix composites. They found that all materials with a surface tension of  $\gamma < 100 - 200 \text{ mJ/m}^2$  (Cs, Rb) wet carbon nanotubes, and fill the cavity of opened CNTs. All materials with surface tensions above that value (Pb, Hg, Ga, Te) do not. Cu has a surface tension of  $1430 \text{ mJ/m}^2$  [38] and should therefore not wet CNTs. A little later it was found that although liquid silver will not fill nanotubes of a diameter smaller than 4 nm, it does fill larger tubes [39]. Quite recently, Chen et al. found that mercury, which does normally not wet CNTs, will do so, if an electric potential is applied across the Hg/NT-interface [40].

There are also some studies which study the coating ability of several metals in respect to carbon nanotubes using deposition methods which do not rely on a metal melt. Zhang et al. used electron-beam evaporation of several metals and investigated if a continuous film was formed on single-walled nanotubes [41]. For Ti, Ni and Pd a continuous film was observed. Au, Al and Fe, on the other hand, formed small discontinuous clusters and showed no affinity to the nanotubes. A little later, Zhong et al. mixed nanosized powders of Fe, Ni and Co with both single- and multiwalled carbon nanotubes and then heated the samples at  $1000^\circ\text{C}$  for several hours to see, if coatings formed on the NTs [42]. No interaction was observed for



the SWNTs. MWNTs were wetted by Fe and Co, and to a lesser extent by Ni (note that the relative wetting of Ni and Fe is the opposite of that observed by Zhang et al.) The wetting seems to be correlated to the formation of carbides, which was strong in Fe, but weaker in Co and Ni. The poor wetting behavior of Au, finally, was also observed in density functional theory calculations done by Maiti and Ricca [43]. They concluded that there is no chemical bonding and that the SWNT studied is only physisorbed on the gold surface.

As long as no further data specific to carbon nanotubes is available, a behavior similar to conventional carbon fibers must be assumed. As a rule, metals wet carbon, be it diamond or graphite, if some kind of chemical reaction takes place [44]. The transition elements react strongly with carbon and thus the wetting behavior is good. Among these elements, the work of adhesion decreases from left to right ( $Ti > V > \dots > Ni$ ). Metals from Cu to Se do not wet carbon, as well as the elements below them - which is in agreement with the work of Ebbesen cited above. Boron and silicon wet carbon. This is also true for the alkaline metals. The earth alkaline metals should wet, since they can form stable carbides, but no experimental data is available. With aluminum the case is somewhat more difficult. Aluminum forms a carbide, yet wetting only takes place at temperatures above 900°C. This is probably due to the presence of an aluminum oxide layer inhibiting the chemical reaction. A graphic representation of the wetting behavior of the different elements is given in fig. 2.7

### 2.1.5 Nitrogen doping

The CVD-method is not only cheap and relatively easy to use, it also offers the possibility to dope carbon tubes with other elements. Most work so far has been done with nitrogen-doped tubes (usually abbreviated as  $CN_x$ ) [45], but boron-doping has also been achieved [46]. Doped nanotubes differ from undoped ones both in their molecular as well as in their electronic structures and thus offer a possibility to influence many properties.

The nitrogen content realized through the CVD of various nitrogen-containing precursors varies from approximately 2% [47] up to 32% [48]. Apart from different

H																	He
Li	Be											B	C	N	O	F	Ne
Na	Mg											Al*	Si	P	S	Cl	Ar
K	Ca	Sc	Ti	V	Cr	Mn	Fe	Co	Ni	Cu	Zn	Ga	Ge	As	Se	Br	Kr
Rb	Sr	Y	Zr	Nb	Mo	Tc	Ru	Rh	Pd	Ag	Cd	In	Sn	Sb	Te	I	Xe
Cs	Ba	La	Hf	Ta	W	Re	Os	Ir	Pt	Au	Hg	Tl	Pb	Bi	Po	At	Rn

Li	metals and metalloids	H	nonmetals
	forms carbides and wets carbon		does not wet carbon
	forms carbides		no information available

**Figure 2.7:** Elements and their wetting behavior concerning carbon. Aluminum does wet carbon, but only at temperatures above 900°C.

precursors, the temperature and general synthesis conditions also seem to play a role. He et al. were able to increase the nitrogen content in their nanotubes from 1.9% to 12% (EELS measurements) by adding H<sub>2</sub> to the reaction system [49]. In correlation with the present work, the results of Reyes-Reyes et al. should be mentioned here. By using a mixture of ferrocene and benzylamine (the same precursors as were used for the present work) they achieved a nitrogen content of 2% - 5% [50].

Regardless of the nitrogen-content, all CN<sub>x</sub> tubes are very similar in their structure, which is usually described as "bamboo-like". The inner core of such tubes is subdivided at regular intervals by one or more graphene sheets. Also, the tube walls are less perfect and often show a wavy appearance. Results so far suggest that the higher the nitrogen-content, the more disturbed the graphene sheets.

The nitrogen atoms can occupy several sites in the carbon-lattice (see fig. 2.9). Single nitrogen atoms can take the place of any carbon atom in which case there will be one free electron [51]. If three such substitutional atoms come together they can form a pyridinic structure. In this case, the lattice site at the center of the three nitrogen atoms will remain unoccupied, thus accommodating the free electron pairs of the nitrogen atoms [52]. The third possibility is for gaseous N<sub>2</sub> to be incorporated in the nanotube, either intercalated between the graphene sheets or filling the central cavity [53] [47].

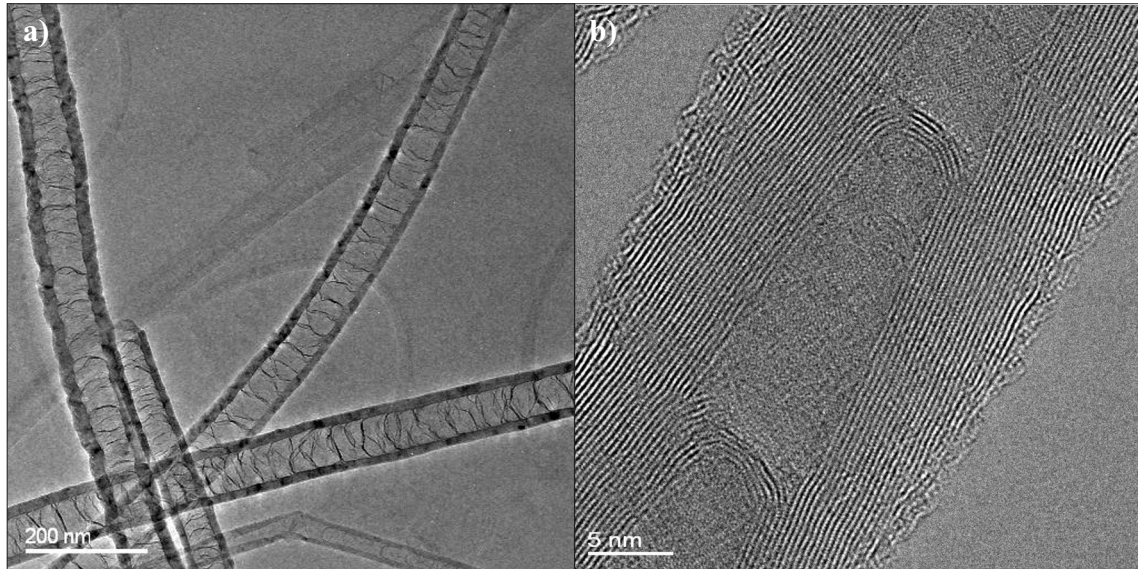


**Figure 2.8:** TEM image of nitrogen doped carbon nanotubes. The nanotubes are divided into several compartments, giving the tube a bamboo-like shape. Courtesy of Dr. Nicole Grobert, unpublished.

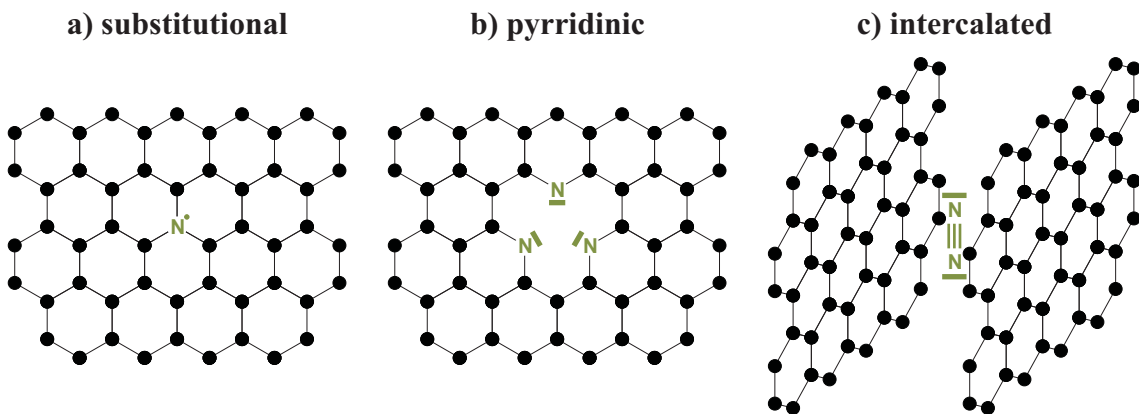


**Figure 2.9:** Different lattice sites for dopant nitrogen atoms: a) a single substitutional atom b) three nitrogen atoms forming a pyridinic structure c) molecular nitrogen intercalated between two graphene sheets.

Nevidomskyy et al. performed calculations using *ab initio* density functional theory to calculate the effect of low-level nitrogen doping on the electronic structure of SWNTs. For metallic armchair tubes, they found a delocalized state. In the case of the semiconducting zigzag-tubes however, the nitrogen energy levels hybridizes with the  $\pi$ -orbitals to form a highly localized state, which is occupied by only one electron. This state is chemically active and permits a reaction with similar states in another nanotube or other ligands [54]. These simulations find support in the work by Jiang et al. who were able to selectively attach gold particles to functionalized

CN<sub>x</sub> [55]. No comparable studies were done for MWNTs. Such chemically active sites were found to increase the wetting of nanotubes by water [56], and may also increase wetting and adhesive forces between nanotubes and metals.

In 2001 Wang et al. measured the bending modulus of nitrogen-doped nanotubes via electrostatic vibrations *in situ* of a TEM. They found a value of 28.6 GPa, but their tubes were so heavily distorted that it was not clear, whether the beam bending equations were still valid [30]. So far, no other measurements on CN<sub>x</sub>-nanotubes have been published. Probably, their values are markedly lower than for the pure carbon ones, if only for the more distorted crystal structure.

## 2.2 Composites

### 2.2.1 Composite theory

An in-depth discussion of composite theory can be found in the textbooks [57]. Therefore, only a short overview with special regard to carbon nanotube-reinforced metals is presented here. Pure metals can have a breaking strain of above 50%, but for alloys this value might be considerably lower and can even approach 1%. For carbon nanotubes on the other hand, the breaking strain was theoretically determined to be as high as 28% (for tensile stress applied parallel to the tube axis), but experimental values are usually around 5%. So although it should in principle be possible to make a composite in which the matrix breaks before the nanotubes, in most cases it will be the other way around. Fig. 2.10 shows the schematic stress-strain-curves for both cases.

#### Reinforcement for strength

To get a strong composite, obviously a large young's modulus and tensile strength of the fiber are desirable. But for discontinuous fibers (which will always be the case with CNTs) the stress transfer to the fiber plays a crucial role as well. As the external load is only applied to the matrix, the force needs to be transferred to the fibers through the interface, if the reinforcement is to have any effect.

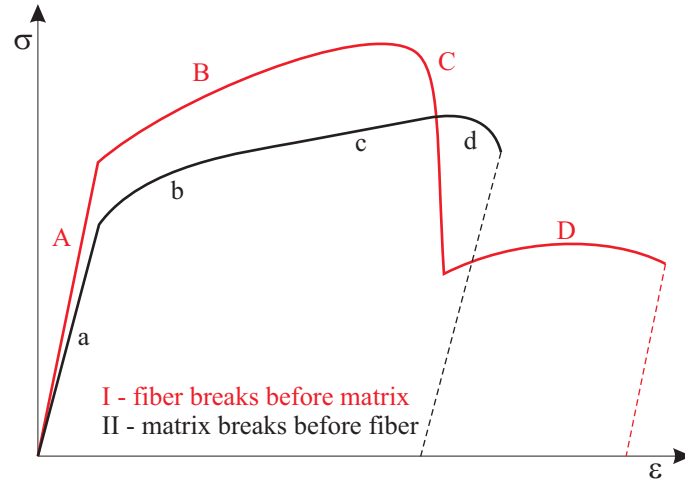


**Figure 2.10:** Schematic representation of the evolution of stress vs. strain in fiber-reinforced composites:

I - fiber breaks before matrix: A - Both fiber and matrix behave elastically. The modulus can be calculated via a rule of mixture. B - The matrix is deforming plastically, the fibers are still elastic. C - The matrix is still plastic, the fibers are breaking. The rounded peak shows that the fibers have a distribution of strengths, i.e. they do not break at the exact same stress. D - All fibers are broken. The matrix remains plastic until the final failure.

II - matrix breaks before fibers: a - Both fiber and matrix are elastic (the difference in slope in comparison with curve I was chosen solely for graphic reasons). b - The matrix is plastic, the fibers elastic. c - The matrix is broken. All stress is carried by the fibers, which are still elastic. d - The fibers break. Again a distribution of fiber strengths is shown.

Only fibers of a length greater than a certain critical length  $l_c$  carry the full stress. This critical length can be calculated using eq. 2.1.

$$\frac{l_c}{d_f} = \frac{\sigma_f(\epsilon_c)}{2\tau_i} \quad (2.1)$$

In this,  $d_f$  denotes the fiber diameter,  $\sigma_f(\epsilon_c)$  the stress in the fiber at a given composite strain, and  $\tau_i$  the interfacial shear stress. This can be determined either by the friction strength between fiber and matrix or by the yield stress of the matrix itself, whichever is lower. From the equation it is obvious that it is the aspect ratio  $\frac{l_c}{d_f}$  rather than the absolute length of the fiber, which determines the amount of stress a fiber can carry. This is due to the fact that the interfacial area scales with the diameter of the fiber.

### Reinforcement for toughness

If the aim of the composite is to increase the fracture toughness, a different approach has to be taken (for in-depth discussion see [58]). Here, it is important that as much energy as possible is dissipated during deformation. For a fiber-reinforced composite, two mechanisms have to be taken into account. When a crack approaches a fiber, the matrix debonds from the fiber. The local stress is then concentrated in the fiber, until the fiber tensile strength is exceeded and the fiber breaks, dissipating the stored elastic energy. This fracture can occur anywhere along the debonded length. As the crack widens further, the fiber is then pulled out of the matrix. During pull-out, more energy is dissipated due to frictional forces.

The pull-out work  $\Delta G_c$  per unit area of fiber is then given by eq. 2.2

$$\Delta G_c = \frac{1}{8} \frac{\tau_i l_d^2 V_f}{d_f} \quad (2.2)$$

In this,  $l_d$  is the debond length, and  $V_f$  the volume fraction of fibers in the composite. If one assumes that the debond length scales with the critical fiber length, as they are both governed by the interfacial strength, this leads to equation 2.3

$$\Delta G_c = \frac{1}{32} \frac{\beta^2 \sigma_f^2 d_f V_f}{\tau_i} \quad (2.3)$$

Here,  $\beta$  is the proportionality factor determining the relation between critical fiber length and debond length and  $\sigma_f$  denotes the tensile strength of the fiber. Therefore, for a high fracture toughness, a low interfacial strength and a high fiber diameter would be preferable.

### Requirements for fibers in MMCs

In comparison with ceramics, most metals are quite tough to begin with. Therefore, metal matrix composites (MMCs) are mainly aimed at high strength and stiffness, rather than at high fracture toughness. To achieve this, a fiber has to fulfill certain criteria:

- high Young's modulus
- high fracture stress and strain

- high aspect ratio
- high interfacial strength
- low absolute length

The Young's modulus, together with the fiber volume fraction, determines the strengthening effect. A high fracture stress will prevent premature fiber breakage. These two requirements are easily fulfilled by carbon nanotubes from what is known today.

Aspect ratio and interfacial strength both determine the load a fiber can carry. Usually, it is argued that the interfacial strength is the biggest drawback of nanotubes. As they present a perfect graphene sheet to the outside, there are no attachment sites for the matrix and the adhesion between the CNT and the matrix should therefore be weak. But this is countered by the very high aspect ratios of carbon nanotubes. The 2.5 mm long SWNTs reported by Hata et al. [3] have an aspect ratio of more than 800,000. Even under the most unfavorable assumptions, i.e. with a high Young's modulus of  $E = 1000$  GPa, the full theoretical breaking strain of  $e_c = 28\%$ , and an interfacial strength as low as  $\tau_i = 0.48$  MPa<sup>1</sup>, the critical aspect ratio reaches only approximately 580.000. Even under these condition, the nanotubes prepared by Hata et al. would be able to carry the full stress.

But even with these large aspect ratios, nanotubes are very short in absolute numbers. Like conventional short fibers, they can therefore be evenly distributed throughout the whole composite, achieving an isotropic reinforcement, while still acting approximately as endless fibers. Other than endless fibers, though, they would not have to be woven into a preform. This combination of interesting properties makes carbon nanotubes an excellent candidate for metal matrix composites. Table 2.3 gives a comparison with some other fibers used in this area today.

---

<sup>1</sup> This is equal to the interplanar shear strength of graphite, corresponding to the sliding of nanotube-shell on nanotube-shell, which is of course not possible in SWNTs.



**Table 2.3:** Fibers used in metal matrix composites

material	E [GPa]	$\sigma_{\max}$ [GPa]	$\rho$ [Mg/m <sup>3</sup> ]	$d_f$ [ $\mu\text{m}$ ] <sup>1</sup>
Al <sub>2</sub> O <sub>3</sub>	380-480	1.4-2.4	3.9-4.0	5-100
Al <sub>2</sub> O whiskers	300-1500	2-20	3.3-3.9	<1
Graphite	390-490	1.5-4.8	1.95-2.2	5-100
Graphite whiskers	700	20	2.2	<1
SiC	380-400	2.4-3.9	2.7-3.4	5-100
SiC whiskers	400-700	3-20	3.2	<1
CNTs <sup>2</sup>	800-1800	10-150	2.1	0.001-0.1

All data according to T. H. Courtney [57] unless marked otherwise.

<sup>1</sup> The values given here are typical [59] but not exclusive.

<sup>2</sup> See tables 2.1 and 2.2.

## 2.2.2 Composites with CNTs

Soon after their discovery, people began to think of carbon nanotubes for reinforcement fibers in composites [60][61]. But the processing proved to be far from simple. A good dispersion and interfacial adhesion is especially difficult to achieve. The first efforts, which were concentrated on polymer matrix composites, have now matured to a point, where the first commercial products are available. The first such product was a tennis racket [62] [63], however, neither the amount of carbon nanotubes in this racket, nor their influence on the mechanical properties are known. Most of the polymer matrix composites, however, are not aimed at the improvement of mechanical properties, but at increasing the electrical conductivity.

Since 1998, several groups have worked on ceramic matrix composites [64][65][66], mainly to increase the fracture toughness. Some promising results were achieved so far, but the composites are still far from commercial application. One study by Xia et al. [17] is of interest as it sheds light on the mechanisms, by which carbon nanotubes deform in a composite. They anodized a thin film of high purity aluminum to generate an amorphous alumina matrix incorporating a hexagonal array of cylindrical pores parallel to the plane normal. Inside these pores, multi-



walled nanotubes were grown, using a CVD process. The result is a composite in which a very regular array of CNTs is incorporated. These composites were stressed by making nano-indentations and the resulting cracks and deformation zones studied in the SEM. The images show not only the classical forms of energy dissipation in fibrous composites (crack deflection, delamination, bridging, pull-out), but also a new mode, in which shear-band-like arrays of collapsed nanotubes were found (see fig. 2.11). Samples exhibiting this mode did not crack and showed high damage tolerance.

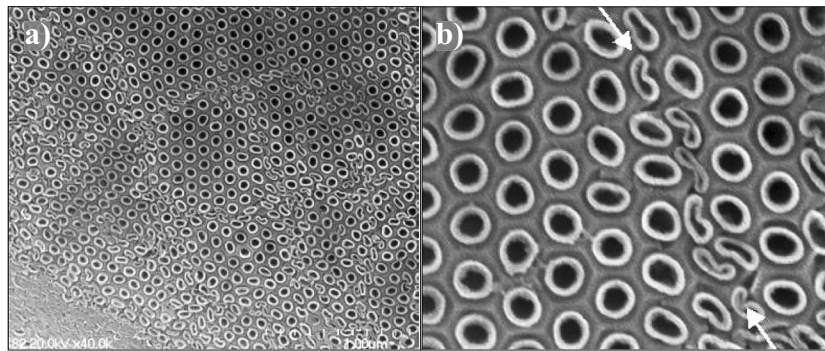


**Figure 2.11:** Carbon nanotube reinforced alumina showing shear-band-like arrays of collapsed nanotubes near a nanoindent [17].

### 2.2.3 Metal matrix composites with CNTs

The study of metal matrix composites reinforced with carbon nanotubes did not begin until the year 2000. The few results which have been published so far are summarized in table 2.4 and discussed in more detail in the following section.

One of the first papers on metal-matrix composites with carbon nanotubes was the one by Kuzumaki et al. [67]. They compared pure titanium with titanium reinforced with 20 vol% of arc-discharge-grown MWNT,  $C_{60}$  or graphite. The CNT-reinforced samples show less porosity than the ones reinforced with graphite or  $C_{60}$ , but they are still not as dense as pure titanium. Some TiC is found in the x-ray-diffraction studies, but this might be due to graphitic particles and amorphous carbon contaminants in the original CNT powder, as TEM investigation showed no carbide formation at the CNT/Ti interface. The microstructure of the reinforced materials is decidedly finer than the one of pure titanium. The CNT-reinforced

**Table 2.4:** Overview of publications on metal matrix composites reinforced with CNTs

author	matrix metal	deposition method
Kuzumaki [67]	Ti	mechanical mixing & hot pressing
Bian [68]	metallic glass	mechanical mixing & casting
Kim [69]	Cu	mechanical mixing & spark plasma sintering
Cha [70]	Cu	molecular mixing & spark plasma sintering
Edtmaier [71]	Cu	electroless plating & hot pressing
Chen [72][73]	Cu	electro-codeposition of metal and CNTs
Chen [74][75][76]	Ni-P, Co	electroless plating
Shi [77]	Ni-P	electro-codeposition of metal and CNTs
Arai[78]	Ni	electro-codeposition of metal and CNTs
Tang [79]	Pt	electrodeposition on carpets

samples have the highest values for both Vicker's hardness and Young's modulus. The Young's modulus is 1.7 times that of the unreinforced material (increasing from 120 GPa to 198 GPa). The change in hardness is even more dramatic (221 HV for the unreinforced material vs. 1216 HV for the CNT-composite). Unfortunately, they do not comment on the influence of the changed microstructure.

Bian et al. [68] investigated metallic glasses ( $Zr_{52.5}Cu_{17.9}Ni_{14.6}Al_{10}Ti_5$ ) reinforced with multi-walled carbon nanotubes. X-ray patterns showed the existence of crystalline ZrC, indicating a reaction between the matrix and the nanotubes. Several elastic constants were determined via ultrasonic measurements (frequency = 10 MHz). In addition the density and the Vicker's hardness (load = 200 g) of the composites were measured. Comparing a sample with 4% CNTs with the unreinforced material, they found an increase in Young's modulus of about 11%. The increase in the compressive modulus was 24% and the increase in the longitudinal attenuation of the ultrasound an astonishing 900%. The density decreased slightly.

Kim et al. used a conventional powder-metallurgic processing to mix nanotubes with nanosized copper-powder. By spark plasma sintering, they were able to reach a relative density of 95% - 100%. In the resulting composite, the nanotubes were found as a dense network at the grain boundaries, with no tubes within the grains.

For nanotube fractions of up to 10%, they found an increase in Vicker's hardness. The hardness decreased slightly, if a nanotube content of 15% was exceeded. They attributed this decrease to the agglomeration of nanotubes at the grain boundaries. The optimum density showed an increase in hardness over the unreinforced sample of 50%, reaching a peak value of 102 kg/mm<sup>2</sup> [69].

The same group later managed to homogeneously distribute the MWNTs within the grains of a copper matrix by molecular level mixing. They dispersed chemically activated (chemically modified to provide attachment sites) nanotubes in a solution of copper acetate, which attached to the tubes upon evaporation of the solute. Subsequent calcination and reduction steps led to copper oxide and then metallic copper. Their micrographs show copper grains with well dispersed nanotubes imbedded in the matrix. As before, they used spark plasma sintering to form a bulk material, in which they measured an increase of more than 200% in the yield stress of a sample reinforced with 10% MWNTs as compared to the pure copper sample[70].

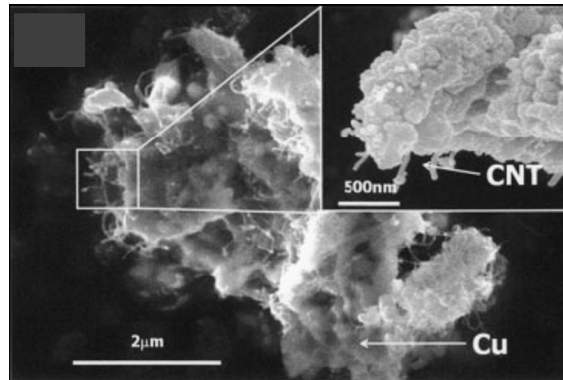


**Figure 2.12:** Copper-carbon nanotube composite produced via molecular level mixing. The nanotubes are homogeneously dispersed throughout the copper grains [70].

Besides the classical methods of metallurgy and powder-metallurgy, methods of electrodeposition and electroless (i.e. chemical) plating are gaining increasing influence. For the electroless plating, several steps of cleaning and chemical surface activation are needed, before a metal (Ni-P [74][75], Co [76]) can be deposited from an aqueous solution. If the conditions are well-controlled, a very homogeneous plating of the nanotubes can be achieved, but it is difficult to build a monolithic composite. For this reason, Edtmaier et al. [71] used a hot-pressing step after depositing copper on MWNTs by electroless plating to make copper/nanotube heat-

sinks. Results from measurements of mechanical and thermal properties of these composites have not yet been published. A different approach was taken by Dong et al. First, they plated carbon nanotubes with nickel in an electroless process. They then used classical powder metallurgy to incorporate these coated nanotubes in a copper matrix.[80]

These copper-matrix composites were tested for wear resistance, as were those prepared by the group of Chen [72]. Instead of an electroless process, they used electrodeposition to deposit nickel or nickel phosphide coatings reinforced with carbon nanotubes. Both types of samples (Cu as well as Ni) showed increased wear resistance combined with a lower friction coefficient. Micrographs of the sample surface after the testing showed large numbers of nanotubes sticking out of the surface. The low friction coefficient is then attributed to a solid lubricating effect of the graphite-like nanotubes. To have this effect, the nanotubes should show weak adhesion to the matrix, and indeed the free ends of the nanotubes appear to be free of metal. On the other hand, the increase in wear resistance indicates a hardening effect of the nanotubes, which would point to a finite interfacial strength.

Although metals can be deposited on carbon nanotubes without any prior treatment, it is usually necessary to chemically activate nanotubes to keep them in dispersion in the electrolytic bath. Even so, it is not possible to increase the amount of nanotubes in the composite by increasing the nanotube concentration in the bath. Actually, the opposite is often the case, which is attributed to the formation of agglomerates in the solution, once a certain threshold concentration is reached. As these agglomerates are not incorporated into the composite, the actual nanotube density decreases [73][77].

While all the work described so far used nanotubes dispersed in a solution, Tang et al. deposited platinum directly onto well-oriented nanotube carpets produced by CVD (see p. 35). After deposition of the metal, the formerly perfectly aligned and widely spaced nanotubes, touched at the tips to form tripod-like structures (fig. 2.13). As the samples were intended as catalysts for the oxidation of methanol, a large surface area was desirable and no dense composites were prepared. [79]

Finally, the work of Arai et al. should be mentioned. When depositing nickel

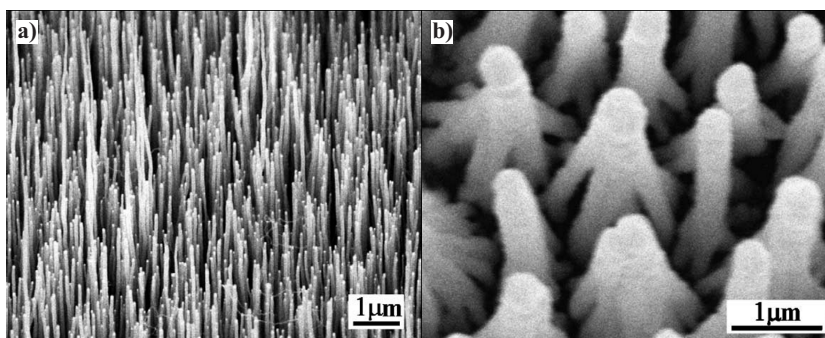


**Figure 2.13:** Pt/nanotube composite catalysts from the work of Tang et al: a) before the electrodeposition the nanotubes are perfectly aligned and loosely spaced. b) After the deposition the tips of several nanotubes are connected to form tripod-like structures [79].

on multi-walled carbon nanotubes, they found a "skewered-dumpling" shape. The deposition took place at a few selected sites along the length of the nanotubes and especially at the ends. With longer deposition times, these metal particles grew in size without ever fully enclosing the nanotube. The sites, where the deposition started, were probably defects on the outer shell of the nanotube. The adhesion between nickel and nanotubes was strong enough that they did not separate upon removing from the substrate. When the powder was ultrasonicated, however, some of the nanotubes detached from the particles, without any signs of plasticity in the metal. [78]

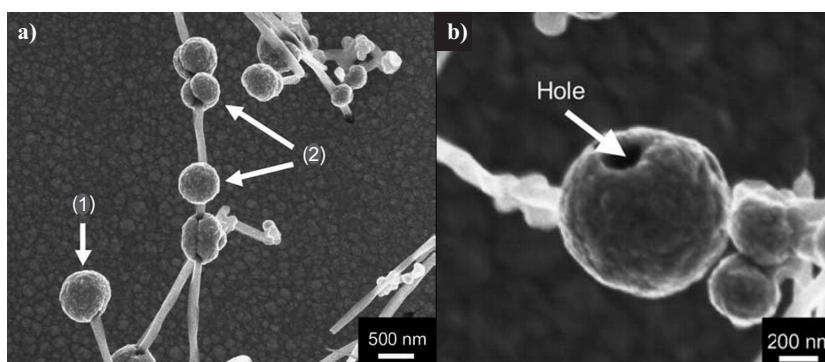


**Figure 2.14:** Carbon nanotubes with nickel particles showing a "skewered-dumpling" shape. a) The particles from typically at the ends (1) and at defect sites (2). b) After ultrasonication, some of the nanotubes have broken out, leaving circular holes. Images by Arai et al. [78].

## 2.3 Motivation

Carbon nanotubes are a very young field of study and although much effort has gone into it, many questions are still unsolved. One of the most important problems is how to produce nanotubes with given characteristics like length, diameter, chirality, and defect density. In correlation with this, it is still not clear how the properties - both mechanical and electronic - are influenced by the same characteristics.

On the other hand, although there is still great variation in the values determined for the mechanical properties of carbon nanotubes, it is obvious that CNTs are very interesting as reinforcement fibers for metal matrix composites. Such composites have been the object of study since the year 2000 approximately. Work published so far focuses on the synthesis methods and the change in macroscopic properties. The fundamentals of the interaction of carbon nanotubes with a metal matrix are, however, for the most part still unknown.

The high production costs of composite materials and the high price of carbon nanotubes (40,000\$/kg [81]) make carbon nanotube-reinforced MMCs predestined for high-end applications. In these applications, safety margins are usually small. A thorough understanding of the material and the fundamental mechanisms governing its behavior is therefore of tremendous importance to correctly predict the components properties and failure probabilities. Some of the questions to be solved are as follows:

- What are the mechanisms by which CNTs strengthen metals?
- What is the chemistry of the interface?
- Is there a stress transfer from the matrix to the nanotube and if so, to which extend?

Especially the last question is of great interest as all modes of deformation are influenced by it. In the elastic regime, the stress transfer at the interface determines how much of the external load is carried by the fibers, thus affecting the young's modulus of the composite directly. In the plastic regime again, the force distribution between fiber and matrix influences yield stress and tensile strength. Finally during

failure of the sample, the interfacial strength and friction determines the toughness of the sample.

Given the small size of carbon nanotubes, micromechanical testing methods have to be employed. These methods were developed for thin film mechanics, especially in connection with microelectronics and MEMS, so they have to be adapted to the investigation of composite materials. In addition, the composites best suited for these studies are not necessarily the ones best suited for macroscopical application. Therefore, new model composites have to be developed.





## Chapter 3

# Carbon nanotubes enclosed in sputtered copper films - a model composite

### 3.1 Motivation

For several years now, carbon nanotubes have been discussed as interesting reinforcing fibers for metal matrix composites. The first composites fabricated exhibited some very promising properties [67] [75]. Yet it is still unclear, how nanotubes interact with a metal matrix. A model composite would be desirable to study the metal/CNT interface and thereby gain insight into the composite's mechanical properties. To that end Cu-CNT composite films were developed using two different methods. In this chapter, the technique to fabricate composites of a CNT layer between sputtered copper films is explained and the composite evaluated.

Due to the small size of carbon nanotubes, an investigation of their interactions with a metal matrix requires TEM analysis. Using a metal with a rather low atomic number eases the restraint on the sample thickness necessary to achieve electron transparency. Furthermore, the matrix should be as pure as possible to exclude any effects from impurities or precipitates. The metal should also be oxidation resistant. For these reasons, copper was chosen as a matrix material. The principal idea behind the sample preparation was as follows (see also fig. 3.1). First, a copper

film is deposited on a silicon wafer using magnetron sputtering, carbon nanotubes are then deposited onto the copper layer (by a method which should ensure a high density of nanotubes, a good separation of the individual tubes as well as a clean copper surface) and a second copper layer is sputtered to enclose the nanotubes at the interface of the two layers. Details regarding CNT synthesis, the deposition of the CNT layer and the composite analysis are discussed in this chapter.

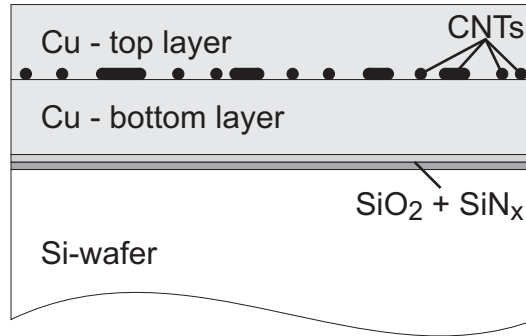


**Figure 3.1:** Schematic cross-section of a composite made from nanotubes enclosed between two sputtered copper layers. The nanotubes are randomly oriented within the plane of the interface.

## 3.2 Experimental Procedure

### 3.2.1 Synthesis of CNTs

The carbon nanotubes for this work were produced using an aerosol-CVD process, similar to the one used by Mayne et al. [11]. The precursor used was benzyl amine with 5 wt% ferrocene for producing nitrogen doped nanotubes. Doped nanotubes were chosen over pure carbon tubes to provide more attachment sites for the matrix. The solution was filled into the aerosol generator shown in fig. 3.2, where an piezoelectric actuator forms the aerosol or fog via ultrasonic energy. This aerosol is then conveyed through the setup by a stream of argon gas.

The precursor decomposes in the furnace, shown schematically in fig. 3.3. Small iron particles form, which act as catalyst for the nanotube formation. Two bubblers are used to clean the exhaust. The first one is empty and collects any dry contaminants, while the second one is filled with acetone and cooled with liquid nitrogen

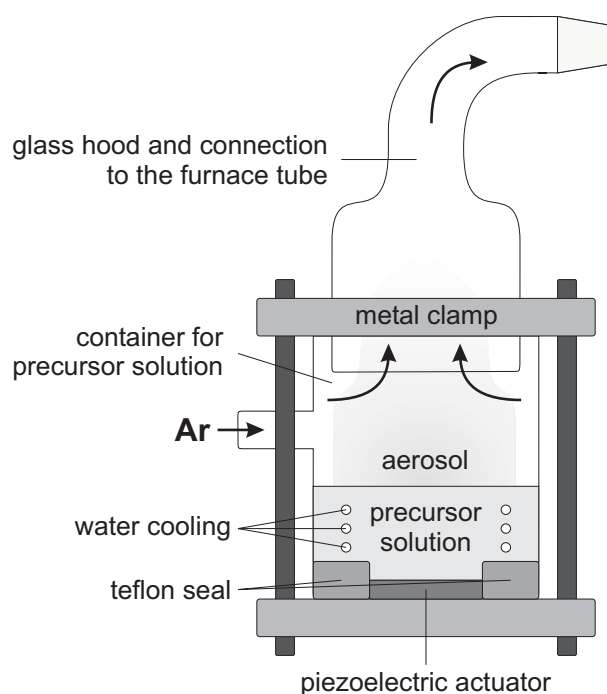


**Figure 3.2:** Schematic drawing of the aerosol-generator.

to wash any remaining organic solvents out of the gas stream. Finally, the gas is released to the fume hood vent.

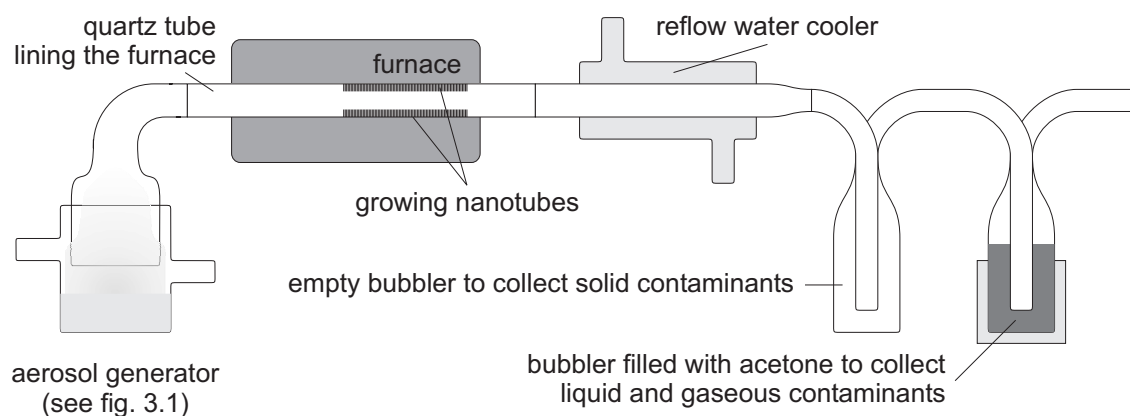


**Figure 3.3:** Schematic drawing of the CVD-setup for the production of carbon nanotubes.

The aerosol-stream was kept for 30 minutes at temperatures of 800°C, 850°C or 900°C. See table 3.1 for the average dimensions of the nanotubes and the yield of nanotube powder in respect to the synthesis temperature. After that time, the piezo actuator was switched off and the furnace cooled down. The quartz tube lining the furnace was then scraped out to collect the nanotubes. The samples were characterized with SEM and TEM. All of them were very clean, with hardly any soot

or other carbonaceous species. Thus, no cleaning step was necessary. TEM showed the samples to have the typical bamboo-structure of nitrogen-doped nanotubes.

**Table 3.1:** samples of nitrogen-doped carbon nanotubes used in this study

Sample	Synth. Temp. $T_s$	av. length $\bar{l}$	av. diameter $\bar{d}$	yield
1	800°C	87.3 $\mu\text{m}$	52.6 nm	265.35 mg
2	850°C	117.3 $\mu\text{m}$	33.0 nm	300.65 mg
3	900°C	101.1 $\mu\text{m}$	49.5 nm	328.10 mg

### 3.2.2 Parameters for the deposition of the copper layers

The copper layers were deposited using DC-magnetron sputtering. For the bottom layer a ultra high vacuum system (UHV), for the top layer a high vacuum system (HV) was used. This was done to avoid carbon contamination from the nanotubes in the UHV system. As substrate silicon wafers (100- or 111-oriented) were used, which were coated with 50 nm each of  $\text{SiO}_2$  and  $\text{SiN}_x$ . Before deposition of the bottom layer, the substrate was sputter cleaned for 1 min at 84 W. This was not done before deposition of the top layer, so as not to destroy the carbon nanotubes on the sample surface. Table 3.2 gives the parameters used for copper deposition in both systems. The thicknesses and corresponding sputter times are exemplary, as samples with different layer thicknesses were fabricated.

**Table 3.2:** Parameters for DC-magnetron sputtering

	bottom layer (UHV)	top layer (HV)
thickness	300 nm	200 nm
chamber vacuum	$5 \times 10^{-8}$ mbar	$5 \times 10^{-7}$
sputter time	5 min at 250 W	5 min at 100 W
target purity	5N	5N
distance target-substrate	20 cm	12 cm
temperature	RT	RT

### 3.2.3 Deposition of nanotubes

The handling of nanotubes is difficult. Due to their small size, they cannot be manipulated individually without the use of an atomic force microscope or a similar instrument. They experience large inter-tube attractive forces due to Van-der-Waals-interactions and their high flexibility makes them prone to entanglement, thus making it hard to suspend them in a liquid phase. Several different approaches were taken, before the optimum parameters for the deposition of nanotubes were found. These experiments together with a short summary of the samples that resulted will be presented here in an overview. The method used for the final samples is presented on p. 59.

### 3.2.4 Dispersing nanotubes

Nanotubes do not form a stable dispersion readily. For the present work, it was necessary to find a solvent, which could keep as many nanotubes as possible in a dispersion stable for a reasonable time span, while not leaving any residue on the wafer surface. Five different solvents were tested (see fig. 3.4). Each of the glasses contains approximately 6.4 ml of solvent and 0.1 - 0.2  $\mu\text{g}$  of  $\text{CN}_x$ -powder. From left to right, these solvents are: a 1% solution of sodium dodecyl sulfate (SDS) in water, toluene, benzene, acetone, and ethanol. As can be easily seen, even at these low concentrations, the nanotubes form a tangled network, instead of a uniform dispersion. Still, SDS, toluene, and ethanol were slightly better than benzene and acetone.

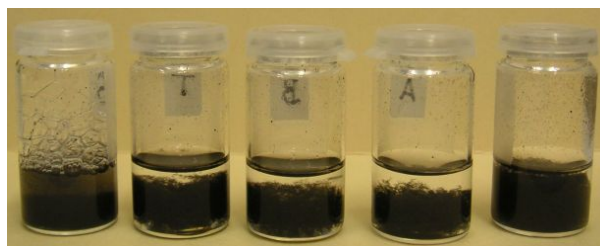


**Figure 3.4:** Solvents tested for nanotube solubility. From left to right: SDS, toluene, benzene, acetone, ethanol.

### 3.2.5 Deposition Methods

Many experiments were run to determine the best way to deposit nanotubes on the copper-covered wafer. The main objective here was to find a method to deposit a high density of nanotubes without forming tangles or agglomerations.

#### Method 1 - blow-drying

The first method tried was found in the literature [82]. The nanotubes were dispersed in a solution of 1% SDS in water. The wafer was immersed in this dispersion for 10 to 240 minutes, dried in an air stream, rinsed in deionized water, and dried again. Unfortunately, with MWNTs on a copper-coated wafer, the results of Lay et al. could not be duplicated. This was probably due to the different surface chemistry as they used SWNTs and an amine-functionalized silicon wafer. Neither the high densities nor the large scale alignment of the nanotubes were observed. Instead, the density was very low, with no discernible alignment. Furthermore, the copper was oxidized in some areas and large quantities of organic residue had formed. The dark regions in fig. 3.5 are the residue typically observed. On the other hand, nanotubes were very infrequently observed. Most of the other images do not show any nanotubes.

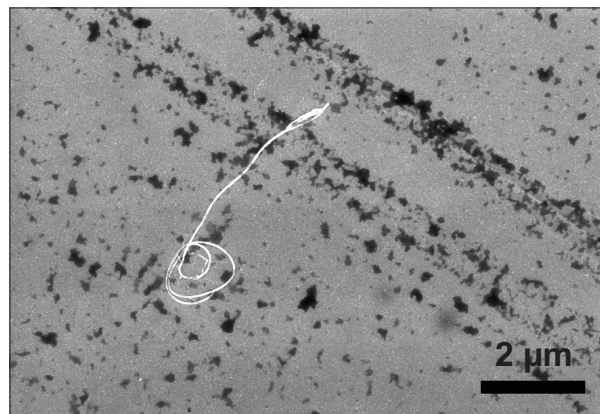


**Figure 3.5:** Wafer prepared according to the procedure as described by Lay et al.[82].

#### Method 2 - evaporation

To increase the nanotube density, wafers were left in the solution until all liquid had evaporated. This resulted in a huge amount of nanotubes being deposited on

the wafer, as can be seen in fig. 3.6. With such a high nanotube density, it is not possible to make a dense composite. In addition, the nanotube distribution was very non uniform. There were regions with no or few nanotubes next to areas with dense three-dimensional networks.

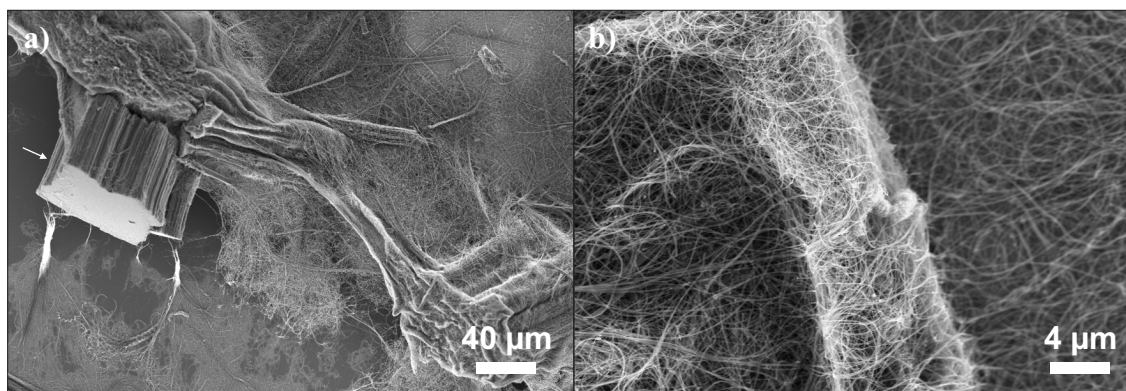


**Figure 3.6:** Images from a wafer prepared by the solution-drying method. A three-dimensional network of nanotubes with highly varying local density has formed. The block marked by an arrow in a) is an undissolved flake of the as synthesized nanotubes. (solvent: acetone)

### Method 3 - drop drying

To decrease the amount of nanotubes deposited, the next samples were not immersed in the dispersion. Instead, some drops of dispersion were dripped onto the wafer and left to dry. As planned, there were fewer nanotubes on these samples. But as long as there was some liquid left, the nanotubes were very mobile, and immediately formed large agglomerates, which lead to a very inhomogeneous distribution of nanotubes on the sample. Fig. 3.7 shows the edge of such an agglomerate. The solvent in this sample was toluene. As can be seen in the image, the dispersion contained a large amount of organic impurities, which formed a residue especially around the nanotube-agglomerates.

### Conclusions from deposition experiments

Of the five solvents tested, acetone and benzene showed a poor dispersing ability for MWNTs and were therefore ruled out. The remaining three solvents SDS, toluene, and ethanol, were similar in their dispersing abilities. SDS and toluene led to organic residues on the copper film. Ethanol, while being able to disperse only a small



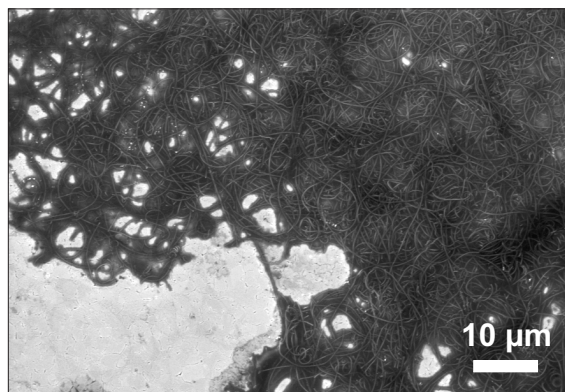


**Figure 3.7:** Wafer prepared by the drop-drying method. While still in dispersion, the nanotubes formed large tangles. Impurities in the solvent (toluene) led to a pronounced film of organic residue.

concentration of nanotubes, nevertheless left the cleanest wafer surface and was therefore chosen for further studies.

This set of experiments revealed that it was imperative to have as little liquid as possible in contact with the wafer at any given time, as the free movement of  $CN_x$  in the dispersion led to entanglements and large agglomerates. Also, the wafer could not be rinsed after deposition, since this led to a very small concentration of nanotubes.

### Final method - cyclic spray-drying

The following method, devised to give the nanotubes as little room to move as possible, resulted the best distribution of NTs and minimized the amount of residue on the copper film. A dilute dispersion of  $CN_x$  in ethanol was prepared and poured into a small spraying flask. When shaken, the nanotubes remained dispersed for about 30 seconds. One use of this flask covered the sample with a thin film of dispersion, which would be left to dry. To increase the nanotube density, several cycles of spraying and drying were performed.

## 3.3 Results

Samples prepared by the cyclic spray-drying method were analyzed further. Samples without the top layer were used to study nanotube density and the cleanliness of



the interface, whereas samples with top layer were used to evaluate the porosity of such samples.

### 3.3.1 Quality of nanotube dispersion

Fig. 3.8 shows the wafers after different numbers of spraying cycles. Both the nanotube density and the amount of organic residue increase with the number of cycles. For each sample a total area of approximately  $0.4 \text{ mm}^2$  was evaluated. Care was taken to select sites which were representative of the sample as a whole. The results are shown in fig. 3.9. To cover a large area, rather low magnifications were chosen. This entails that very small nanotubes ( $d < \text{approx. } 25 \text{ nm}$ ) might be missed and the numbers shown are actually lower boundaries. As expected, the nanotube density increases linearly with number of cycles. A number of 16 cycles was found to be the best compromise between a high nanotube density and a clean sample.

Most of the nanotubes deposited were well separated from each other, however, small agglomerations were found in a few places as shown in fig. 3.10.

### 3.3.2 Conformity

After depositing the second copper layer, the nanotubes are still visible at the sample surface as long as the films are not annealed after deposition (see fig. 3.11). Actually, they are more easily discernible, due to the conformity of the sputtering process, which enhances the surface topography around the nanotube. The copper forms a raised mound on the sample surface directly above the nanotube. This mound has approximately the same height as the nanotube, but can be up to twice as wide. Examples for such mounds can be seen in figs. 3.12 and 3.13. The greater width as well as the higher atomic number of copper in relation to carbon gives a marked increase in contrast. The difference in visibility is reflected in the steeper slope of the copper-coated samples in relation to the uncoated ones as shown in fig. 3.9. During annealing, these mounds flatten, and lose their well defined edges due to grain growth. The nanotubes are then very hard to locate.

As the buried nanotubes can be easily seen from the sample surface, it is possible to make cross sections at specific sites using a focused ion beam microscope (FIB).

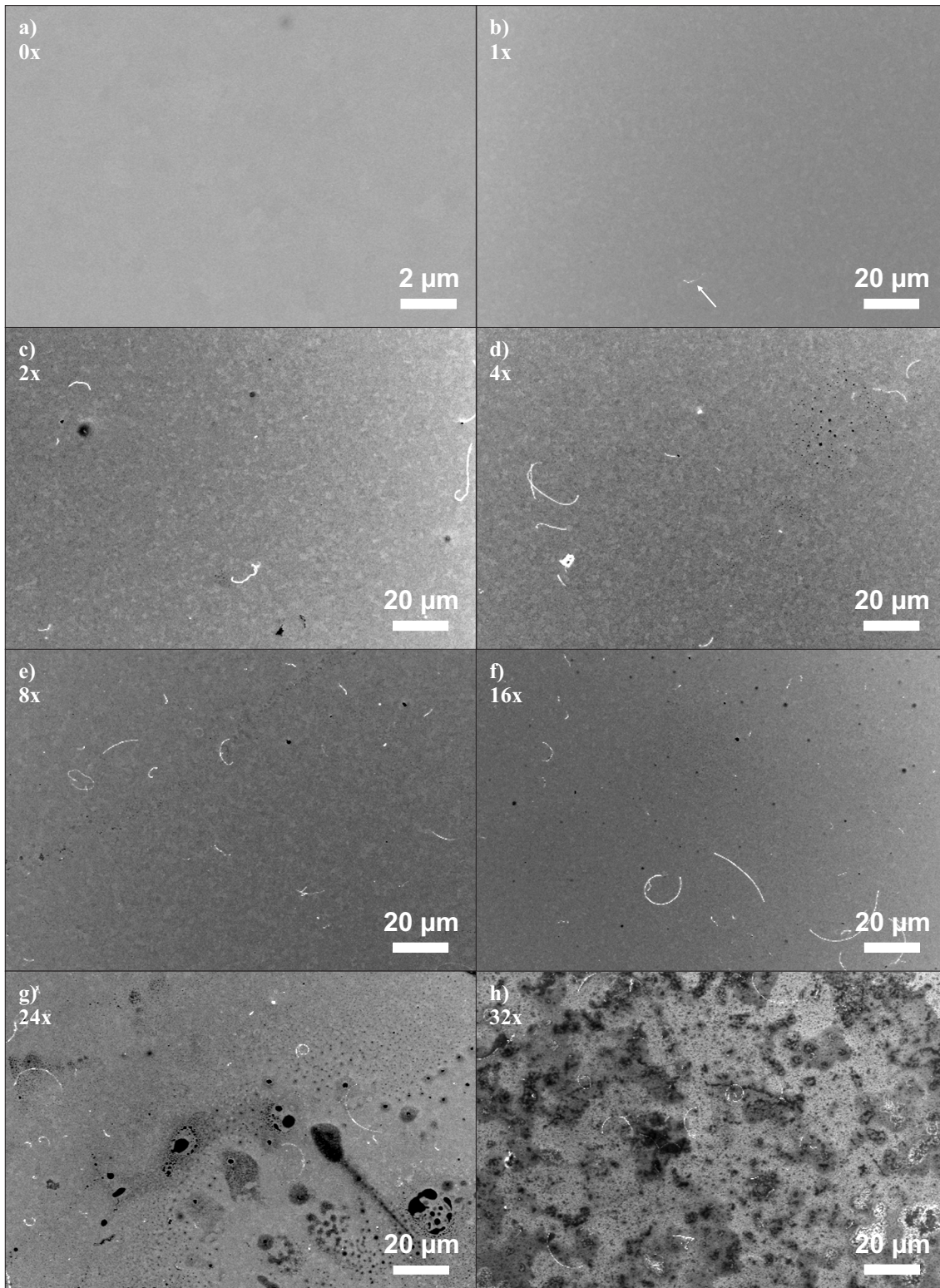


**Figure 3.8:** Development of wafer cleanliness and nanotube density with increasing number of spraying cycles. Note the different magnification of the image of the pristine wafer (a).

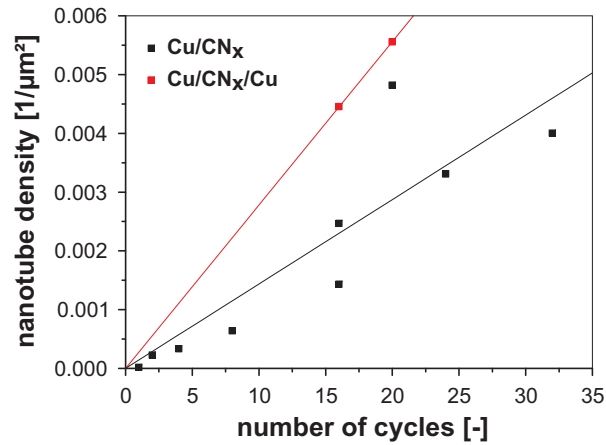


**Figure 3.9:** Nanotube density vs. the number of spraying cycles. Since the nanotube visibility is improved by the top copper layer, the slope is steeper for the covered samples (red).

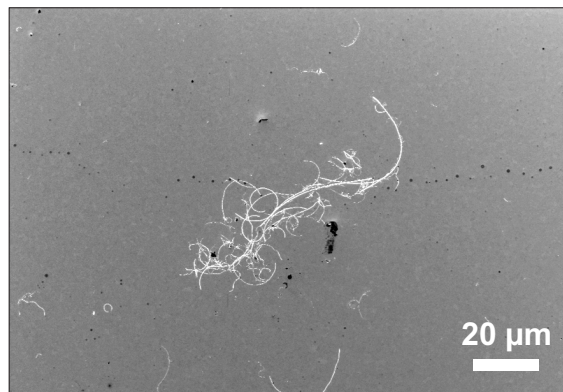


**Figure 3.10:** Agglomeration of nanotubes on a wafer prepared by the cyclic spraying method.

Two such images are shown in fig. 3.12. The first one shows a site, where the nanotubes were lying flat on the underlying copper film; these nanotubes are completely enclosed by copper. In the second one, the nanotubes were raised above the surface, as a result of tangling; in this spot, the copper was not able to completely fill the space underneath the nanotubes, thus leaving a cavity.

It is also possible to cut a TEM specimen directly from the composite film, using FIB. Images from such a sample are shown in fig. 3.13. From top to bottom, the following layers can be distinguished: The dark tungsten layer at the top was *in situ* deposited to protect the specimen surface during the cutting process. Below is the second copper layer, approximately 700 nm thick. Below that is the first copper layer (300 nm). A nanotube lies at the interface between the two layers. Finally, a thin film of silicon nitride and silicon oxide coat the silicon surface. This image shows once again the remarkable conformity of the sputtering process. The height of the



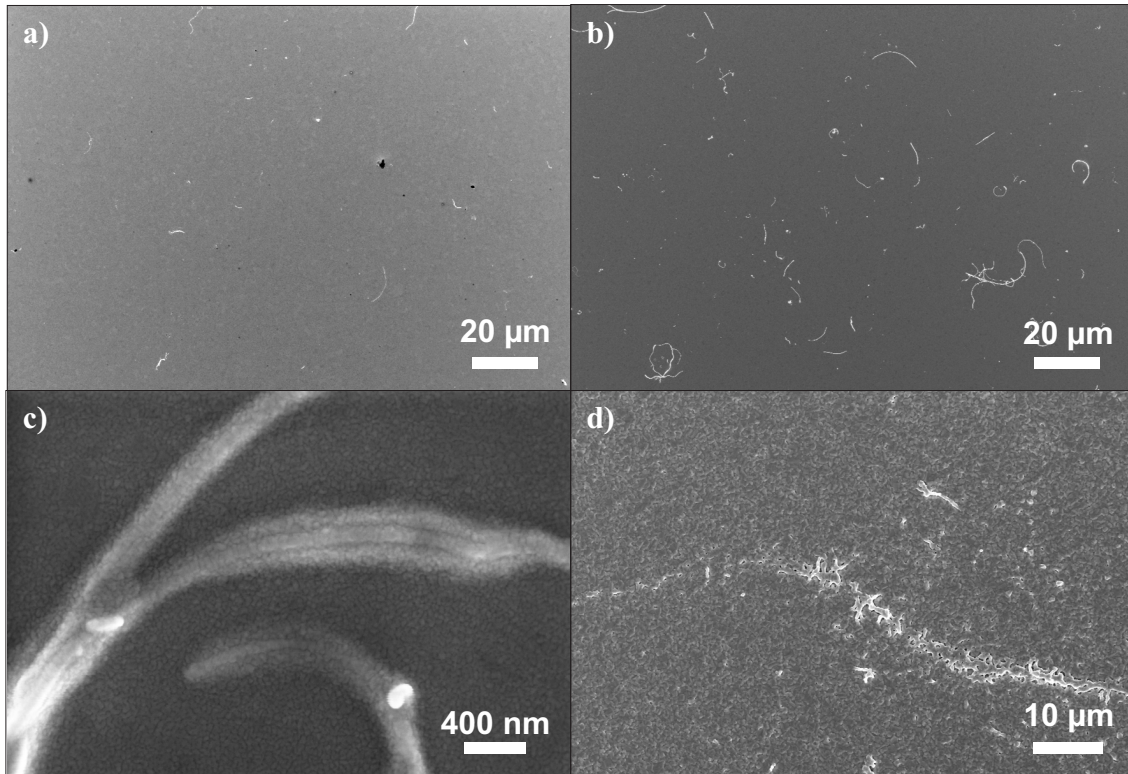


**Figure 3.11:** Appearance of Cu/CNT/Cu-sandwich wafers. a) no second copper layer. Visibility of nanotubes is poor. b) with second copper layer (300nm). The nanotubes are much better discernible. c) wafer with a very thin (100 nm) copper top-layer. The nanotubes are visible through the copper. d) wafer with 1000 nm top-layer after annealing at 350°C for 30 minutes. The nanotubes under the copper film is more difficult to see.

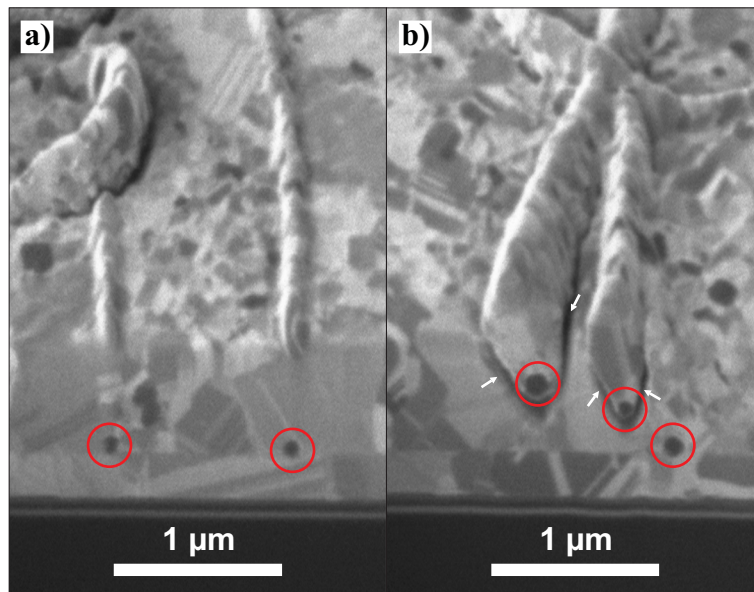


**Figure 3.12:** Cross section (FIB) of a wafer with a 1  $\mu\text{m}$ -thick copper top layer. When nanotubes lie flat on the surface of the underlying copper film, they are well enclosed by copper. b) If the nanotubes are tangled or raised above the surface, cavities (indicated by arrows) may form due to shadowing effects.

bulge at the sample surface has hardly decreased with respect to the height of the nanotube itself. Both are approximately 120 nm. The width of the bulge has nearly doubled from 150 nm to 280 nm. There is evidence of an organic residue at the interface between the nanotube and the bottom copper layer. On closer inspection, this light "crescent" underneath the nanotube is also mainly copper, as well ordered atomic planes - although with a weak contrast - can be seen here. Only small parts of the crescent appear to be amorphous, and are probably due to residue from the solvent. In contrast, the top of the nanotube is perfectly clean, with the copper crystal planes in close contact with the nanotube itself.

In the FIB, only one nanotube was visible, but TEM analysis revealed that there are actually two. The second, much smaller one is situated at the top left of the larger one, in the lighter area indicated by the left arrow in fig. 3.13a. A closeup of the larger tube shows the wavy yet concentric rings of the  $CN_x$ -graphene shells (see fig. 3.13b) as well as the copper crystal planes. This proves that the nanotube has been cut nearly perpendicular to the tube axis, and indeed the hollow core of the nanotube is clearly visible. The smaller tube, however, was cut at a different angle. Here, the images show overlapping rings of weaker contrast.

### 3.4 Discussion and Outlook

A process has been demonstrated by which carbon nanotubes can be incorporated in thin metal films. The nanotubes are well imbedded, with no cavities due to shadowing effects, provided they lie flat on the underlying copper film. Increasing the number of spraying cycles increases the density of nanotubes but also the amount of residue from the organic solvent. However, the sample can be kept reasonably clean, if the number of spraying cycles is not too high. The nanotube density achieved that way is rather low, which makes the samples unsuitable for macroscopic measurements, yet they are very well suited for microscopic measurements or *in situ* experiments in an electron microscope.

The high conformity of the sputtering process makes it possible to see the nanotubes, even when they are lying underneath a copper layer of 1  $\mu\text{m}$ . Using FIB, cross-sections and TEM specimens can thus be made at any desired angle to the

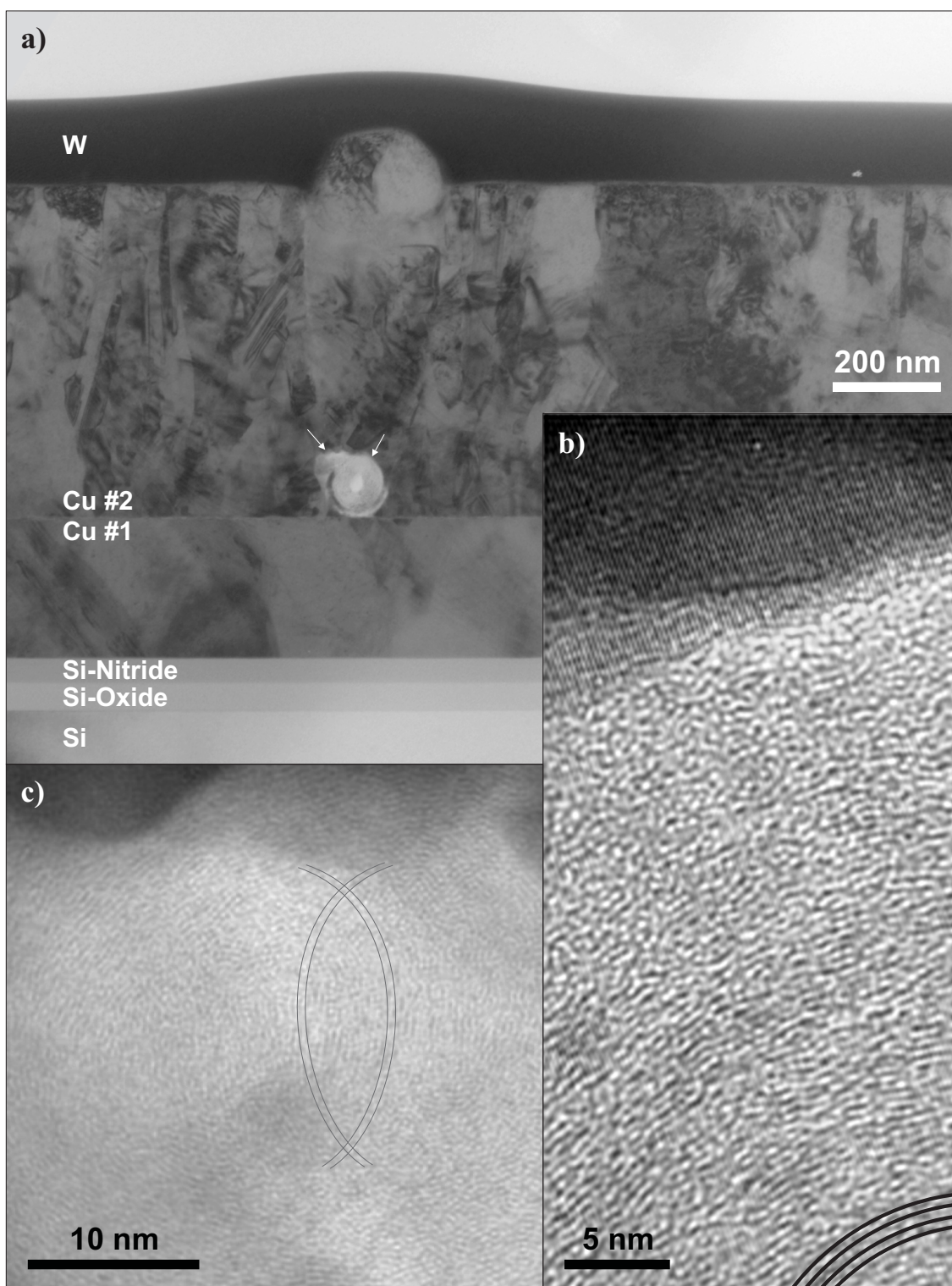


**Figure 3.13:** TEM image of a nanotube at the interface of the two copper layers. a) The nanotube is well enclosed by copper with no organic residue at the top and only little below. In the lighter area indicated by the left arrow, a second, smaller nanotube lies flat against the bigger one. b) Close-up of the interface between matrix and bigger nanotube (right arrow). c) Close-up of the smaller nanotube.

---

tube axis. In particular, samples cut under an angle of  $90^\circ$  are well suited to the study of interfacial reactions, as there is no overlap between nanotube and matrix in these samples. This is especially important for EDX or EELS measurements. Unfortunately, such measurements could not be made with the TEM sample presented here, as it was at first too thick for these techniques and was then completely destroyed during further thinning.





## Chapter 4

# Microcolumns from a Cu/CN<sub>x</sub> composite: compression testing and TEM analysis

### 4.1 Introduction

In the model composite presented in the last chapter, the nanotubes are all aligned in one plane (the interface between the two copper layers). Most of the nanotubes are well separated, with few tangles and little contamination. Using a sputtering process for the deposition of the matrix, on the other hand, ensures a high purity of the matrix material. This composite is therefore well suited to study the interaction between carbon nanotubes and a metal matrix. However, as the overall nanotube density is low, a method has to be used which allows to test small volumes of the composite.

One such method has been introduced by Uchic et al. in 2004 [83]. They used a focused ion beam microscope to mill columns of diameters between 0.5 and 40  $\mu\text{m}$  (aspect ratio between 2:1 and 4:1) out of macroscopic single crystals of pure nickel. They then tested these columns in a nanoindenter equipped with a flat punch instead of a sharp indenter tip. The bulk sample, to which the column is still attached, acts as a counter bearing, thus the test closely resembles a conventional compression test. The only difference is that the column is fixed at the lower end.

Following this first publication, other groups began to employ this technique as well. So far, results have been published for pure nickel [84], Ni<sub>3</sub>Al, nickel super alloys and gold. The findings closely resemble each other. All groups find a noticeable strengthening effect for very small columns ( $d < \text{approx. } 5 \mu\text{m}$ ), which is usually attributed to dislocation starvation. After an elastic regime with a gradual onset of plasticity, discrete strain bursts are observed for these columns, whereas the larger ones show a smooth curve. Often, these strain bursts alternate with almost elastic behavior. This shape of the curve is usually explained by one slip event triggering an avalanche of dislocations, often on the same slip plane. Sometimes, the number of strain bursts can even be correlated with the number of slip traces found in the SEM analysis of the columns after testing [85].

Recently, TEM samples have been prepared from deformed columns [86]. In agreement with hardening through dislocation starvation, no mobile dislocations were found in an orientation suitable to relieve the compressive stresses. A small but noticeable damaging of the TEM sample through the FIB milling was reported, leading to small dislocation loops at the surface of the TEM lamella.

FIB induced damage to the column surface has been discussed as being responsible for the observed size effect. However, recently both Greer [86] and Volkert [87] have concluded from their experiments that although a gallium enriched layer is usually present at the sample surface, its influence on the deformation behavior of the samples is negligible. The brittle layer often observed in the SEM micrographs of the column surface after testing is probably not due to ion implanting, but rather carbon contamination caused by the SEM imaging done before testing.

In 2006 Zhang et al. have published results from extensive finite elements simulations, in which they studied the influence of several parameters of the column shape on the reliability of the stress-strain behavior measured [88].

- If the ratio of the fillet radius (at the bottom of the column) to the column is large, stresses in the plastic regime are overestimated. On the other hand, if it is small, i.e. if the corner between substrate and column is sharp, stress concentrations occur, which can lead to premature failure. This is only the case, if the base is made of the same material as the column itself.

- Plastic buckling is suppressed in columns with aspect ratios  $\leq 5$  by friction between the indenter tip and the column top. Euler buckling would require even larger aspect ratios. To ensure a mostly homogeneous stress state, aspect ratios between 2 and 3 are recommended.
- Tapering of the columns, i.e. a smaller diameter at the top than at the bottom, results in overestimation of the Young's modulus and strain hardening.
- Misalignment between the column top surface and the flat punch leads to underestimation of the Young's modulus and may result in buckling of the pillar.

Compression tests of micron-sized columns are a promising method to investigate the interaction of carbon nanotubes and the copper matrix in the model composite presented in the last chapter. The use of the FIB to fabricate the columns makes it possible to spot the carbon nanotubes and thus to alleviate the effects of the low nanotube density to some extent. The sample geometry achieved by FIB milling also makes up for the lack of positioning accuracy of the nanoindenter used for the actual compression experiment, as it ensures the exact position of the column with regard to the nanotube. The column then can be located in the optical microscope, even though the nanotube itself remains invisible. A wide trench milled out around the column and the construction of the nanoindenter, which prevents tilting of the flat punch, ensure that only the column is tested and that this is done under controlled conditions. In addition, the columnar geometry makes the evaluation of the force-displacement curves straightforward in comparison to e.g. nanoindentation.

The nanotube density in these samples is still rather low, so that a noticeable effect on the overall deformation behavior is not expected. However, microscopic studies are much facilitated as the deformation is concentrated in a small volume. This is especially the case for TEM studies as TEM samples are always very small. Using micron sized pillars, the entire sample - although thinned for increased electron transparency - can be studied in the TEM.

## 4.2 Experimental procedure

A sample with nitrogen-doped MWNTs embedded between two DC-magnetron sputtered copper layers was prepared on a silicon wafer (coated with 50 nm each of SiO<sub>2</sub> and SiN<sub>x</sub>) using the routine described in the previous chapter, differing only in the fact that both films were done in the high-vacuum sputter chamber. After sputtering, the sample was annealed at 300°C for 30 min to induce grain growth. As annealing lessens the contrast of the underlying nanotubes at the sample surface to a high degree, it was not always possible to decide which area contained nanotubes.

### 4.2.1 Preparation of micron-sized columns

In cooperation with the Forschungszentrum Karlsruhe, columns with a diameter of approx. 500 nm were cut out of this film using a 30 keV dual beam FIB (Nova NanoLab by FEI). To avoid any artefacts due to fillet radius, and to obtain a stiff counter bearing, the columns were cut well into the silicon. Unlike in the work of Uchic et al. [85] the sample was not rotated during the cutting process. The sides of the columns are therefore not perfectly parallel, and the columns are slightly thicker at the bottom, with a tapering angle  $\alpha$  of approx. 4° (see fig. 4.1A). A detailed description of the cutting process can be found in the work by Volkert et al. [87].

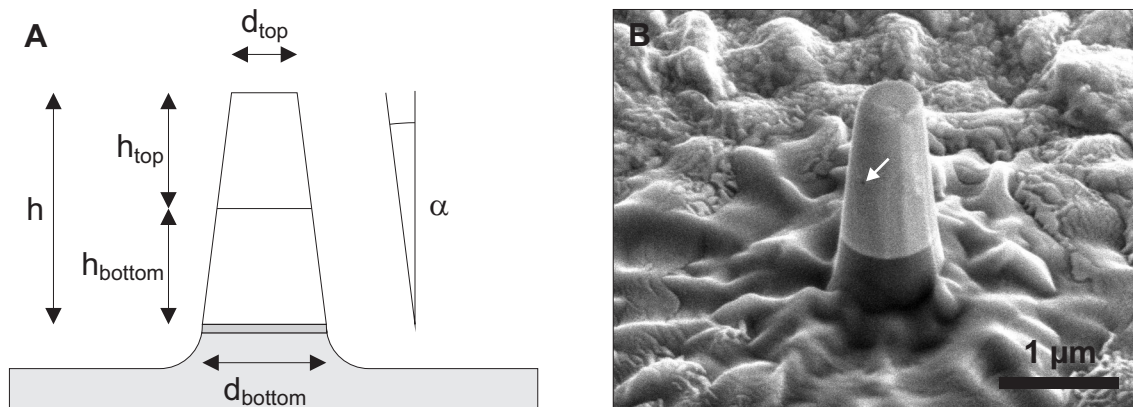


**Figure 4.1:** Geometry of the microcolumns: A - Schematic drawing of a microcolumn and its dimensions. The taper angle is exaggerated to illustrate the column geometry. B - column 6 before the test. The white arrow marks the exit opening of the nanotube.

The height of the original film was approx. 1500 nm. As the FIB milling causes some loss of material at the top of the columns, the resulting height is somewhat

smaller and varies from column to column. The overall height  $h$  was measured from SEM images, as were the respective heights of the top  $h_{\text{top}}$  and bottom layer  $h_{\text{bottom}}$ . However, as the interface between the two layers has a much weaker contrast than the Cu/Si<sub>3</sub>N<sub>4</sub>/SiO<sub>2</sub>/Si-interface at the bottom of the column,  $h_{\text{top}}$  and  $h_{\text{bottom}}$  could not be determined for all columns. Diameters given in this chapter always refer to the average diameter of the column  $\bar{d}$ , which was calculated from the diameters at the top and at the bottom of the column (i.e. at the Cu/Si-interface).

$$\bar{d} = d_{\text{top}} \cdot d_{\text{bottom}}/2$$

As described in the previous chapter, the nanotubes are hard to detect after annealing from the sample surface. Annealing flattens the raised structures due to the conformity of the coating, which indicate the position of the nanotubes. Furthermore, facetting and grain growth lead to a more rougher surface, making it even more difficult to locate the nanotubes. Therefore, sites were chosen, which seemed to contain nanotubes, but not all of them actually did as was found after milling. Then the nanotubes can be clearly seen as a dark circular spot on the side of the columns (see fig. 4.1B). It should be noted, however, that a very small nanotube might not give enough contrast and thus, as all columns were cut from the same sample, there is no definite proof that a column is free of nanotubes. In four columns, larger pores were found which are attributed to tangles of several nanotubes as was described in the last chapter (see p. 67). These large pores prohibited a controlled compression test and therefore the columns in question are not discussed in this work. Table 4.1 gives an overview of all the good columns and their dimensions.

### 4.2.2 *In situ* compression testing

In cooperation with the EMPA in Thun, columns 1-4 were tested *in situ* in an SEM (Zeiss DSM 962 with tungsten cathode). The pillars were compressed under load control to approx. 300 nm indentation depth. Unfortunately, the testing rig incorporated in the SEM did not have the force resolution necessary to measure force-deformation-curves of such small samples. The videos of these experiments show a uniform deformation of the columns even for large strains. However, the

**Table 4.1:** List of all columns evaluated

No.	$\bar{d}$ [nm]	h [ $\mu$ m]	h/d	$\alpha$ [°]	NT?	$\sigma(\epsilon)$ ?
1	630	1330	2.1	4.4	yes	no
2	640	1430	2.2	4.3	yes	no
3	660	1370	2.1	3.5	yes	no
4	680	1390	2.0	4.6	yes	no
5	750	1470	1.9	4.0	yes	yes
6	680	1450	2.1	5.5	yes	yes
7	620	1370	2.2	5.2	no	yes
8	750	1390	1.9	4.2	no	yes
9	750	1240	1.8	3.7	no	yes
10	740	1390	1.9	3.8	no	yes
11	720	1470	2.0	4.4	no	yes
12	720	1460	2.0	4.6	no	yes

resolution of this microscope was not good enough to discern any details, and the columns were therefore later analyzed in a field emission SEM (Hitachi S-4800), also at EMPA.

### 4.2.3 *Ex situ* compression testing

The rest of the samples were tested *ex situ* in a nanoindentation machine (Nano Indenter XP by MTS), equipped with a diamond flat punch (conical with opening angle of 60°, diameter of flat area 10  $\mu$ m). Due to the improved force resolution of that machine relative to the *in situ* SEM set up, it was possible to measure force-deformation curves for these samples. The samples were loaded at a rate of 0.05 mN/s to an indentation depth of 500 nm. The load was then kept constant for 10 s before unloading to allow the sample to recover completely. These experiments were done in Karlsruhe and the deformed columns sent to Thun for further SEM analysis.

#### 4.2.4 Preparation of TEM specimens and TEM analysis

After compression testing and SEM analysis, five of the nanotube containing columns were prepared for TEM. The small size makes traditional methods impossible to use and so FIB was used. At first, a rectangular slice containing column 4 was cut from the wafer using a dual beam FIB microscope (Nova 600 Nanolab by FEI). Initially, the trenches were cut at a considerable distance to the column itself, so as to induce as little change as possible in the column. That way, the dislocation structure in the deformed collar should be preserved. Of course, a column of more than 600 nm thickness (and that before deformation) is very thick for TEM studies. However, with a TEM of 1.25 MeV acceleration voltage, it should have been possible to penetrate the column without having to thin it.

Unfortunately, during the cutting, a large amount of material was redeposited on top of the column, more than doubling the column diameter, which made it too thick for the e-beam to penetrate the sample (see fig. 4.2). Therefore, the column was cut free of the redeposit, and a small amount of the column was cut away on two sides, as the first try had shown that even without the redeposition the columns are too thick to get good images.

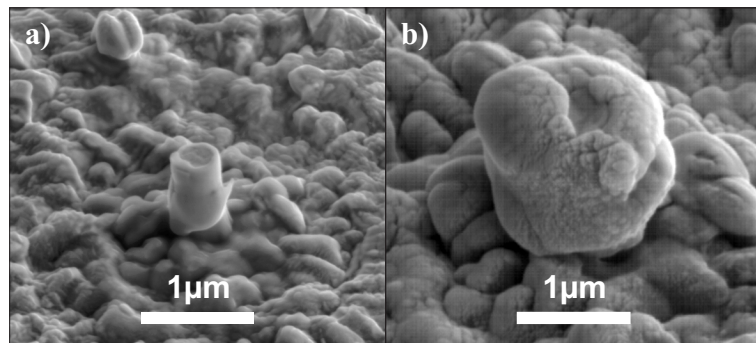


**Figure 4.2:** When trying to cut a TEM sample without milling the column itself, a lot of material was deposited on the column, more than doubling its diameter. This sample was not useable in the TEM as it was not electron transparent. a) Column before preparation of the TEM sample. b) Afterwards.

As the dual beam offers the possibility to take images without causing damage to the sample, the orientation of the nanotube in respect to the TEM sample could be controlled and was chosen at 90°. No protective layer was deposited on the column during cutting, thus the copper top layer was subjected to severe mass loss.

Unfortunately, this sample then detached from the TEM grid and was lost before it could be analyzed.

The next two samples were cut from columns 5 and 6 using a single-beam FIB (FIB 200 by FEI). Here, the routine method for cutting TEM samples was followed, thus a layer of tungsten was deposited before cutting to protect the copper surface. The orientation of the sample could not be controlled, as repeated imaging with the ion beam would have damaged the sample. Again, one sample (column 5) was lost before it could be fixed to the TEM grid, the other one survived and was successfully analyzed in the TEM.

With the next sample (column 2) a new problem led to the loss of the sample. Again, the sample was covered with a protective layer, this time of platinum, and the sample cut in the dual beam. However, the highest point of the platinum cover was not directly above the column, and therefore the column itself was completely lost in the first rough cuts. This eccentric deposition of the platinum protection layer was also observed in the last sample, column 3, but here the effect was not as marked and the sample preparation was successful.

All the TEM images were taken with the JEOL ARM (atomic resolution microscope) with an acceleration voltage of 1.25 MeV and a theoretical point resolution of 0.12 nm.

### 4.3 Results and discussion

SEM images of all the columns after deformation are shown in fig. 4.3. Even at a quick glance, it is obvious that the columns differ greatly in their deformation behavior. In the following section, it will be attempted to find correlations between the different deformation behaviors and the shape of the stress strain curves. After that, some observations on the matrix deformation mechanisms are made. The last section will then talk about the interaction of matrix and nanotubes.



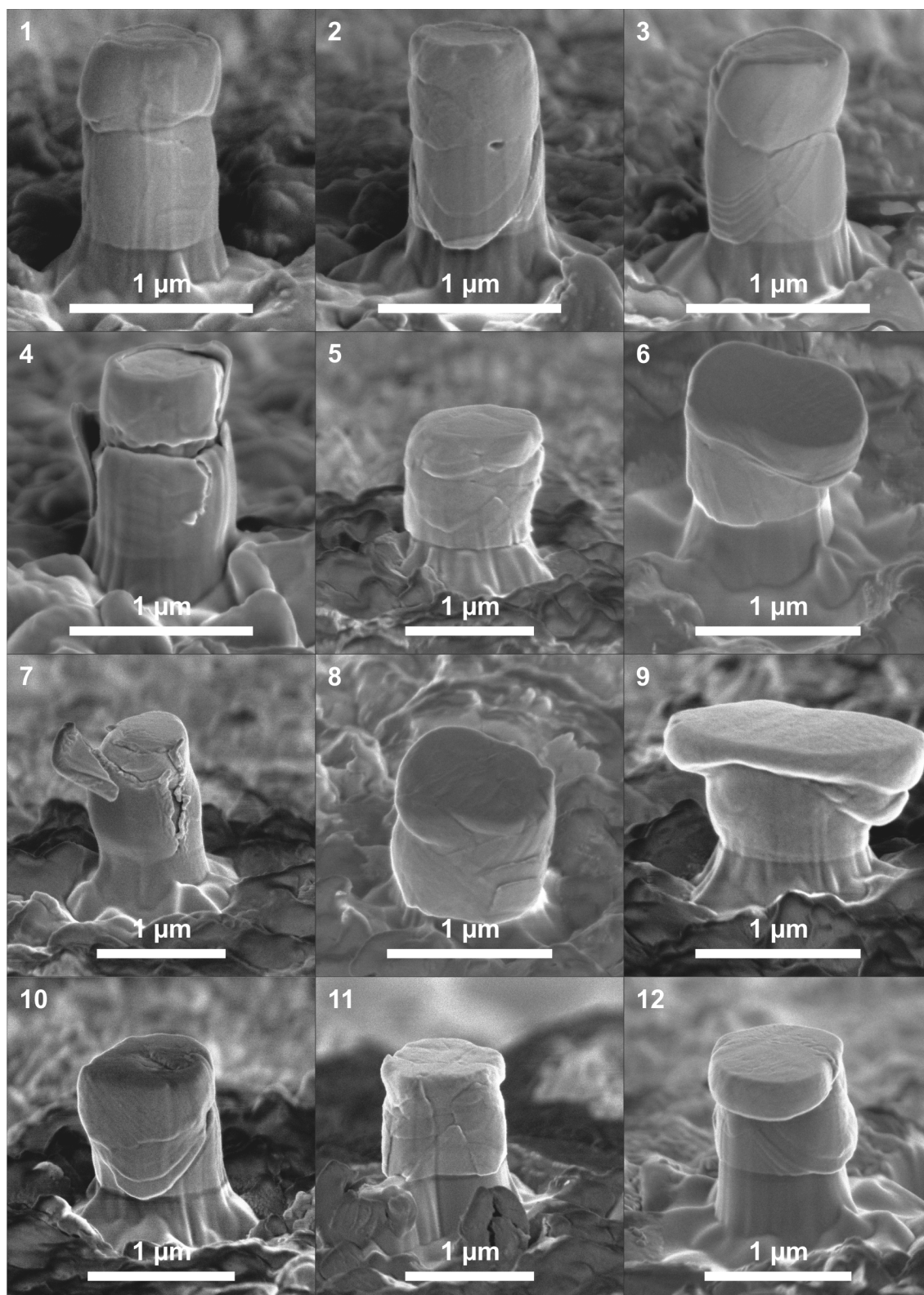


**Figure 4.3:** SEM images of all columns after deformation. Columns 1 to 6 contain nanotubes, columns 7 to 12 do not.

### 4.3.1 Stress-strain measurements

The most obvious distinction is between those columns containing nanotubes (1-6) and those which do not (7-12). The SEM images show no big difference in behavior. Except for columns 2 and 6, which clearly show the exit opening of the nanotube, there are no features, which can be found only in one group. Unfortunately, most of the columns with nanotubes were among the ones tested *in situ*, so that there are no stress-strain curves existent for them. Only columns 5 and 6 were measured *ex situ*. Fig. 4.4A gives their stress-strain-curves, 4.4B shows the curves of the columns without nanotubes (all curves true stress vs. true strain).

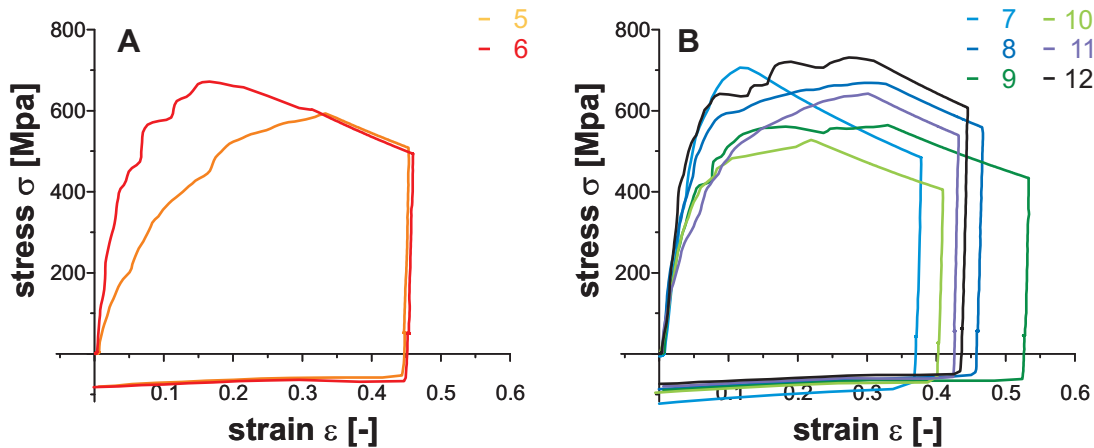


**Figure 4.4:** Comparison of the microcompression curves of pillars with visible nanotubes (A) and without (B). Note that although the pillars in B showed no visible signs of nanotubes, they may still contain smaller nanotubes.

All curves can be divided into four sections. At first there is an elastic regime. There is no sharp yield stress but rather a gradual onset of plasticity. In the case of columns 5 and 11, this onset is so early that it is hard to define an elastic region at all. But even for the other columns, the elastic slope is not well enough defined to measure the Young's modulus upon loading. This is typical for compression tests on micron-sized columns. This early plasticity is usually attributed to the roughness of the column top. As the columns never have a perfectly planar surface, some parts come into contact with the indenter before others. Thus, they experience a high initial stress and therefore plastic flow. From the SEM images taken before the test, however, there is no marked difference between columns 5 and 11 and the rest. The difference in shape must therefore be due to other reasons, as will be discussed later.

After the elastic regime, plasticity sets in. There is always a certain amount of strain hardening. For some columns, the curve is very smooth, with a continuous increase in stress. Others show several strain bursts, which may even be accompanied by a stress drop. Unlike the results which have been published for single crystalline columns, however, these strain bursts do not seem to be correlated to dislocation avalanches on one single crystal plane. There are only two columns which show such strongly developed slip bands. One is column 2, for which no stress-strain curve exists. The other is column 10, which does not show any strain bursts.

Except for these strain bursts, strain hardening continues as long as the load is increased. During the hold time, the stress decreases and there is a large strain increase. Similar effects have been noted by other authors [87] [89]. The reason for this is almost viscoelastic behavior is not clear. Finally, there is the unloading segment. Usually, the Young's modulus is measured in this segment. This was not possible for the columns presented here as they were deformed so heavily (up to 50% strain) that no uniform diameter can be assumed.

This description holds for all curves. Are there any differences between the columns with and without nanotubes? Fig. 4.4 shows no clear correlation. Most curves look very similar and the variations within one group are at least as big as between the two groups. It is therefore concluded that the presence of a nanotube has no measurable influence on the overall deformation behavior of a micron-sized column. This is not surprising considering the tiny nanotube content in the columns (for column 6 a volume fraction of 0.09% is estimated).

Are there then any other distinctions, which will explain the different shapes of the curves? The most obvious difference in the deformation behavior is the extensive deformation in the upper layers of columns 6, 9, 12 and to a lesser extend 7, when compared to the other columns. In these four samples, the upper layer has experienced a very high amount of plastic deformation, giving the column a mushroom-like appearance. The corresponding stress-strain curves are given in fig. 4.5.

The mushroom-like columns show a much more inhomogeneous strain hardening. Regimes of nearly elastic behavior alternate with large strain bursts, which some-

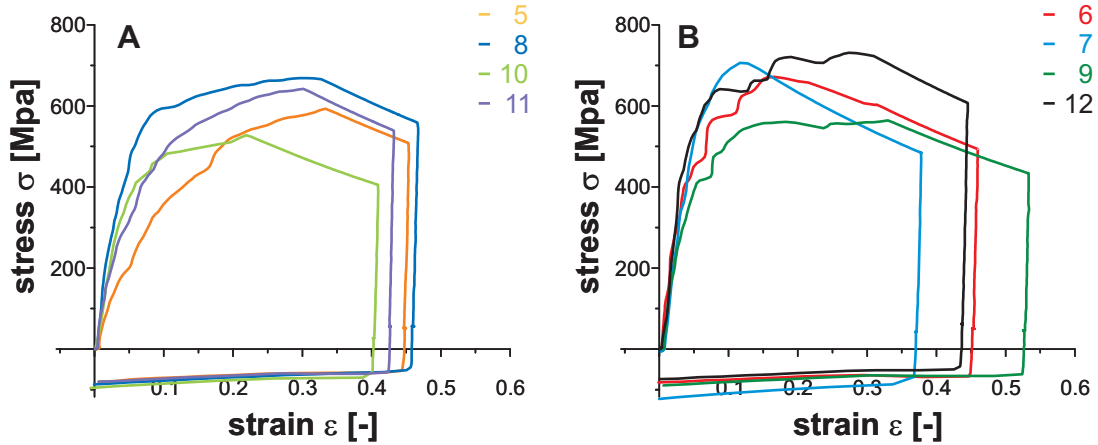


**Figure 4.5:** Comparison of the compression curves of the evenly deformed columns (A) and the mushroom-like columns (B). All the curves in the latter group, except column 7, show several alternating hardening and softening of the material.

times even show a lowering of the stress. The only exception to this is column 7, but that is the one in which the mushroom shape is very weak. The homogeneously deformed columns, on the other hand, show a much smoother stress-strain curve.

The SEM images were investigated to quantify the difference in deformation between top and bottom copper layer. To do this, the interface needs to be visible both before and after compression, which was not the case for all columns. Especially in the images taken before the test, the contrast of the interface is very weak. As it turned out, the interface could only be located, if there was a nanotube there. For column 4, the interface could be located before the test, but not afterwards. This is due to a brittle layer of carbon [87], which encloses the column (the same effect can be seen in column 7). All in all, five columns could be evaluated for the relative strain in top and bottom copper layer. The results are shown in fig. 4.6A.

All columns, except for number 2, show a much stronger strain in the top layer than in the bottom layer. Obviously, the ratio is largest for the mushroom-type column 6, but the effect is also quite strong in the columns which show a homogenous deformation. Column 2, the only one in which the bottom layer deformed more strongly, shows highly concentrated slip on a few crystal planes, which happen to be in the bottom layer. The top layer is hardly deformed at all with only 5% strain as compared to 32% in the bottom layer. Column 10 has a similar appearance in the SEM image after the test, but here the interface was not detectable, so the values could not be calculated.

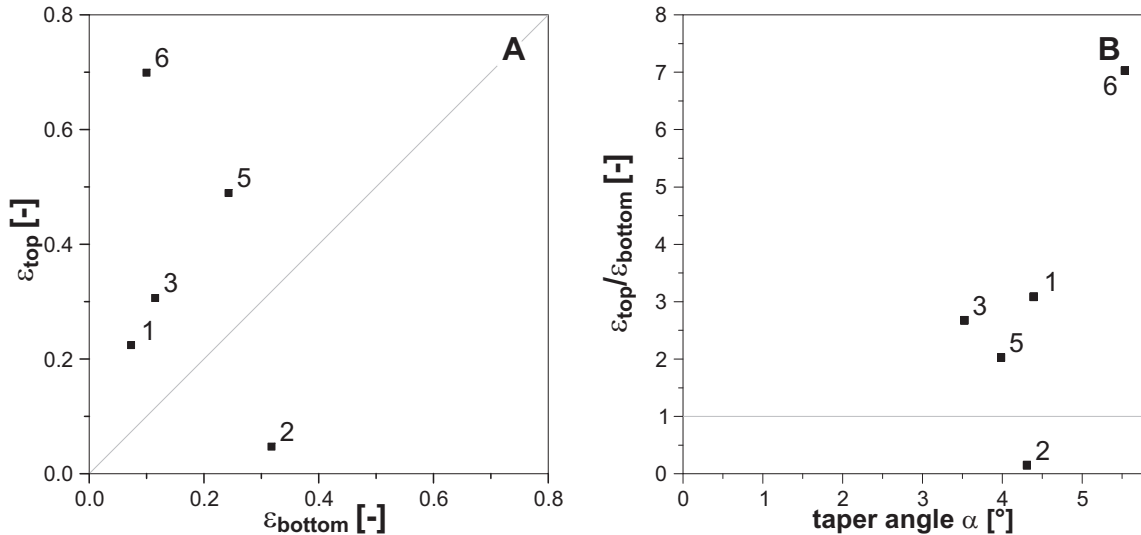


**Figure 4.6:** Differences in compressive strain in the top and bottom copper layer. A - Compressive strain in the top layer vs. compressive strain in the bottom layer. The grey line marks even deformation. B - the ratio of strain in the top layer to strain in the bottom layer plotted over the initial taper angle of the columns. Again, the grey line marks the case of even deformation of both layers.

Other authors have reported that deformation is stronger in the top half of the column [87] or that it initiates there [85]. This is often attributed to the taper of the columns, as the thinner top half sees higher stresses. However, in the work presented here, no correlation between taper and the localization of strain in the top layer can be observed (see fig. 4.6B and table 4.1 on p. 80). Although the mushroom-like columns 6, 7 and 12 are among the four with the highest taper angle, two homogeneously deformed columns (4 and 11) have taper angles nearly as high. Column 9, on the other hand, shows the strongest mushroom-shape, yet it has the second-lowest taper angle of all columns.

Another reason might be the high indentation depths. None of the columns tested *in situ* in Thun (indentation depth approx. 300 nm equivalent to 20 - 25 % strain) shows a mushroom-shape. The columns tested *ex situ* in Karlsruhe were indented to approx. 500 nm. However, only some of these columns show a mushroom-shape, not all. Furthermore, if the strain bursts alternating with regimes of higher stiffness are indeed associated with the mushroom formation, then mushrooming sets in way before the 300 nm used in Thun are reached.

As the columns used in this study are polycrystalline, the lower strength of some



of the top layers may have something to do with grain orientation and/or size. However, as there is not enough data to evaluate this (mainly because of the loss of three out of five TEM samples), this cannot be studied, and the question as to what causes the mushroom-like deformation remains unsolved. Further studies are needed here.

### 4.3.2 Matrix deformation mechanisms

TEM is an important tool to study deformation mechanisms. However, due to the small size of TEM samples, there is always a risk of producing artefacts during sample preparation. Therefore, at first a TEM sample was prepared from column 4 without milling the column itself. Yet as there was heavy redeposition of milled material onto the column, this approach had to be abandoned (see fig. 4.2). The redeposit on column 4 was milled away in the dual beam FIB and the column thinned to get better contrast in the TEM. During this process, a dark copper grain appeared at the interface between the two copper layers and in close vicinity to the nanotube. As the cutting continued, this grain showed extensive grain growth (fig. 4.2a and b). It has been observed before that copper grains oriented in a way as to show such a dark contrast will show extensive grain growth in the FIB.

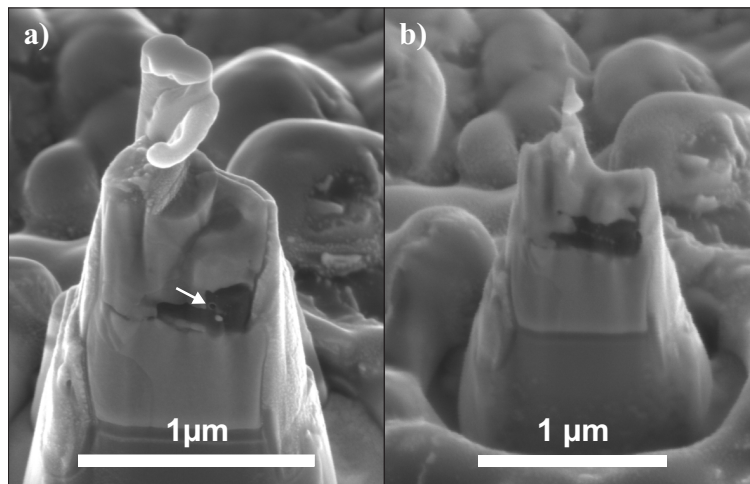


**Figure 4.7:** Grain growth during FIB milling: a) After some time, a dark grain appears near the interface. The white arrow marks the exit opening of the nanotube. b) The dark grain continues to grow as long as the milling takes place.

Grain growth alters the dislocation structure in the material as the recrystalliza-

tion front annihilates (nearly) all extrinsic defects, including dislocations. Therefore, FIB beam induced grain growth as seen in column 4 would make TEM studies pointless, at least in the affected areas. However, column 4 (which was subsequently lost, and therefore did not contribute any TEM results) was the only one, in which such grain growth was observed. No grain growth was seen in the preparation of the sample from column 3, which was also done in the dual beam FIB. The sample from column 6 was prepared in the single beam FIB, where continuous monitoring of the sample during milling is not possible. Yet all parts of this sample show a constant high dislocation density and thus it seems unlikely that extensive grain growth took place.

Even if no recrystallization takes place, FIB milling can induce changes in the position and/or mobility of individual dislocations. Yet the deformation in these columns was so strong that no individual dislocations could be discerned. Depending on the tilt angle of the TEM image, different parts of the column show the dark contrast of a strongly disturbed lattice, but there are no noticeable differences in dislocation density between the different regions. The influence of FIB damage on the overall dislocation density, however, is negligible.

The strong contrast due to the intense deformation makes it difficult to discern microstructural features like grain boundaries, slip lines or twin boundaries. Images from different tilt angles have to be used to clearly identify them. This is why the schematic drawings of columns 6 and 3, as shown in fig. 4.8 show lines that are not visible in the actual micrographs given in that image. White lines mark the outline of the pillar and the interface between the two copper layers. Green are grain boundaries, red are slip lines and blue twin boundaries.

The micrograph of column 6 shows several slip bands, mostly in the bottom layer, although there is one in the upper layer as well. Although these slip lines are straight, the material between them has the same contrast as the one outside. The regions between two adjacent slip lines show the same contrast as the rest of the grain. On the other hand, the dark regions of dislocation networks are not confined by the slip bands. In column 3, on the other hand, several twins are found, which have a contrast differing from the mother grain, due to the different crystal orientation. In fig. 4.8b, several can be seen in the right half of the column and one

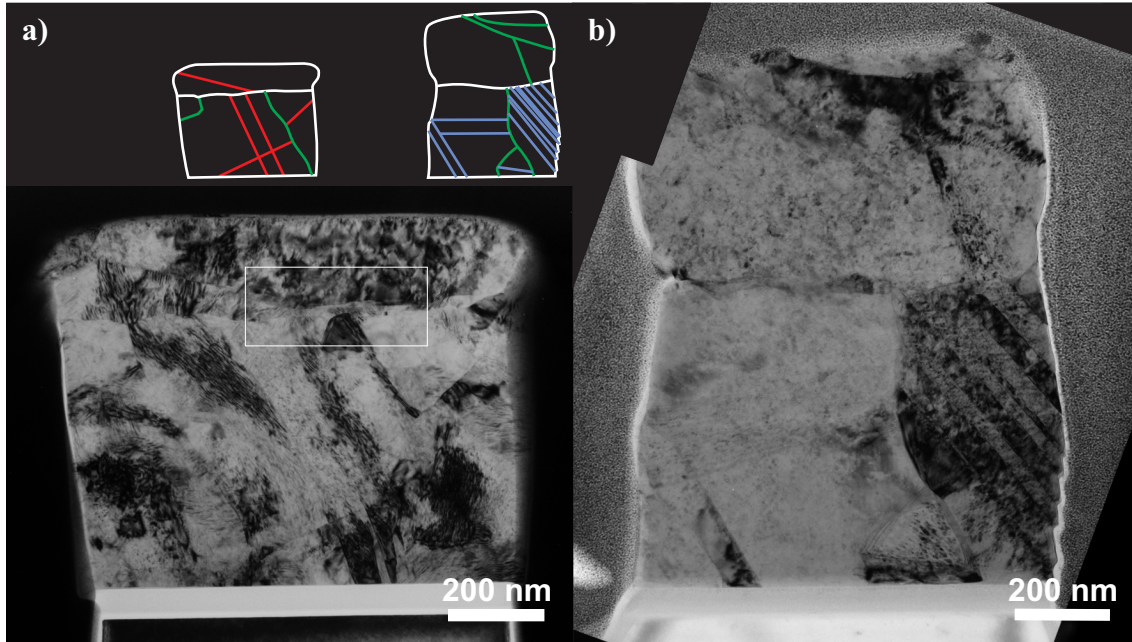


**Figure 4.8:** Overview images of the two TEM samples. The schematic drawings show the positions of column outline and interface (white), grain boundaries (green), slip bands (red) and twin boundaries (blue). a) - column 6 (tilt angle  $x = 15^\circ$ ). The white rectangle marks the section enlarged in fig. 4.11b. b) - Column 3 (tilt angle  $x = 2^\circ$ ,  $y = -20^\circ$ )

on the left side. At different tilt angles, a few more could be found in the bottom layer, but none in the top layer.

All publications on microcolumns so far report the occurrence of well defined slip systems, and a concentration of the dislocation activity on a small number of crystal planes is also often observed although it is not found in all columns. Twinning on the other hand so far has never been reported. All the columns in the publications by Uchic [85], Greer [86] and Volkert [87] were single crystalline and either Au, Ni or a nickel alloy. The columns presented here, however, are polycrystalline copper. Some of them have deformed by twinning, some by slip.

If a crystal deforms by slip, any number of dislocations can glide on any active slip plane. This is shown schematically in fig. 4.9A. If the number of dislocations on one specific plane is low, the deformation leaves little traces on the crystal surface. If the number is large, there will be a distinctive slip band with sharp edges. Twinning, on the other hand, requires the coordinated movement of many dislocations, one on each plane in the twinning section of the crystal (see fig. 4.9B). It is always associated with a large surface displacement, but although there may be noticeable



kinks, the profile of the crystal does not show the serrated edge of highly localized shear bands. Another distinction is the crystal orientation. Whereas it does not change in pure slip, in twinning the crystal lattice is mirrored on the twin plane, thus giving a different orientation contrast in e.g. TEM.

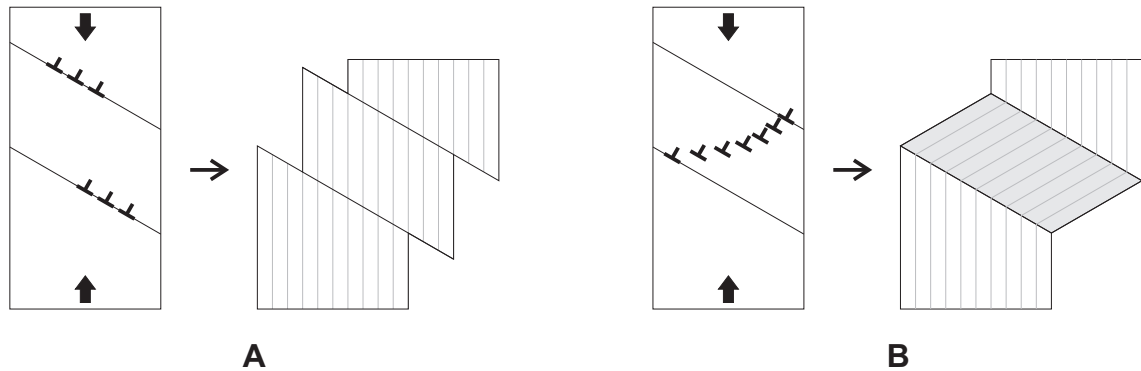


**Figure 4.9:** Schematic drawing of deformation via slip and twinning: A - In slip the orientation of the crystal stays the same. B - Twinning leads to a rotation of the lattice in the twin.

In the SEM images, the distinction between slip and twinning is less clear, as they can both result in linear traces on the sample surface. If the lines had a regular appearance and a low displacement normal to the column surface (6 and 12), they were classified as slip. If the displacement was larger, and the edges of the lines were sharp, as if the crystal had sheared off (2 and 10), it was also classified as slip. If the edges were more rounded (column 3) or if the column appeared as if a whole grain with two parallel sides had protruded from the surface (5, 8, and 11) it was classified as twin-dominated. The other columns could not be classified.

In macroscopic samples of high purity copper, twins are not observed at moderate strain rates at room temperature, although twinning can occur when the sample is shock deformed or deformed at low temperatures [90]. On the other hand, several alloying elements (e.g. Al, Zn) are known to enable twinning during quasi-static deformation at room temperature. This is usually attributed to a lowering of the stacking fault energy (SFE) through these alloying elements, as materials with a low stacking fault energy are in general more prone to twinning. Table 4.2 gives the stacking fault energies for several fcc metals and their deformation behavior in macroscopic samples.

Considering these values, it is surprising that copper microcolumns should show twinning, but gold columns with a lower SFE do not. (An unintentional alloying of

**Table 4.2:** Stacking fault energy of different materials [90]

Material	SFE [mJ/m <sup>2</sup> ]	twinning?
Ni	200	no
Cu	80	no
Au	60	no
Cu-2wt%Al	37	no
Cu-4.5wt%Al	7	yes
Cu-8wt%Al	4	yes

copper due to impurities - and thus a lowering of the SFE of the matrix material - can be excluded as the targets used in magnetron sputtering are of a very high purity and the film is deposited at HV conditions.) It is also remarkable that not all the copper columns presented in this work show twinning. The different behavior might be due to different orientations of the grains, but then the twinning plane and the preferred slip plane are the same in fcc metals (in contrast to bcc metals). If the stresses and Schmidt factors are high enough to move the dislocations necessary for twinning, they should also be able to induce slip on the same glide systems.

Grain size might be another explanation, as the grain size in column 3 seems to be slightly smaller than in column 6. On the other hand, gold columns down to diameters of 200nm have been tested and no twinning has been reported, so that explanation is not straightforward either.

Finally, the deformation behavior might be influenced by the dislocation structure of the interface between the two copper layers and also the grain boundaries within the two layers themselves. Dislocation sources, which can be activated repeatedly, are necessary for slip to be highly localized on a few planes. Twinning on the other hand requires a high density of dislocations on different planes. Two different scenarios are possible: either twinning occurs, if there is no suitable dislocation source for slip, or slip occurs, if there is no suitable dislocation network for twinning. The first one resembles the theory by Volkert et al. [87] that the size effect in single crystalline columns deforming by slip is related to the dislocation source density. However, if that was the case, one would expect the twinning columns to show a higher yield stress. As can be seen in fig. 4.10, this is not the case.

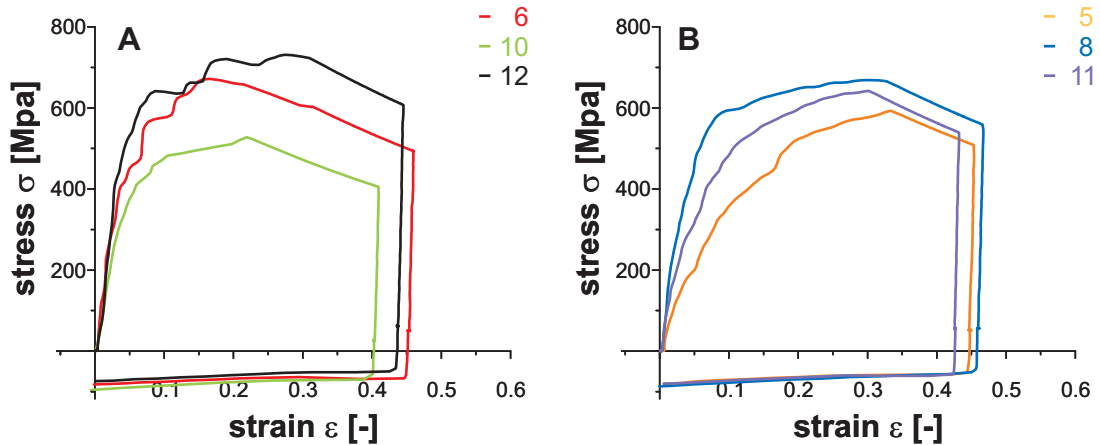


**Figure 4.10:** Comparison of the compression curves of the columns deformed via slip (A) and the columns which exhibit twinning (B). The twinning columns show an earlier onset of plasticity and a less defined yield stress.

The stress-strain curves of the twinned crystals in fig. 4.10B show a much earlier onset of plasticity, and in the case of column 5 hardly any elastic deformation at all. This early onset of plasticity is also quite remarkable in comparison with studies on macroscopic samples [91]. There, deformation twinning is usually associated with hardening as the effective grain size is reduced (Hall-Petch effect) and the rotation of the crystal lattice may lead to higher Schmidt factors for the glide systems (Basinski mechanism). However, this lattice rotation may also lead to softening, if the new orientation is more favorable to slip [92].

It should be noted that both of the columns studied in the TEM contain nanotubes at the interface. However, slip and twinning were also observed, although not in TEM samples, in columns without nanotubes and thus an influence of the nanotube on the deformation mechanisms seems highly unlikely, especially if one takes into account that the nanotubes occupy only a very small percentage of the interface.

So far, the statistics of the experiments are too low to draw any definite conclusions. Further micro-compression tests of copper columns, both polycrystalline and single crystalline, and of other polycrystalline materials besides copper are needed, and especially more TEM studies on the deformed columns.

### 4.3.3 Matrix-nanotube interactions

#### Determining the position of the nanotubes

Although the nanotube density in these columns is too low to influence the deformation behavior of the column as a whole, they still might have an impact on the matrix immediately surrounding them. Due to their small size and the low atomic number of carbon, the nanotubes embedded in the copper columns have a very weak contrast in the TEM images. However, if one has a close look at the interface - where the nanotubes must be located due to the fabrication process of the columns - one can discern areas with a slightly different appearance than the rest of the sample. They are mostly lighter than the rest, but they might also be rather dark if they are surrounded by a dark copper grain. One such area from column 6 is shown in fig. 4.11a with white arrows to mark its boundaries.

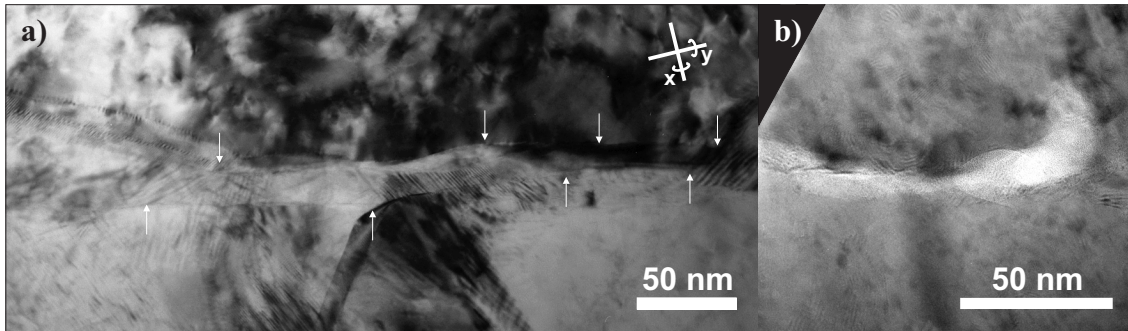


**Figure 4.11:** High resolution TEM images of the areas at the interface with a slightly different contrast, identified as carbon nanotubes. a) Close-up of the central part of column 6 (see fig. 4.8a; tilt angle  $x = 15^\circ$ ). b) Close-up of the bright spot near the center of column 3 (tilt angle  $x = 21^\circ$ ).

By tilting the sample both in  $x$ - and  $y$ -direction, it was found that the object responsible for this contrast is roughly cylindrical in shape, with the long axis lying parallel to the interface between the two copper layers and also parallel to the plane of the TEM lamella. For column 3, the contrast at the interface was very weak, except for one region a little to the right of the middle (shown in 4.11b). By tilting, this region was found to be also cylindrical in shape and parallel to the interface, but in contrast to column 6 it is oriented at an angle to the plane of the TEM lamella. To be sure that these cylindrical objects in the two samples are indeed carbon nanotubes, the TEM images had to be related to the position of the nanotubes as

it is known from SEM and FIB images.

For column 3, this was rather easy, as this sample was done in the dual beam FIB and several images were taken during milling. The positions of the nanotubes, as they were seen on these images, were superimposed on a TEM image (see fig. 4.12). In this figure, the yellow marks come from a plane of the sample that was removed during milling and thus marks a position somewhat "above" the TEM lamella. Orange are the positions as they were found on the top surface of the lamella and brown are the positions from the bottom surface.

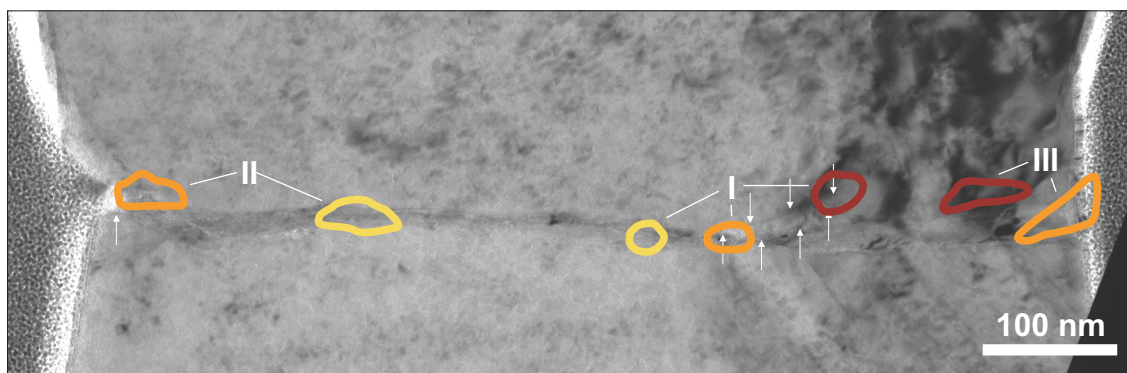


**Figure 4.12:** Position of the nanotubes as identified on images taken during FIB milling. Yellow marks lie above the sample surface, orange ones are on the top surface of the lamella and brown ones on the bottom. The white arrows mark the area shown in fig. 4.11b.

With this it becomes clear that the cylindrical object in the middle (marked by arrows) is indeed a nanotube. It goes all the way through the lamella, lying at an angle of approx.  $30^\circ$  to the plane of the lamella, as it was not possible to get this nanotube head-on even at a tilt angle of  $46^\circ$ . In addition, two more nanotubes should be present in the sample, but they are very close to the edge and may not extend all the way through the lamella, which explains, why they could not be identified in the TEM sample. Nanotube II enters the TEM lamella very close to the side of the column and actually exits through the side of the column, instead of through the bottom surface of the lamella. Finally, nanotube III probably goes all the way through the TEM lamella, but as it enters the lamella very close to the edge of the column, this is not 100% sure.

The shape and position of the contrasting region in column 6 also suggest that this object is indeed a carbon nanotube. However, as this TEM sample was made in a single beam FIB, there are no images from the milling itself. The orientation of

the TEM lamella therefore needs to be correlated to the SEM images, where the exit openings of the nanotube are visible (see fig. 4.16b). For this, the distance between the two strongest slip bands is used. As the calculations are rather lengthy, they are presented in an appendix at the end of this chapter, so as not to interrupt the discussion (see pp. 102). From the calculations, it is safe to say that the nanotube runs nearly diagonally through the lamella. However, it is not possible to say whether it exits through the side of the column or through the lamella surface very close to the edge of the column. Therefore, it seems safe to assume that the object in fig. 4.11a is a carbon nanotube.

### Formation of funnel-like depressions

Before compression testing, the nanotubes are discernible as a black circular spot on the side of the columns, but they do not appear to influence the topography of the column flank (see fig. 4.13a). After the test, however, the contrast around the nanotube is much stronger (see figs. 4.13b and c). Now, in addition to the dark contrast of the nanotube itself, there is a white line nearly circling the nanotube. This line is probably due to a topography contrast and indicates that the immediate vicinity of the nanotube has retracted from the rest of the column surface, leaving a funnel-like depression. These depressions are not circular any more, but oval in shape, thus indicating a radial compression of the nanotubes.

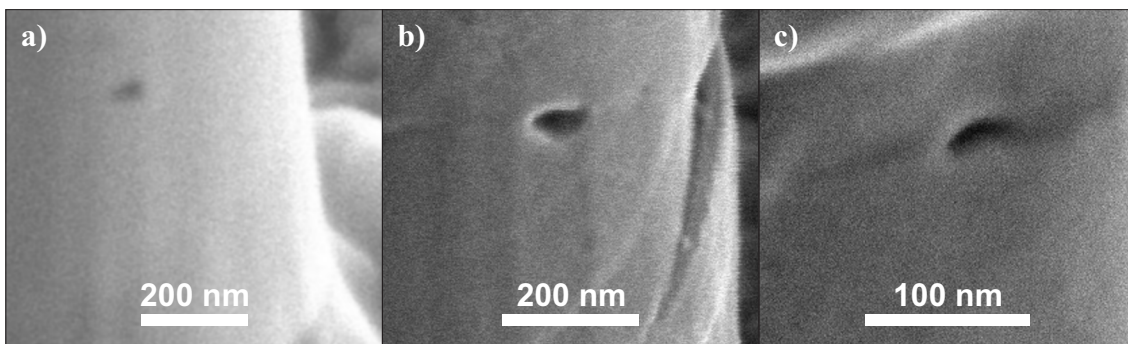


**Figure 4.13:** Change in appearance of the nanotube during compression. a) Column 5 before deformation: the nanotube is cut in one plane with the copper. The side of the pillar is perfectly straight. b) Column 2 after deformation: in addition to the dark contrast of the nanotube itself, the bright edge-contrast of the funnel-like opening is clearly visible. c) the same effect as seen on column 6.



The TEM images of column 3 confirm these results. As has been shown, in this column there are two nanotubes which exit the column flank within the TEM lamella or very close to it (nanotubes II and III in fig. 4.12). When tilting the sample in the TEM, such funnel-like depression were found on both exit sites. As they only appear at a certain tilt angle, they are indeed of limited width (rather than a groove which runs all the way around the column). The one near nanotube II (see fig. 4.14a) is approx. 30 nm deep and close to 60 nm in diameter. The one near nanotube III is approx. 50 nm deep and almost 100 nm wide. On the other hand, the height of the compressed nanotubes is only approx. 26 nm and 37 nm respectively, as measured from the dual beam images used for fig. 4.12. Thus, the depressions in the column surface are roughly twice the diameter of the nanotube itself.

This is a clear indication for a sizeable shear strength. As the column deforms and increases in diameter, the much stiffer nanotube cannot follow this expansion. Due to the shear forces at the interface, the copper adhering to the nanotube is also retained, resulting in the funnel-shaped depression. If there was no force transfer through the interface, the nanotube would simply slip out of its sheath and the metal would deform as if no nanotube was present.

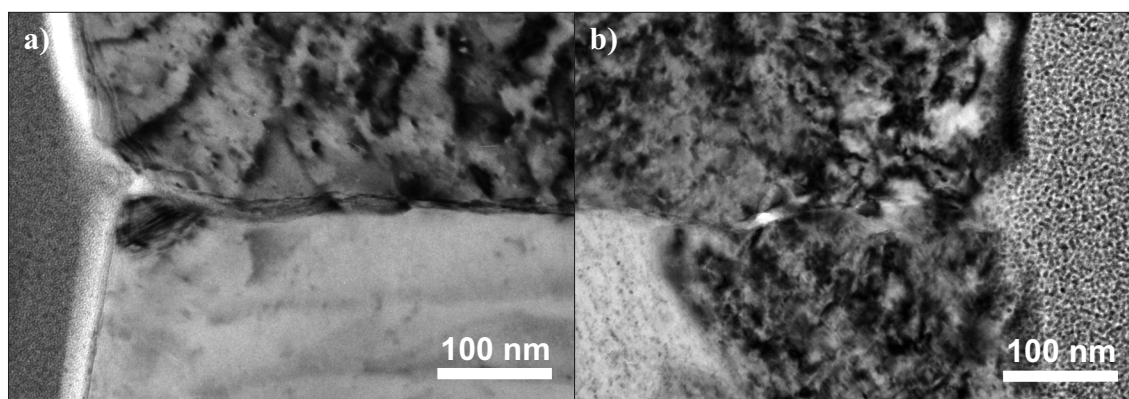


**Figure 4.14:** TEM images of the funnel-like depression in column 3. a) Depression on the left flank of the column near nanotube II (tilt angle  $\alpha = 0^\circ$ ). b) Depression on the right flank near nanotube III (tilt angle  $\alpha = 28^\circ$ ).

In the TEM images of column 6 a similar depression can be seen on the right side, although the contrast is weaker than in the images of column 3. The lamella of column 6 was much thicker than that of column 3, which would explain the

weaker contrast. On the other hand, it is also possible that part of the depression was milled away during the TEM sample preparation as it is not possible to say to 100% accuracy whether the nanotube leaves the lamella through the column flank or through the lamella surface.

### A possible case of fiber fracture

For column 6, there is no single image in which the nanotube can be traced over the whole column width, due to the weak contrast. Yet when looking at images taken at different tilt angles, the nanotube becomes visible in different areas of the sample. Five such areas are outlined in fig. 4.15.

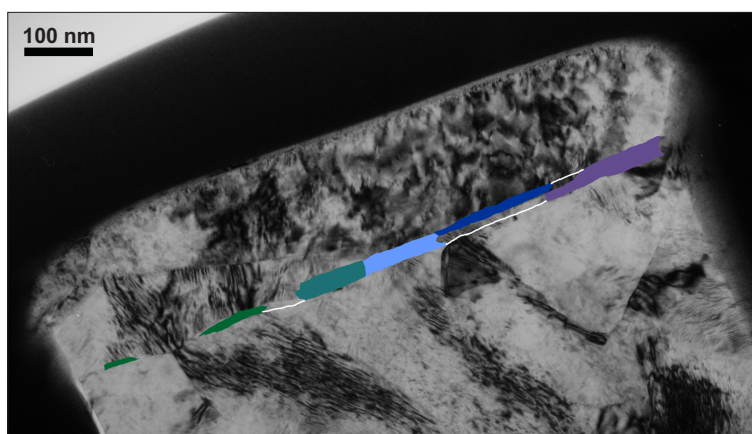


**Figure 4.15:** In this image, the areas have been marked, which have been identified as parts of the nanotube. Although each image shows only a small part, the parts fit together nicely. The image might show a case of fiber fracture due to transverse elongation (tilt angles  $\alpha = -2^\circ$  to  $21^\circ$ ).

Taking all these images together, it appears that the nanotube is continuous at least in the right half of the column. In the left half, only two smaller areas were found. The length of the two small areas is 50 nm and 110 nm respectively, whereas the length of all the other areas taken together is 580 nm. This contrasts with an column diameter at the interface of 690 nm before deformation, and 940 nm afterwards. The diameter of the nanotube before the test was 58 nm as measured from SEM images. In the TEM images, the diameter was calculated to be approx. 30 nm on the right side and approx. 10 nm in the two smaller areas on the left side. This is in agreement with a radial compression of the nanotube, which can also be seen in fig. 4.13c.



Unfortunately, it was not possible, to get any carbon signal from the sample with EDX-measurements in the TEM. There is therefore no definite proof that the areas marked in figs. 4.11 and 4.15 really are carbon nanotubes. However, they are roughly cylindrical in shape (as was tested by tilting the sample both in x- and y-direction), they show only a very weak contrast (as is expected for a thin carbon object in a copper matrix) and they are located exactly where they are expected from the analysis of the SEM and FIB images. It can therefore be safely assumed that these regions are really carbon nanotubes.

Under the further assumption that no part of the nanotube was missed in fig. 4.15, one can try to understand what happened in column 6 during deformation. As the nanotube has been cut on a level with the column flank, its length before compression must have been approximately the column diameter of 690 nm (assuming that it runs straight through the center of the column). After deformation, the column diameter is 940 nm, which corresponds to a strain of 36%. If there is no debonding and slipping at the nanotube-matrix interface - and the funnel-like depression at the right column flank seems to indicate that - the nanotube would have to undergo the same strain. However, experimental results published so far [22] have suggested that the maximum breaking strain for multi-walled carbon nanotubes is around 5% (see table 2.2 on p. 40).

Formation of the funnel-like depressions eases the strain on the nanotube, but even if there were depressions of 50 nm depth on each side (which is the maximum found in column 3), the strain would still exceed 20%. There are therefore three possibilities: either the interface fails, the matrix close to the interface fails or the nanotube breaks. The length of the continuous area on the right side of fig. 4.15 is 580 nm, thus smaller than the original column diameter. Adding the two smaller areas on the left, one arrives at a number of 749 nm, which exceeds the original column diameter. Yet in the literature it has been reported repeatedly [24] [22] that MWNTs tend to fail by a sword-in sheath mechanism (see p. 39), in which the inner tubes are pulled out of the outer ones, so that the length of the fractured pieces combined is longer than the original length. This would also explain why the two areas on the left show a smaller diameter. If they contain fewer carbon walls, they would compress more readily. Fracture close to the left side of the column would

also explain, why no funnel-shaped depression was found on that side.

Without definite proof that there is actually carbon at these areas - either through analytical TEM or through images which show the atomic structure of the nanotubes, this explanation must remain a hypothesis. Yet it is in good agreement with everything that is known today about carbon nanotubes and thus seems a plausible explanation for all the facts. Furthermore, fiber fracture in compressions tests due to transverse elongation of the matrix has been reported before for macroscopic composites [93][94].

## 4.4 Summary and outlook

Micron-sizes columns were fabricated from a model composite, in which nitrogen-doped MWNTs are incorporated between two layers of magnetron-sputtered copper. Six of the columns contained nanotubes, six did not. The presence of nanotubes showed no influence on the stress-strain-curves of the entire column. This fact was attributed to the small volume fraction of nanotubes in these columns. Nearly all columns showed a stronger deformation in the top copper layer than in the bottom layer. No correlation to the initial taper angle of the column was found. Samples with a strong localization of plasticity in the top level (mushroom-type columns) showed strain bursts alternating with nearly elastic regimes in the stress strain curves, whereas the curves were very smooth for the other columns.

Although some columns deformed by dislocation slip, as has been reported in the literature, there were also some columns which showed extensive deformation twinning. Up to date, no twinning has been reported for micron-sized columns, and twinning is also not typical for macroscopic copper samples of high purity. Columns with twinning showed a very early onset of plasticity and a less defined yield stress. The maximum stresses reached were comparable to the slip-deformed columns. This is remarkable as twinning in macroscopic samples is usually associated with increased strain hardening. Why some columns deform by slip and others by twinning could not be ascertained, as the statistics were too low.

It proved difficult to locate the nanotubes in the TEM micrographs, due to the weak contrast of a small carbon object embedded in a metallic matrix. Therefore,

additional information from SEM and FIB images was used. With that it was possible to locate the nanotubes with sufficient certainty. In all tested pillars, in which the nanotube was visible after compression, a funnel-shaped depression was found to have formed around the nanotube. This was also observed in the TEM images, where the diameter of this funnel was measured to be roughly twice the diameter of the nanotube. These depressions indicate a sizeable interfacial strength, as the nanotube was able to retain the matrix in its immediate vicinity. In one of the TEM samples, there were also indications for fiber fracture caused by the transverse elongation of the column.

Testing carbon nanotube reinforced polycrystalline copper films in a microcolumn compression test provided several interesting results, notably the presence of deformation twinning and strong indications for a sizeable shear strength at the nanotube-metal interface. Further studies are needed to gain a better understanding for the ultimate causes of the observed behavior. Loading the columns to lower strains could provide samples with a clearer microstructure. Determining the orientation of the grains within the columns might prove crucial for the question of whether a column deforms via slip or via twinning. Finally, more TEM samples are needed to get more data on the interaction of nanotubes and metals.

## Acknowledgements

This work was done in cooperation with Dr. Ruth Schwaiger of the Forschungszentrum Karlsruhe, who cut the columns and conducted the *ex situ* microcompression experiments and with D. Johann Michler of the EMPA in Thun, Switzerland, who did the after-test SEM imaging and conducted the *in situ* compression tests.

## Appendix: Orientation of the column 6-TEM sample

To locate the nanotube in the TEM images, the plane of the TEM lamella has to be correlated to the SEM images, which show the exit openings of the nanotube. Once the angle  $\alpha$  between the image plane of the TEM image and the SEM image is known, the orientation of the nanotube within the TEM lamella is defined.

Three images were used for the following calculation. One TEM image taking at a tilt angle in x-direction of  $3^\circ$  (fig. 4.16a, one very similar to the first one, but taken at a tilt angle of  $18^\circ$  (not shown) and an SEM image (fig. 4.16b).

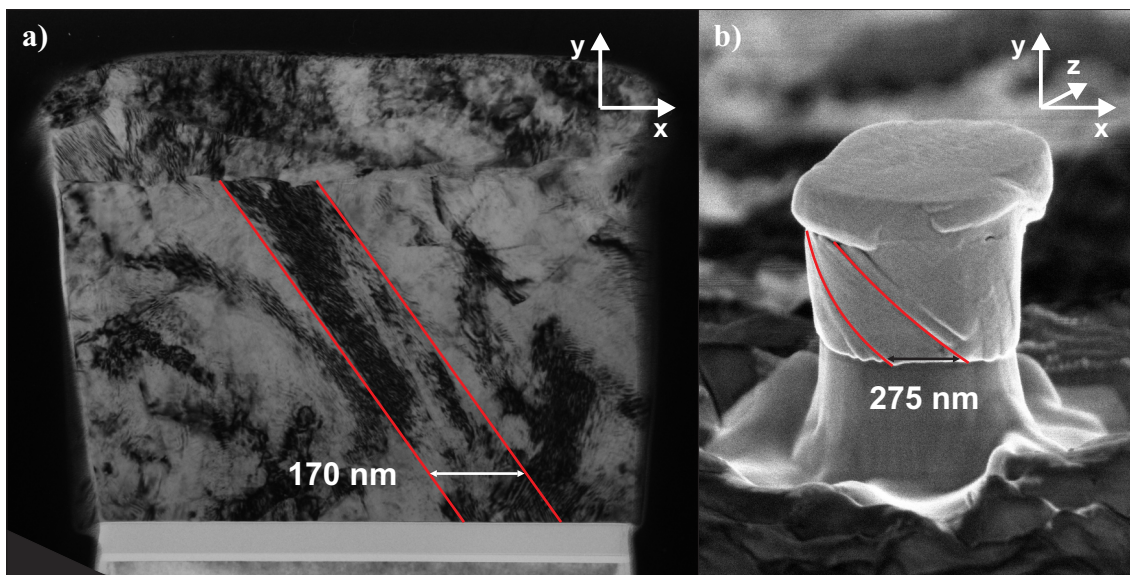


**Figure 4.16:** Determining the orientation of the TEM sample of column 6 in relation to the SEM images. a) One of the two TEM images used for the calculation, showing the slip planes 170 nm apart (tilt angle  $x = 3^\circ$ ). b) In the SEM image, the same two slip lines are 275 nm apart.

All three images show the same pair of slip traces. Fig. 4.17a gives a schematic representation of the deformed column as seen from the top, the position of the slip traces (red) and the three images. As can be seen, the distance between the slip traces depends on the angle of the image in respect to the column. From these different distances and from the known value of the angle  $\alpha^* = 18^\circ - 3^\circ = 5^\circ$  between the two TEM images, the angle between the TEM lamella and the SEM image can be calculated. Fig. 4.17b gives all the variables used in the following

calculations.  $x' = 170$  nm and  $x'' = 118$  nm are the distances as measured in the two TEM images.  $x = 275$  is the corresponding value from the SEM images. Variables with \* refer to the triangle between the two TEM images, variables without \* refer to the triangle between TEM image one and the SEM image.

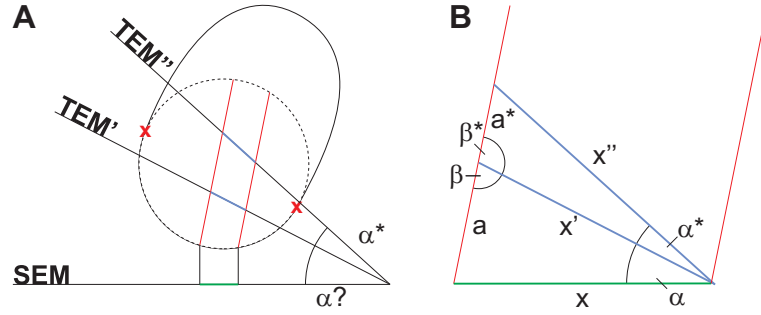


**Figure 4.17:** Schematic drawing of the orientation of the images used for the orientation calculation for column 6 (A) and the variables needed (B). The red x marks the exit openings of the nanotube.

Using the law of cosine,  $a^*$  can be calculated.

$$a^{*2} = x'^2 + x''^2 - 2x'x'' \cos \alpha^*$$

$$a^* = 63.805 \text{ nm}$$

From this,  $\beta^*$  can be calculated with the law of sine.

$$\frac{x''}{\sin \beta^*} = \frac{a^*}{\sin \alpha^*}$$

$$\beta^* = 28.598^\circ$$

$$\beta = 180^\circ - \beta^* = 151.402^\circ$$

Again using the law of cosine, a quadratic expression for  $a$  can be found.

$$x^2 = a^2 + x'^2 - 2ax' \cos \beta$$

$$a_{1,2} = x' \cos \beta \pm \sqrt{x'^2 (\cos^2 \beta - 1) + x^2}$$

$$a_1 = 113.425 \text{ nm}$$

$$a_2 = -411.945 \text{ nm}$$

Finally, the law of sine gives  $\alpha$ .

$$\frac{a}{\sin \alpha} = \frac{x}{\sin \beta}$$

$$\begin{aligned}\sin \alpha_1 &= 0.197 & \sin \alpha_2 &= -0.717 \\ \alpha_1 &= 11.387^\circ & \alpha_2 &= -45.809^\circ\end{aligned}$$

If  $\alpha_2$  was the correct solution, a large overhang on one side of the TEM sample would be expected. As this is not the case,  $\alpha_1$  must be the correct solution and the angle  $\alpha$  between the SEM image and TEM image one is approx.  $11.4^\circ$ . As the TEM image was itself taken at an angle of  $3^\circ$ , the rotation of the TEM lamella with respect to the SEM image plane is  $8.4^\circ$ . In addition, the width of the column in the lamella is very close to the width of the column in the SEM image, therefore, the center of the lamella is close to the center of the column and the position is approximately as shown in fig. 4.18 (the thickness of the lamella is approx. 300 nm). It is not possible to give the position of the nanotube within the TEM sample (e.g. if it exits through the side of the column or through the lamella surface) to 100% accuracy, but it can be safely assumed that the nanotube runs through the lamella in a roughly diagonal way.

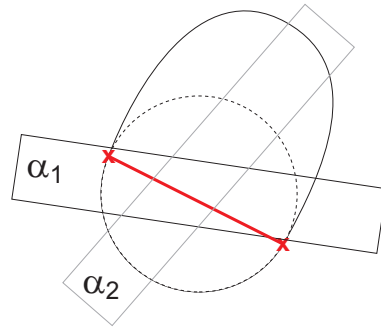


**Figure 4.18:** Orientation of the TEM lamella of column 6 as calculated from the images. The red line shows the probable position of the carbon nanotube. As the TEM images show no overhang on one side of the sample  $\alpha_1$  must be the correct solution.

## Chapter 5

# Preferential deposition and interfacial strength in electrolytically produced Cu/CNT composites

### 5.1 Introduction

Carbon nanotubes show a range of interesting properties, both mechanically and electronically. But for many applications it is necessary to form a good contact with another material, in many cases a metal (e.g. as electric contact). However, studies have shown that only metal melts with a surface tension of less than  $\sim 180 \text{ mJ/m}^2$  wet carbon nanotubes. Most commercially interesting metals, like e.g. copper (surface tension of  $1430 \text{ mJ/m}^2$  [38]) or aluminum, have not been tested for their ability to wet carbon nanotubes, but as their melts do not wet graphite, it is usually assumed that they do not wet CNTs either. Therefore, it should be difficult to coat CNTs with these metals in the melt. However, it has been proven that nanotubes can be coated with metals using electrochemical processes [73][79]. In the work presented here, the early stages of electrodeposition were studied. Additionally, nanotube carpets of a medium to high density were coated. Some observations on the adhesion between nanotubes and metal are presented, as well as a longer term outlook for this research.

## 5.2 Experimental procedure

Three different types of samples were investigated for this study. The first used nitrogen-doped carbon nanotubes ( $CN_x$ ), which were removed from the substrate on which they were synthesized, before they were used in the electrodeposition. These samples therefore show a random orientation of the nanotubes. A silicon wafer coated with a thin layer of copper was used as a substrate for these samples. For the other samples, carpets of pure-carbon MWNTs were studied. In one, the nanotubes were very well aligned. This sample was grown on an electrically non-conductive substrate. In the other, they formed a thick tangled film, grown on an electrically conductive substrate.

### 5.2.1 Isolated $CN_x$ on copper

The nitrogen-doped nanotubes used in this study were CVD-grown from a benzyl amine/ferrocene aerosol following a process similar to the one used by Mayne et al. [11]. The resulting tubes show the typical bamboo-like structure. Their diameter ranges from 10 to  $\sim 100$  nm, their length from 50 to 150  $\mu\text{m}$ . A more detailed description of the nanotube synthesis can be found on pp. 60.

As substrate, pieces ( $\sim 50 \text{ mm}^2$ ) of a silicon wafer were used, which had been coated with a thin ( $\sim 300 \text{ nm}$ ) copper film via magnetron sputtering to make it electrically conducting. To remove any native copper oxide, the wafers were rinsed subsequently in ethanol, water, sulfuric acid and again water. This was repeated three times. Afterwards, the substrate was immediately immersed in the electrolytic bath. The electrolyte consisted of a solution of  $\text{Cu}_2\text{SO}_4$  and  $\text{KNaC}_4\text{H}_4\text{O}_6$  in water, with a pyrophosphate buffer to keep the pH-value between 8.2 and 8.5.

For most samples, the nanotubes were dispersed directly in the electrolyte. The resulting nanotube densities were very low, even if the dispersion was allowed to settle overnight onto the substrate before deposition. Increasing the amount of nanotubes in the electrolytic bath did not increase the number of nanotubes incorporated in the film. This is probably due to agglomerates of carbon nanotubes, which form if a certain threshold concentration in the bath is reached. As these agglomerates remain in the solution, the number of nanotubes deposited remains



small [73] [77]. For the sample shown in fig. 5.2 d a different approach was taken. Here, a small amount of  $CN_x$ -powder was rubbed directly onto the wafer with a spatula, which resulted in very high, inhomogeneous three-dimensional nanotube distribution.

Copper was deposited for varying times  $t_d$  at a current of  $I_d = 5$  mA. After that, the electrolysis was stopped, the samples rinsed and characterized in a field emission SEM (Zeiss LEO 1530 VP), using an in-lens secondary electron detector.

### 5.2.2 Aligned CNT-carpets on non-conductive substrate

For the second type of samples, aligned carpets of multi-walled carbon nanotubes were used, which had been synthesized by a micro-wave assisted CVD-process, resulting in a carpet with a lower nanotube density than usual for aligned carpets. These nanotubes were not intentionally doped with nitrogen, although a certain contamination or a damage to the outer walls due to interactions with the plasma cannot be ruled out completely. In these carpets, the nanotubes were well aligned but of differing lengths. They formed large pointed bundles of several hundred nanotubes. Fig. 5.1 shows the substrate with the as grown nanotubes before the electrodeposition.

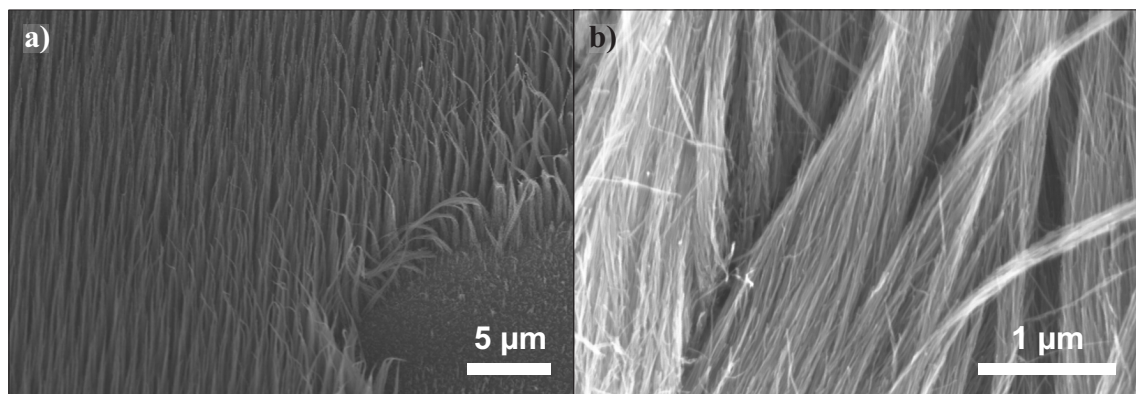


**Figure 5.1:** Sample with highly oriented CNTs before the electrodeposition: a) At the edge of a spot, where the CNTs were scraped off, the bundles of CNTs are clearly distinguishable. b) Close-up of the CNT-bundles. The nanotubes vary in length, but are very similar in diameter.

The CNTs were grown on a non-conductive substrate. Thus, for the electrodeposition, the silicon substrates were attached to a piece of tin-foil with silver paint,

taking care that the silver paint covered a small stripe of the substrate surface on all four sides of the sample. This ensured that at least some nanotubes were electrically connected to the power supply. As MWNTs are electrically conductive and each tube is in contact with its neighbors, the whole film should thus be connected. The conditions for the electrolysis were the same as for the  $CN_x$ -samples, with deposition times of 60s and 120s respectively. These samples were also characterized in the SEM. In addition, several cross-section through the copper-nanotube deposit were cut with a focused ion beam microscope (FIB) to better examine the degree of filling of the carpet with copper.

### 5.2.3 Tangled CNT-carpets on conductive substrate

The last type of samples consisted of a dense, tangled carpet of carbon nanotubes grown on a conductive substrate [95]. As some of them have a very wavy shape (see fig. 5.6), they seem to be rich in defects, although they were not doped with nitrogen.

For the electrodeposition, the same parameters were used as for the aligned carpets. As the tangled carpets were grown on a conductive substrate, no silver paint was applied to the top of the film or the edges. Two samples were used, both were studied in the SEM and then reimmersed in the electrolytical bath for further deposition cycles. The deposition time  $t_d$  given for these samples is therefore always the cumulative time of the deposition cycles of this sample up to this point.

## 5.3 Results

### 5.3.1 Isolated $CN_x$ on copper

Typical images of the  $CN_x$ -samples are shown in fig. 5.2. If the electrolysis was run for only a short time, small copper crystals form exclusively on the nanotubes. No copper deposits on the underlying copper film. The copper grains on the nanotubes coalesce to form a continuous coating, which thickens with time. Finally, the substrate is covered by a continuous copper film with thickly coated nanotubes protruding from the film surface. Some nanotubes, however, show no copper deposition

at all, as can be seen in the last image. Such uncovered nanotubes were found in all samples, yet always in small numbers.

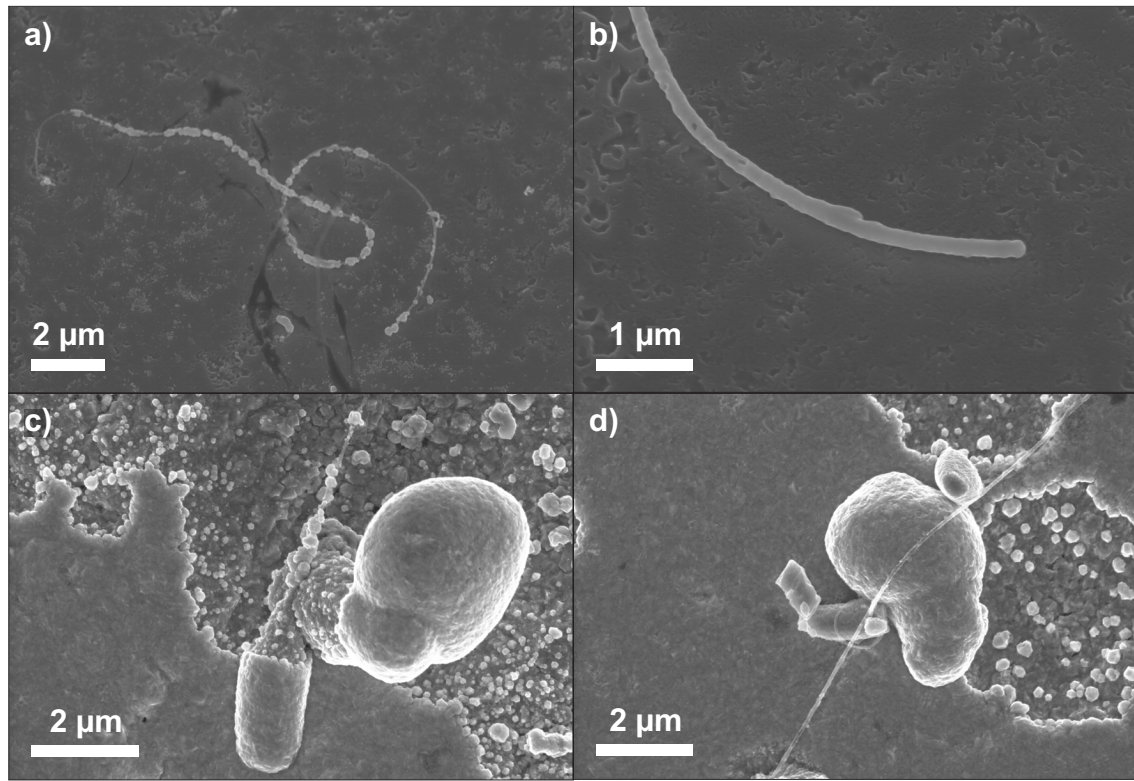


**Figure 5.2:** Deposition of copper on carbon nanotubes during electrolysis. a) Copper grains form preferentially on carbon nanotubes. ( $t_d = 60$  s) b) At a different site of the same sample, the nanotube is already completely enclosed. ( $t_d = 60$  s) c) The copper coating around the nanotube thickens, until a dense film is formed. ( $t_d = 10$  min) d) Only a few nanotubes remain uncoated ( $t_d = 60$  s).

### 5.3.2 Aligned CNT-carpets on non-conductive substrate

Fig. 5.3 shows the samples with the aligned CNTs after electrodeposition of copper. Interestingly, metal deposits everywhere on the sample, not just in the areas immediately next to the silver paint. In fact, the deposition rate near the silver paint appears to be slightly smaller than in the center of the sample, as can be seen in fig. 5.3c.

In the sample with 60 s deposition time, the bundles are still clearly visible, as shown in fig. 5.3a and b. The tips are often connected, thus forming tripod-like shapes as in the work by Tang et al. [79]. More copper deposited on the bundle

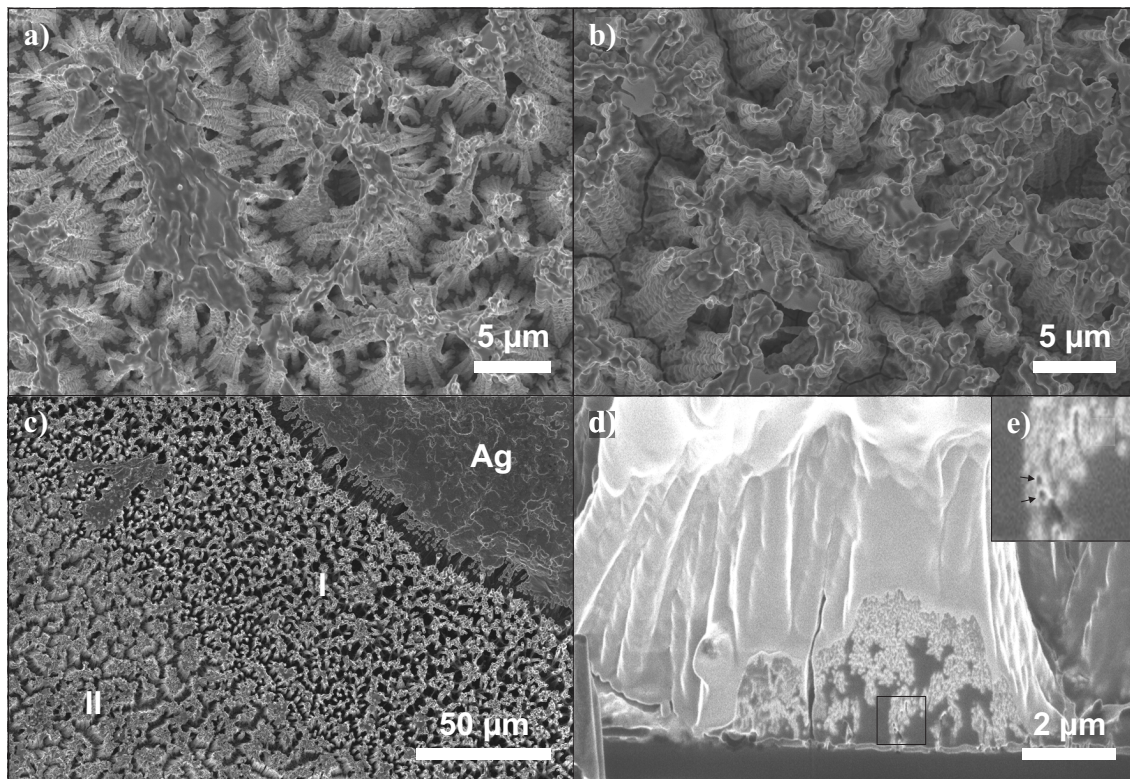


**Figure 5.3:** Samples with aligned CNTs after electrodeposition: a) After a short deposition time ( $t_d = 60$  s) the bundles are coated with copper. In some places, a continuous film starts to form on top of the nanotubes. b) With longer deposition times ( $t_d = 120$  s) the copper deposits thicken to form solid blocks. c) Overview image from the edge of the sample. Close to the area covered with silver paint (marked by Ag) is a zone (I) in which the deposition rate is markedly reduced when compared to the rest of the sample (II). d) FIB image of a cross-section of one such block ( $t_d = 120$  s). The nanotubes form well-aligned bundles separated by areas of pure copper. Except for very few pores (black arrows), the nanotube bundles appear to be well coated with copper.



tips than at the CNT/substrate interface. In some places, the tips start to grow together to form a continuous film, with large cavities underneath (see fig. 5.3a). No copper seems to deposit on the substrate itself.

In the sample with 120 s deposition time, the copper coating on the bundle thickens and bundles become joined in larger blocks (fig. 5.3b). The FIB cross-section (fig. 5.3d) shows that these blocks consist of areas, where the nanotubes are densely packed, joined by areas of pure metal. The space between the nanotubes of a single bundle appears to be completely filled with copper, except for a few small pores (indicated by the black arrows).

In both samples, many places could be found in which the copper was cracked. Such cracks are marked by the white arrows in fig. 5.4a. The source of the internal stresses that induces the cracks is not quite clear. They could be related to the stirring of the bath or non-uniform stress generation during deposition due to variations in the structure. On both sides of these cracks, nanotubes which have been pulled out of the matrix can be found. Others bridge the gap and are still embedded in the matrix on both ends (see fig. 5.4b-e).

Additionally, a small area of the sample with  $t_d = 60$  s was deformed by nanoindentation. The curves from the nanoindentation, although recorded, were not evaluated in detail, as the sole purpose of the indentation was to induce further cracking and plasticity in the sample. They showed the high compliance of a foam-like material.

A closer look at the deformed area shows a heavily disturbed microstructure (fig. 5.5a). The bundles have been twisted, and in many places nanotubes are sticking out of the surface. Some of the nanotubes show a very thin silhouette with perfectly straight sides. Two such tubes are indicated by the white arrows, a close-up of one of these is shown in fig. 5.5b. Other nanotubes are thicker, with variations of the thickness even over a very short distance. In several instances, a spherical thickening right at the end of a tube is observed (marked with black arrows, close-up in fig. 5.5c) These NTs appear to be coated with copper. Most nanotubes, however, cannot be easily classified as either the one or the other.

Upon close inspection of the indented area, several places can be found, where

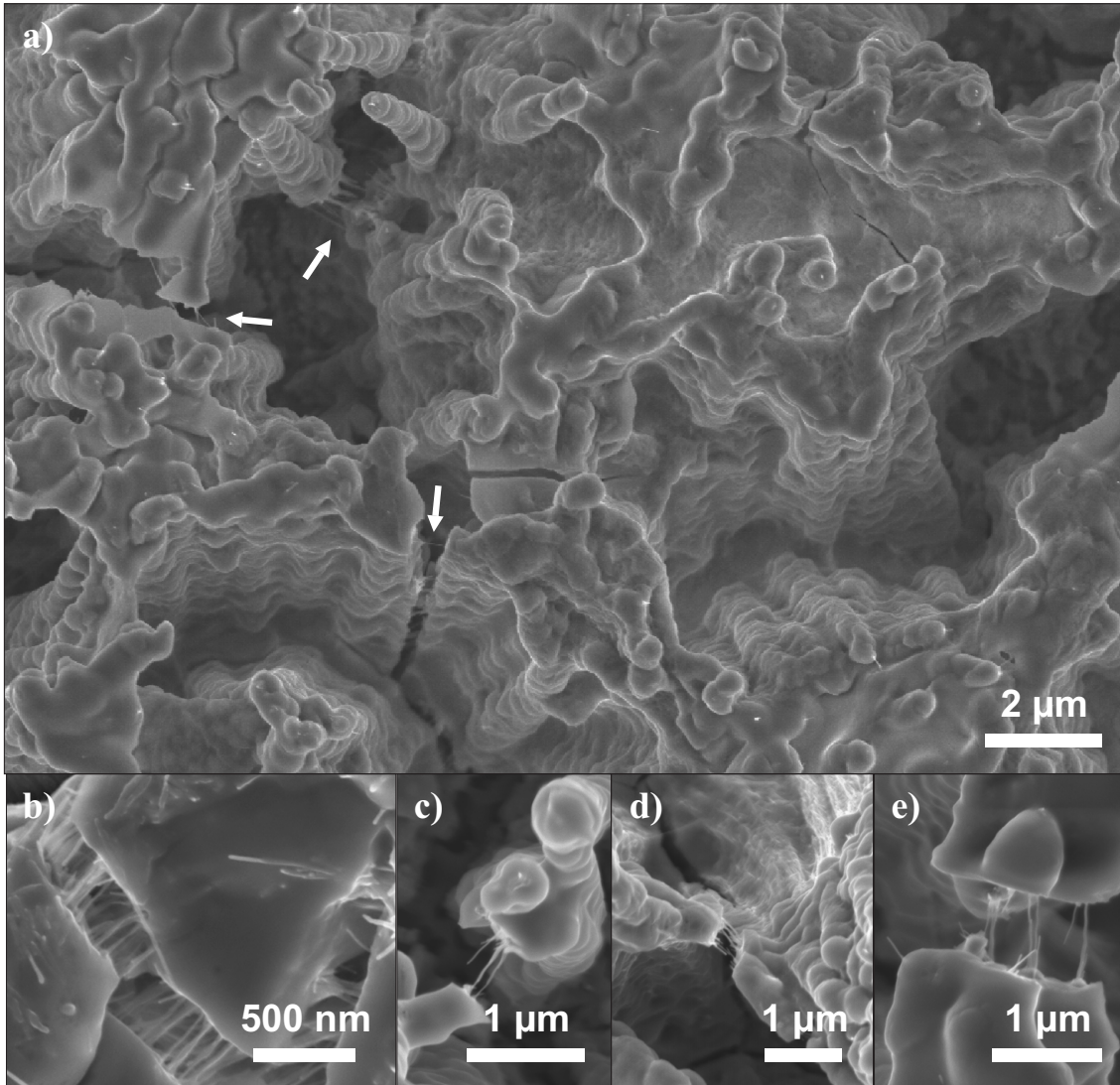


**Figure 5.4:** Nanotubes at cracks formed during electrodeposition: a) The white arrows indicate cracks, which are bridged by CNTs ( $t_d = 120$  s). b) and e) Close-up images of cracks. Short nanotubes, which have been completely pulled out of the matrix on one end, can be found on both sides, while other nanotubes still bridge the gap.

the copper was deformed to form a point around the base of a nanotube, resulting in an outline reminiscent of several connected crescents. Several such points are indicated by the arrows in figs. 5.5d.

### 5.3.3 Tangled CNT-carpets on conductive substrate

At very short deposition times, copper starts to coat the topmost nanotubes (see fig. 5.6). With growing deposition times, the nanotubes below become coated as well, until a dense film forms, with a few thickly coated nanotubes still raised above

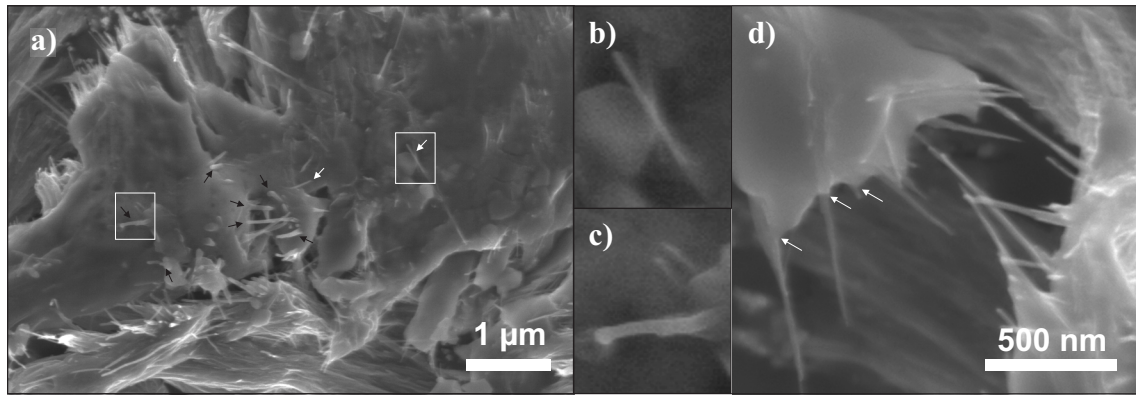


**Figure 5.5:** Nanotubes at deformed regions: a) Image from an area deformed by nanoindentation. Some nanotubes (white arrows) appear to be free of copper, while others (black arrows) appear to be coated. b) and c) closeup of an uncoated and a coated nanotube (marked in a) with white rectangles) d) In some places, copper deformed around the base of the nanotubes, resulting in an outline reminiscent of several connected crescents.

the surface. However, at any time the deposition is very inhomogeneous across the sample with places still completely free of copper while others in close vicinity are already completely covered. There is no discernible pattern as to which areas become coated.

Similar to the samples with aligned carpets, cracks started to form in the growing film after a certain density had been reached. One such crack is shown in fig. 5.6e. Although it is not quite possible to see all the way down to the substrate, the copper seems to enclose the nanotubes in a dense film to a considerable depth. The formation of the crack caused many nanotubes to be broken. Some of them exhibit a certain, if limited amount of pull-out, while others broke exactly in the plane of the crack. A prominent example of the latter can be seen in the center of the image, where two nearly parallel tubes can be located on both sides of the crack.

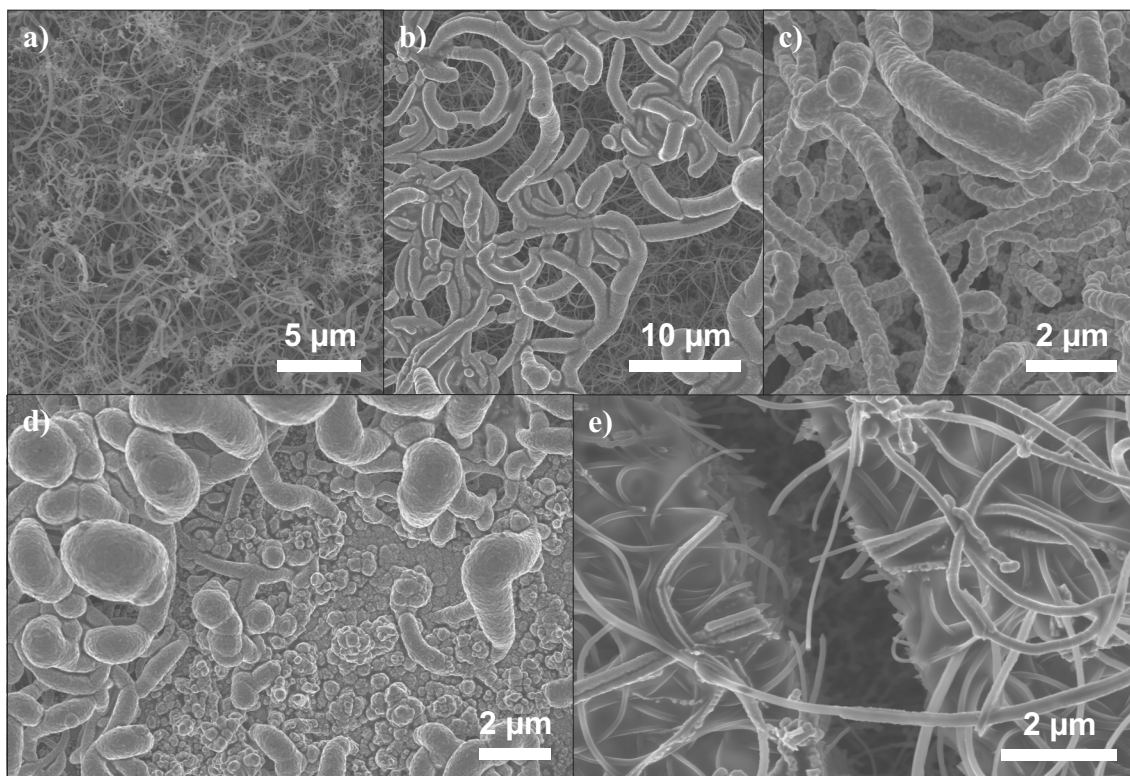


**Figure 5.6:** Samples with tangled CNT-carpets: a) Nanotube carpet before electrodeposition. b) At first, only the nanotubes at the top are coated ( $t_d = 40$  s). c) A little later, the nanotubes below are coated as well ( $t_d = 63$  s). d) Finally, a dense film is formed. ( $t_d = 220$  s). e) Cracks form due to internal stresses, showing breaking of nanotubes and limited pull-out. ( $t_d = 40$  s).



## 5.4 Discussion

### 5.4.1 Samples with isolated $CN_x$

The preferential deposition of copper on carbon nanotubes instead of the copper substrate can probably be attributed to geometric effects of the electric field. As the nanotubes are raised above the substrate, the electric field density is higher around them. This is especially pronounced for nanotubes sticking up straight, thus forming a very sharp tip, similar to an antenna. The rate of electrodeposition is proportional to the field density, thus accounting for the coating of the nanotube. As MWNTs are usually very good electric conductors, it is sufficient that the nanotube is connected electrically at one point along its length. The few nanotubes, which are not being coated, are then probably either electrically isolated from the substrate, or contain large defects (e.g. breaks), which disrupt the conductive path.

Along a single nanotube, the copper deposition was initiated in many places at the same time, thus quickly forming a continuous film on the nanotube. This is different from the results reported by Arai et al. [78], who found a "skewered-dumpling"-morphology of few large nickel grains growing at defect sites on the nanotube. This difference might be explained by the much higher density of defects in the nitrogen-doped nanotubes used in the first part of this study. The coating of the nanotubes, thus achieved is very uniform. To use such regular structures in technical applications, it is necessary to understand, which factors promote the formation of a uniform coating in preference to a "skewered-dumpling"-morphology. Further research is needed here.

### 5.4.2 Samples with CNT-carpets

Although the defect-rich  $CN_x$ -tubes might be favorable to the formation of uniform coatings, it is also possible to coat pure-carbon nanotubes as was demonstrated in section 5.3.2. As the influence of synthesis conditions on the crystallinity of carbon nanotubes is still not known and as no TEM analysis was carried out on these samples so far, the defect density of these tubes is not known. However, it should be markedly lower than in the nitrogen-doped nanotubes.

The aligned carpets soon form a continuous coating, which thickened to larger blocks, upon increasing of the deposition time. As the FIB images show large areas which are free of nanotubes the present samples are not suited to fabricate composite films. However, as few pores have been found in these samples, it should be possible to use substrates with higher densities of nanotubes to begin with, thus reducing the amount of unreinforced copper.

The tangled carpets prove that it is possible to form dense copper films with high nanotube densities. This is quite remarkable as the coating here is concentrated at the top of the carpet at first. Yet the images of the cracked regions (see fig. 5.6e) show that the dense copper coating reaches into considerable depths, although it is not possible to say, if the copper really reached the substrate, as no FIB cross sections were made.

However, in these films, the deposition rate was very non-uniform across the sample. More research is needed to understand the mechanisms. So far, the results suggest that the substrate does not play a major role in determining the deposition behavior of the films. One might reason that a conductive substrate would lead to the copper film growing from the bottom of the carpet to the top, as the electricity flows through the substrate. For the nonconductive substrate, the path of electricity would go across the top of the nanotube carpet, as this is where the tubes touch. If anything, the results showed the opposite to be the case, although that might also be attributed to the different morphology of the nanotube carpet.

In the area of the aligned sample that was deformed by nanoindentation, many nanotubes were found which were coated by a thin layer of copper. As such nanotubes are absent in the undeformed area, these nanotubes were probably pulled from the matrix. For the copper to stay attached to the nanotube, the interfacial strength must therefore have been higher than the shear strength of copper. Such strong adhesion at the interface of copper and nanotubes is also supported by the images from the cracks.

In the aligned sample, short nanotubes can be found, sticking out of both sides of the crack, next to longer ones, which are still bridging. This is prove that the adhesion was strong enough to cause nanotubes to break, for if these tubes had

just been shorter to begin with, they would be found only on one side of the crack, considering the morphology of the carpet (see fig. 5.1b).

In the case of the tangled samples, the evidence for strong adhesion is even more evident. Here, several nanotubes can be located on both sides of the crack, showing little or no pull-out, which is equivalent to a large stress transfer across the interface and therefore very good adhesion.

## 5.5 Summary and outlook

Composite samples of carbon nanotube carpets and electrodeposited copper have been prepared. These samples show signs of a sizeable interfacial strength, like broken tubes due to stress transfer from the matrix to the fiber and nanotubes, which have been pulled out of the bulk of the matrix, but which are still covered with copper. Similar images have been published for nanotube-polymer composites [96][97], but this is the first time that such indications for adhesion between carbon nanotubes and a metal matrix have been reported. On the contrary, it is often assumed that the interfacial strength between nanotubes and any metal matrix is weak or even negligible, due to the near-perfect surface of carbon nanotubes (unless there is a formation of carbides). As a strong interfacial adhesion is crucial for using the extraordinary mechanical properties of carbon nanotubes successfully in composite materials, it is of high interest to further investigate the bonding between carbon nanotubes and metals.

Using aligned carpets, a uniform coating with copper was achieved. The nanotube bundles were well penetrated by the copper, showing hardly any porosity at all. However, the space between the bundles was filled with unreinforced copper, lowering the effective nanotube density of the composite. Higher densities were achieved with the tangled carpets, but here the deposition rate was inhomogeneous across the sample, leaving some areas virtually free of copper, when others had already formed a compact film several microns thick. Further research is needed to find a process which insures a high nanotube density and a homogeneous deposition behavior.

Using nitrogen-doped carbon nanotubes, the initial stages of electrodeposition on

nanotubes have been studied. It was found that the copper is deposited preferentially on the nanotubes instead of on the substrate. This is attributed to geometrical effects. As the deposition is initiated in many sites along a single nanotube, a continuous coating is formed very early in the process, leading to very uniform structures. With longer deposition times, the deposits around the nanotubes thicken until a continuous film is achieved.

Electrodeposition is a very promising route for the synthesis of carbon-nanotube reinforced metal matrix composites. For most metals, electrolytical deposition methods are already in use. As was shown, by using such methods, it is possible to make composite materials with a high density of aligned nanotubes, and with a good adhesion between nanotubes and matrix. This is possible both for defect-rich nitrogen-doped nanotubes, as well as for the more perfect and thus stronger pure-carbon nanotubes. As one of the biggest problems in carbon nanotube-reinforced composites so far was to reach a high and uniform density, this might prove to be of high interest, e.g. for wear-resistant coatings [74].

## Acknowledgements

The aligned CNT-carpets were supplied by Dr. Siegfried Menzel of the Leibniz Institute for Solid State and Materials Research in Dresden.

The tangled CNT-carpets were supplied by Prof. Carl Thompson and his coworker Gilbert Nessim, both at the Massachusetts Institute of Technology.

## Chapter 6

# Electrolytically deposited Cu-CN<sub>x</sub> composites: tensile testing and characterization

As described in the previous chapter, during electrodeposition copper forms preferentially on top of nitrogen-doped carbon nanotubes. Electrodeposition is therefore an interesting method to produce composite samples. Like all methods in which a film is grown on a substrate electrodeposition is not suited to the fabrication of true bulk samples. However, as it is a very fast process when compared to sputtering, very thick films can be grown. These can then be removed from the sample and tested as a freestanding film, thus forming a kind of semi-bulk sample. In such samples, the behavior of the composite film can be studied without having to account for the influence of the substrate.

### 6.1 Experimental procedure

To make the best use of the extraordinary mechanical properties, a high density of nanotubes would be desirable. However, if the density is too high, and especially, if there are large, three-dimensional tangles, pores may form. The density therefore has to be kept low enough to ensure the formation of a dense composite.

### 6.1.1 Sample preparation

Tin foil (thickness 0.127 mm, purity 99.9%) was chosen as substrate, as it is electrically conducting and can be selectively etched without removing the copper. The first criterium is important for the electrodeposition, the second to get the freestanding copper film needed for tensile testing.

First the tin foil was cut into rectangles with a size of 10mm x 50mm and weighed. One side of the foil was coated with a commercially available varnish to keep it free of copper deposition. Then the sample was mounted on a plastic holder, so that the uncovered side of the substrate was exposed. This side was then cleaned with acetone and etched slightly using NaOH to remove any surface oxide, before the substrate was immersed in the electrolyte, whose composition is given in table 6.1. The electrolyte was adjusted to a pH of 8.2 - 8.5 and a temperature between 36°C and 38°C. The voltage was adjusted so that the electrical current was between 50 mA and 52 mA, resulting in a current density of approx. 100 A/m<sup>2</sup>.

**Table 6.1:** Chemical composition of electrolyte

Substance	Weight
Cu <sub>2</sub> SO <sub>4</sub> · 5H <sub>2</sub> O	7 g
K <sub>4</sub> P <sub>2</sub> O <sub>7</sub>	30 g
Na <sub>2</sub> HPO <sub>4</sub>	19 g
KNaC <sub>4</sub> H <sub>4</sub> O <sub>6</sub> · 4H <sub>2</sub> O	5.75 g
H <sub>2</sub> O <i>dem.</i>	200 ml

To achieve a good adhesion of the copper film on the substrate, first a pure copper layer was deposited (deposition time  $t_d = 5$  min). The sample was then removed from the electrolytical bath, cleaned with water, and wrapped in a piece of lint-free tissue (Whatman 105 Lens Cleaning Tissue) that had been saturated with a CN<sub>x</sub>-containing paste. This paste was prepared by boiling a dispersion of nanotubes in the electrolyte for some time, until a viscous paste was achieved.

The paste was prepared in several batches with differing water content (although the nanotube content in the original solution was kept the same). When applying the paste to the paper, care was therefore taken to always achieve the same shade

of color to keep the nanotube concentration in the paper on one level. However, as this was done purely manually, there was some variation due to the experimenter.





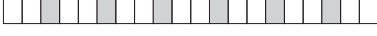










The wrapped sample was re-immersed in the electrolyte and deposition continued. To achieve a more homogeneous distribution of nanotubes within the film and to prevent the tissue from getting imbedded in the copper, the deposition was interrupted every 5 min to clean the sample, rewrap the tissue, and apply more nanotubes. After a couple of such cycles, copper starts to form on the tissue itself, and it has to be replaced. The final cycle was done like the first one without paper and nanotubes to minimize the porosity in the surface.

The nanotube content within the samples was varied by alternating reinforced layers with pure copper layers and changing the total number of layers. However, as it was not possible to control the exact amount of nanotubes incorporated during electrodeposition, these variations can only give a broad trend. In addition, three control samples were fabricated which did not contain any nanotubes at all. A schematic representation of the number and sequence of the layers is given in table 6.2. Each box represents 5 min deposition time. Filled boxes are done with the sample being wrapped in the nanotube-saturated paper. For the empty boxes, the samples was not wrapped in paper and therefore also not in contact with nanotubes. If the incorporation of nanotubes during each cycle had been the same, the samples would be arranged in order of increasing nanotube content. In addition, the table gives the mass difference  $\Delta m$  before and after deposition, the average thickness  $h$ , and width  $b$  of the sample at the gage length as measured from SEM images.

After the deposition, the samples were rinsed in water and ethanol and dried in an air stream. Then the varnish on the backside was removed using acetone. Afterwards, the samples were weighed again to estimate the layer thickness from the mass increase. The samples were then cut into the final dogbone shape (see fig. 6.1A) and the tin substrate was removed using HCl to give a freestanding copper film.

On some substrates, an approximately 150 nm thick copper layer was deposited before electrodeposition through a physical vapor deposition (PVD) method. Adhesion on these substrates was very weak, and most of the films did not survive the

**Table 6.2:** Overview of all tensile samples fabricated by electrodeposition

	$\Delta m$ [g]	layer sequence	h [ $\mu\text{m}$ ]	b [mm]
1	0.1145		21.2	4.506
2*	0.1274		18.3	4.999
3	0.1220		21.2	4.847
4	0.1037		25.7	4.755
5	0.0999		17.1	4.572
6	0.1037		15.6	4.817
7	0.0986		17.3	4.748
8	0.1054		17.6	4.933
9	0.0794		16.3	4.969
10	0.0968		17.3	4.961
11	0.1073		21.1	5.016
12	0.1085		18.1	4.806
13	0.1117		20.8	4.766
14	0.0814		18.1	4.822
15	0.1101		21.2	4.769

\* Film grown on substrate with PVD-deposited copper layer (150 nm)

first cleaning step during electrodeposition. Only on one sample a film could be grown. Adhesion was still very weak and after deposition the copper film detached from the substrate by itself. This sample was therefore not etched with HCl and appears in table 6.2 as number 2.

### 6.1.2 Tensile testing and microscopical analysis

The freestanding copper films of approximately 20  $\mu\text{m}$  thickness are mechanically stable enough for handling, but are prone to bending. To ensure that the films remained straight when fixed in the tensile testing stage, they were first transferred to a holder, made from three brass plates held together by adhesive tape. A schematic drawing of this holder and how it works is given in fig. 6.1B-D. This holder together with the sample is fixed in the grips of the testing machine. Since the machine itself



keeps the sample straight, once enough tension is applied, the adhesive tape on the holder can be cut and one of the three plates removed. The remaining two plates stay in place, but as they are not connected anymore, they have no influence on the tensile test. Using such a holder makes it possible to conduct a tensile test on the film itself without any stress concentrations through bending or twisting of the sample.

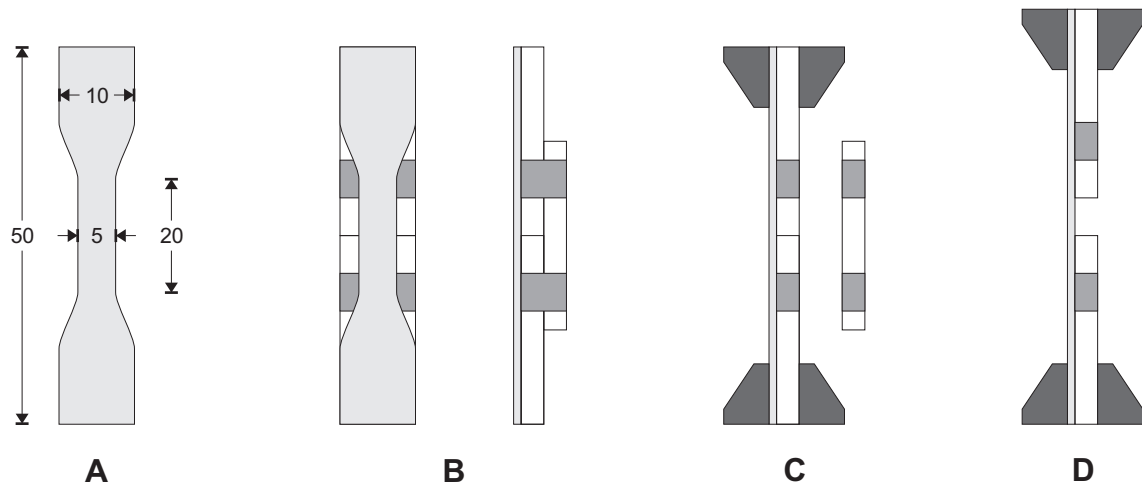


**Figure 6.1:** Samples for tensile testing: A - sample dimensions in mm. B - sample fixed on the holder. The holder is made up of three identical brass plates, held together with adhesive tape. C - once the sample is held firmly by the testing rig, the adhesive tape is cut and the center plate removed. D - the holder carries no load during tensile testing.

The testing rig used was a Zwicki 1120 by Zwick with a load cell suitable for forces up to 2 kN (error  $<0.1\%$ ). The speed was set to 0.003 mm/s for forces between 0 mN and 6 mN and 0.005 mm/s for the rest of the test. These two different speeds were used to correlate the data with the external strain measurement from the laser extensometer. The results showed that the laser extensometer was in very good agreement with the internal strain measurement of the testing rig. Therefore, the internal strain measurement was used. All samples were strained to failure.

After failure the samples were studied in a field-emission SEM (LEO 1530 VP by Zeiss) using an in-lens secondary electron detector. Both surfaces (i.e. the original surface from the electrodeposition, as well as the side where the tin was removed) were studied, as well as the fracture surface. In addition, the sample was cut with a knife at some distance from the fracture site to measure the original thickness as well as the width of the sample (see table 6.2).

## 6.2 Results

### 6.2.1 Sample appearance

Most samples showed a shiny copper surface directly after electrodeposition, but some already showed a brownish, matte surface similar to heavily oxidized copper. After the etching step, all samples show this dark, oxidized surface, although HCl normally does not etch copper. This surface corrosion is also apparent in the images from the SEM, especially when compared with sample No. 2, which was not etched (see fig. 6.2). The comparison between the etched samples and the unetched one also shows an increase in the (surface) porosity during etching, although in principle, copper should not be etched by hydrochloric acid.

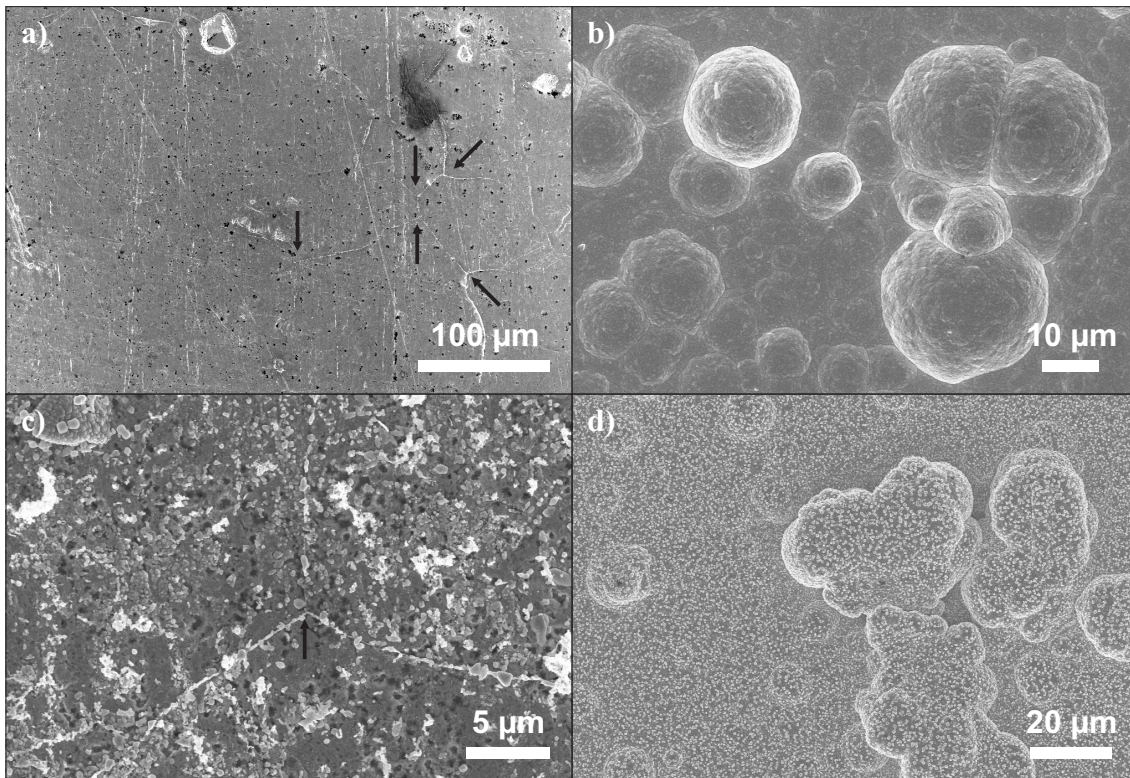


**Figure 6.2:** SEM images of the sample surface. a) Sn-side of the unetched samples 2. The black arrows mark the triple points of a hexagonal array of lines. b) Cu-side of the unetched sample 2. c) typical Sn- side of the etched samples. d) typical Cu-side of the etched samples.

The two different surfaces can be easily distinguished in all samples. The tin side - i.e. the side, where the tin foil was removed - shows a hexagonal pattern of raised lines with very regular triple points. This is probably a kind of imprint of the grain

boundaries of the original tin foil. Copper filled the grain boundary grooves and was left as a raised structure, when the tin was etched away. The copper side - i.e. the original surface of the electrodeposition - has a completely different appearance. Here large, round structures or "knolls" dominate the images.

A closer look at the surfaces revealed that during etching a large number of crystals of different sizes and shapes formed. The most commonly found are tetrahedral, hexahedral and cubic in shape and are shown in fig. 6.3. Crystals on the copper side are usually larger and better developed than the ones on the tin side.

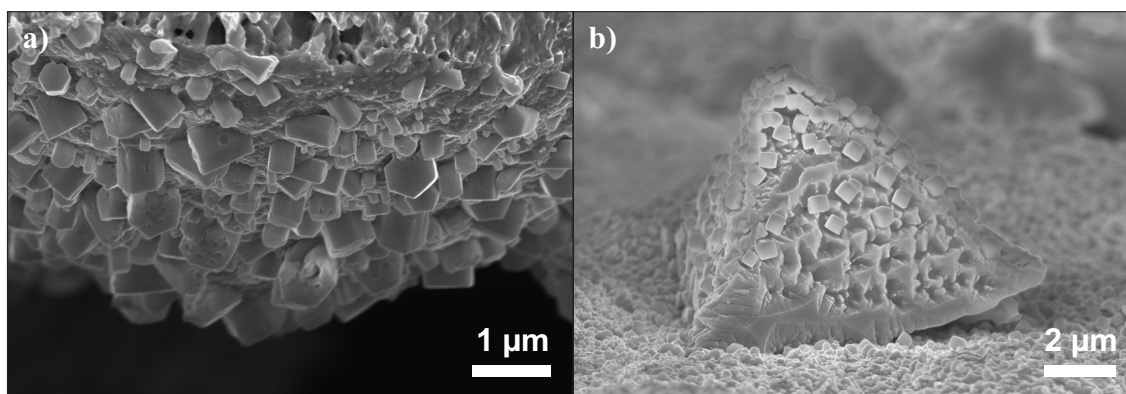


**Figure 6.3:** After etching of the samples, the surface is often covered with crystals: a) hexagonal crystals (probably cupric chloride) on the copper side of sample 10 b) tetrahedral (probably cuprous chloride) and cubic (probably sodium chloride) crystals on the copper side of sample 11.

Given the bath chemistry, the crystals can either be chlorides or oxides. EDX-measurements taken from the large tetrahedral crystals (see fig. 6.4 first spectrum) show a high chlorine peak. The chlorine signal for the cubic crystals (see fig.6.4 second spectrum) was much weaker. Yet these crystals are much smaller in size.

Most of the signal from the second area are therefore related to the pure copper sample underneath, which prevents a quantitative analysis, as the signal cannot be deconvoluted. Cuprous oxide ( $\text{Cu}_2\text{O}$ ) has a cubic structure, but normally, oxidizing copper samples do not form such nice crystals. The most probable explanation therefore is sodium chloride. However, the EDX measurements do not show a sodium peak, but this might be due to its proximity to the large copper peak and the small volume of these crystals. The most important peaks of the detected elements are given in table 6.3. In addition, there are several small copper peaks between

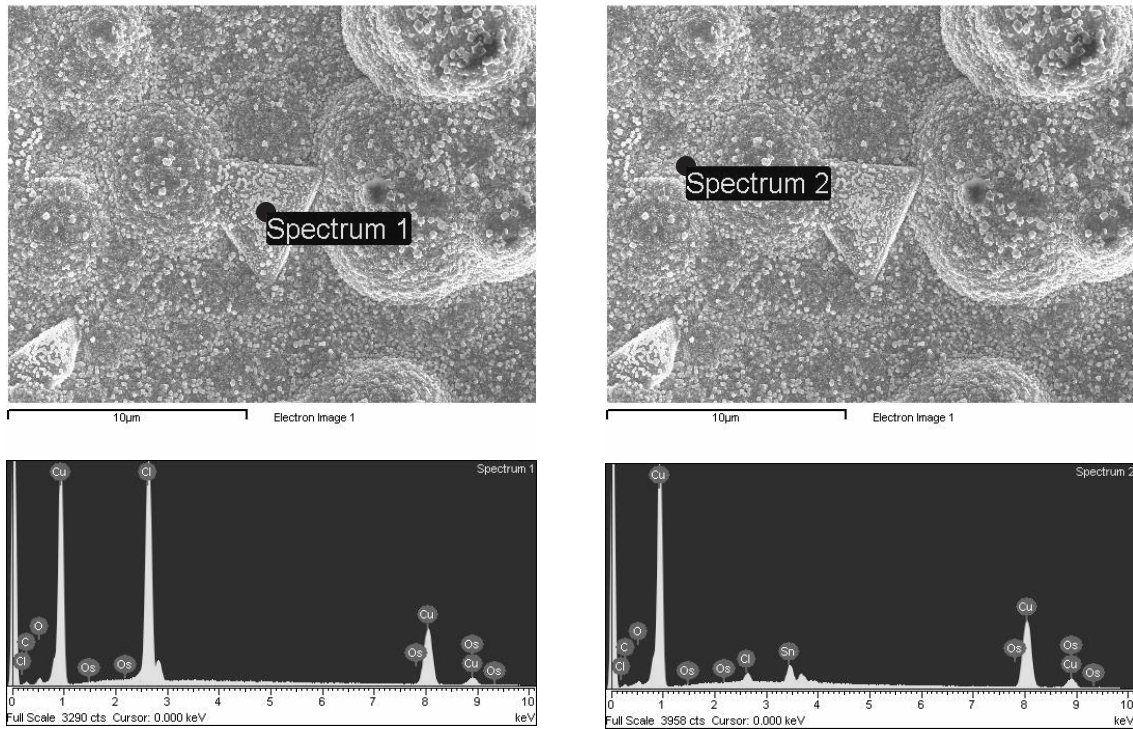


**Figure 6.4:** EDX-measurements from different sites on the copper surface of sample 11. a) the large tetrahedral crystals are apparently some kind of chloride, probably cuprous chloride. b) even on the Cu-side, a small amount of Sn can be detected.

0.832 keV and 1.023 keV, further masking any sodium, which might be present in the sample. The spectra also showed some Sn, although the images were taken on the Cu-side. This is probably due to some tin compounds being deposited from the etching bath.

**Table 6.3:** Energies of EDX peaks [98]

energy [keV]	element	transition
0.525	O	$K_{\alpha}$
0.930	Cu	$L_{\alpha 12}$
1.041	Na	$K_{\alpha}$
2.622	Cl	$K_{\alpha 1}$
3.443	Sn	$L_{\alpha 1}$
8.046	Cu	$K_{\alpha 1}$
8.904	Cu	$K_{\beta}$



As for the tetrahedral crystals, they are likely cuprous chloride or Cu(I) chloride, which has a zinkblende structure and tends to form tetrahedral crystals. Accordingly, the hexagonal crystals are probably cupric chloride or Cu(II) chloride, which crystallizes in a CdI-structure.

In some samples, the fracture surface was covered with small crystals or crystal-like deposits. Examples of these samples are given in fig. 6.5. As these samples had good results in the tensile testing and as no such deposits could be seen in the cross-sections, it is assumed that these crystals have grown after the tensile testing, maybe by resublimation. How this came about is not quite clear. In order to investigate the fracture surface and especially the nanotube density in the fracture surface, these samples had to be etched for 150s in diluted nitric acid (20 vol.%).

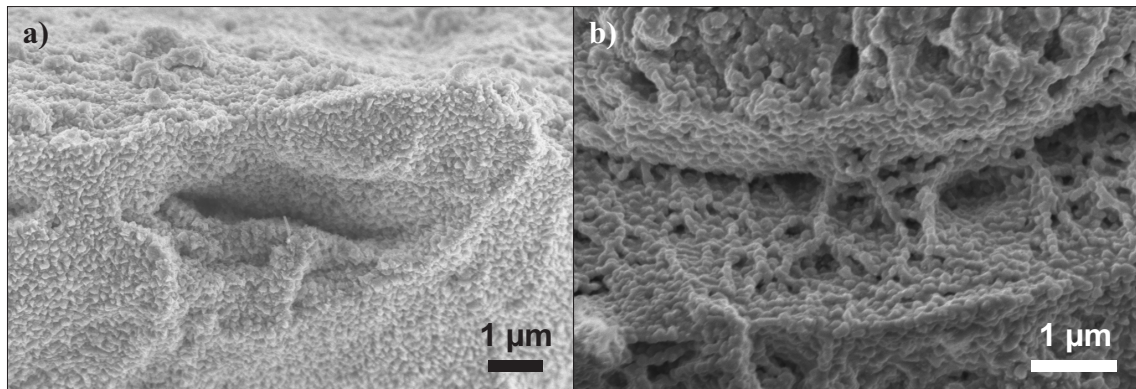


**Figure 6.5:** In some of the samples, the fracture surface was covered with small crystals, often tetrahedral-shaped. No indication of these crystals was found in the cross-sections, therefore they probably grew after the tensile testing. This layer had to be etched away to see the nanotubes.

All samples were cut at a distance of roughly 1 cm to the fracture surface to measure the thickness. It was found that some samples are markedly rougher than others. Examples of both are given in fig. 6.6. In the samples 1, 9, and 10 the roughness is on the order of the film thickness. For the calculations an average thickness was taken here. The other samples showed a more or less uniform thickness, with only a few knolls. Here, the thickness of the films without these knolls was taken.

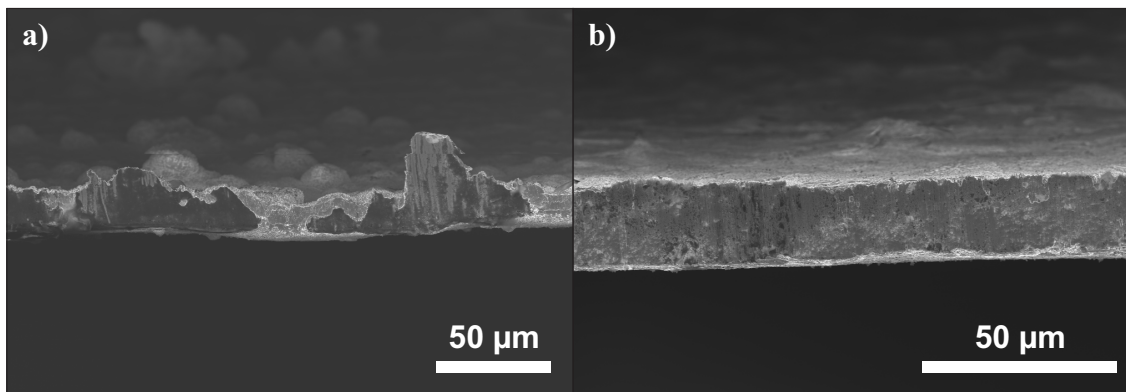


**Figure 6.6:** Each sample was cut to measure the thickness: a) example of a rough sample (no. 9) b) example of a smooth sample (no. 11).

### 6.2.2 Density of carbon nanotubes

At first, the small pieces of the sample left over from cutting out the dogbone tensile sample were tested for their carbon content. However, it was not possible to determine the weight fraction of carbon nanotubes, as the samples were too small and the carbon content thus below the threshold of detectability. It was then attempted to get an estimate of the number of nanotubes by etching away the copper matrix in diluted nitric acid (20 vol.%). It was not possible to arrive at a dependable volume fraction, as very few nanotubes became visible in that manner. Most were either etched away completely or were still firmly enclosed in the copper. Finally, after all other experiments were completed, another attempt was made at measuring the carbon content by chemical analysis. This time, the whole samples were used. For each sample, three measurements were made. However, although the carbon content was now above the threshold of detectability, the error was large. In fact, one of the carbon-free control samples showed higher carbon content than most of the other samples. This seems to be due to surface contamination. Therefore, the values give no hint of the amount of nanotubes incorporated in the samples. As all of the samples were burned completely for these test, no further experiments could be made. Therefore, there are no definite numbers for the amount of carbon nanotubes incorporated in the samples.

Finally, the samples were classified from the microscopical images of the fracture surface. Only nanotubes sticking out of the surface can be found here, and due to the fact that the surface is not planar, even those number are hard to interpret.

Therefore the samples were divided into three rough groups, keeping in mind that the samples within a group might vary to some extent.

The first group consists of the pure copper control samples (1, 2, and 3). As is expected, no nanotubes could be found here. The second group consisted of samples where nanotubes were easy to find and where most places showed a high density of nanotubes. Fig. 6.7 gives some examples of the different spots, nanotubes were found in, and what kind of nanotube densities were found there. Counting all clearly distinguishable nanotubes in several such images, a planar nanotube density of 1 nanotube per  $3 \mu\text{m}^2$  was estimated (based on a total area of several hundred  $\mu\text{m}^2$ ). The true value is probably higher, as low magnifications were used to get a better statistic and it was often hard to discern which structure contained a nanotube and which did not. This group is comprised of the samples 6, 7, 8, 11, 13, 14, and 15.

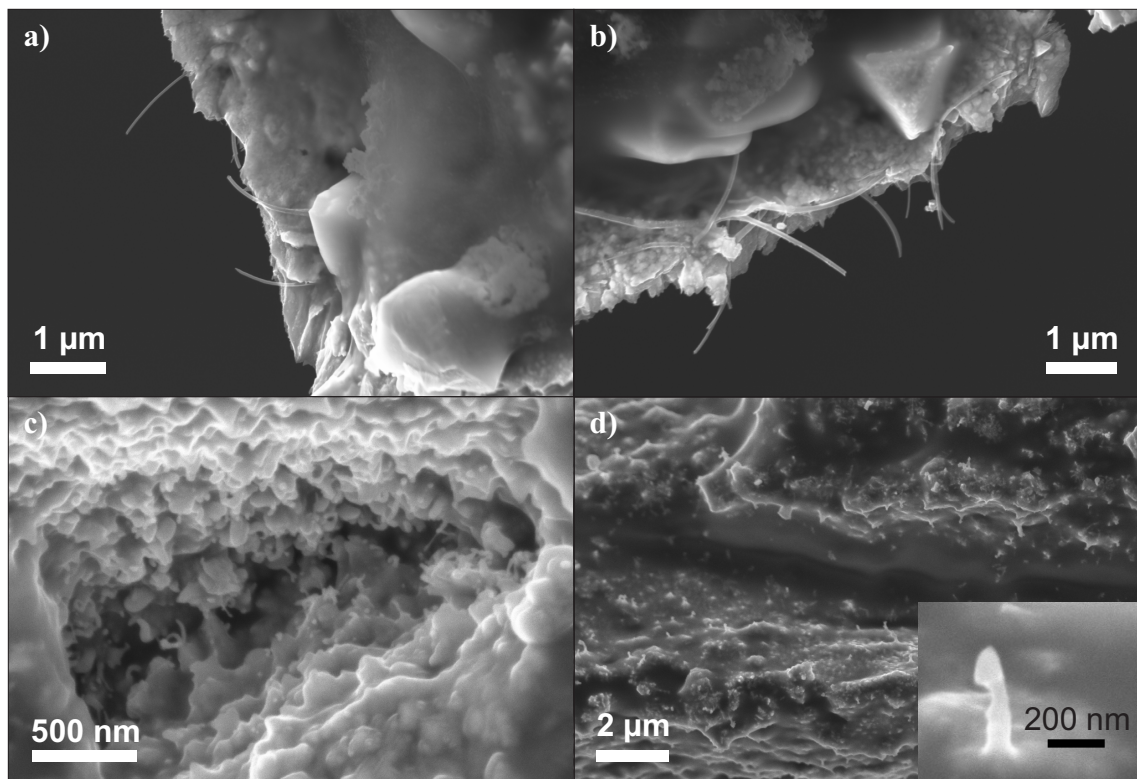


**Figure 6.7:** Exemplary images of samples which were rated as having a high nanotube density.

Nanotubes could be found in several sites: a) and b) sticking out of the fracture surface, thus visible in the top view of the sample (both images sample 11). c) lining the walls of cave-like openings in the fracture surface (sample 14). d) on the fracture surface itself (sample 14).

The last group contains the samples 4, 5, and 12. These samples showed some nanotubes, and sometimes even several at the same spot, but these sites were few

and far between, so that the overall nanotube density was markedly lower than for the samples of the second group. Since samples 4 and 5 had the lowest number of reinforced layers the low density was expected in these samples. Sample 12, however, should have had a lot more nanotubes and be quite similar to sample 11, as it was fabricated in the exact same way. The difference might be due to the fact that fewer of the nanotubes present in the wrapping paper were actually incorporated in the film. Yet it is more likely that the nanotube density in the paper itself was lower, as saturating the paper with the nanotube paste was done purely manually and the reproducibility of this process relied mainly on the skill of the experimenter.

### 6.2.3 Microscopical observations of the fracture site

Seen from the sample surface such as in fig. 6.8, all fracture sites looked very similar. On the tin side, there were small cracks in the close vicinity of the fatal fracture. On the copper side, the cracks were farther away, extended over longer distances and followed the baseline of the knoll-like morphology. The differences between the samples became evident, when looking at the fracture surface itself, i.d. in the direction of the arrow in fig. 6.8a.

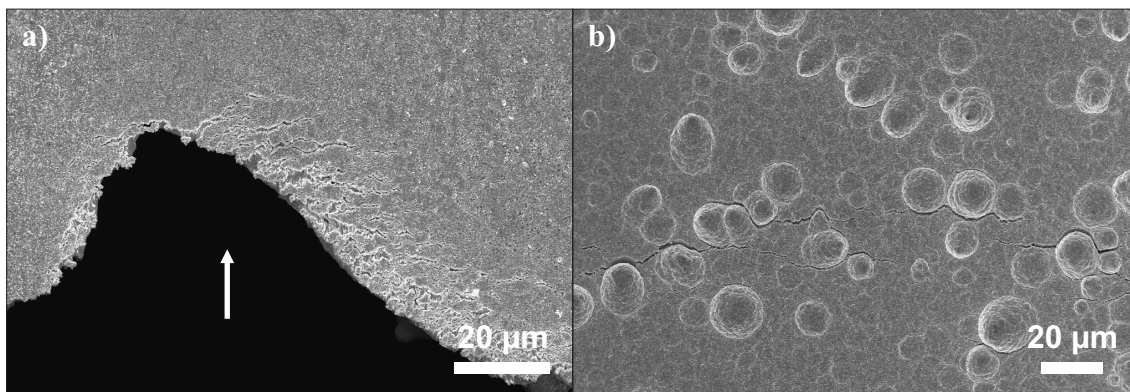


**Figure 6.8:** Near the fracture site, many smaller cracks can be found. a) On the tin side they are usually evenly spaced and show no special orientation (sample 13). b) On the copper side they usually follow the baseline of the knoll-like morphology (sample 3).

Typical fracture surfaces for both nanotube-reinforced and pure-copper samples are presented in fig. 6.9. Some things are the same for both types of samples. As stated before, the course of the fatal crack often follows the baseline of the knolls, and this is also often apparent in the images of the fracture surfaces. There is usually



a thin porous layer at the tin side (bottom of fig. 6.9a and b) and a thicker one on the copper side (top of these images). These layers are related to the oxidation of the sample during etching, as they are not seen in sample 2, the one that was not etched (see fig. 6.9c). These oxide layers fracture brittly, as is shown in 6.9d. Finally, the small circular pores should be mentioned, which can be found in all fracture surfaces, but not in the cross-sections that were artificially cut. As they are also found in the nanotube-free samples, they are not related to the presence of nanotubes but due to the ductile failure of the copper itself.

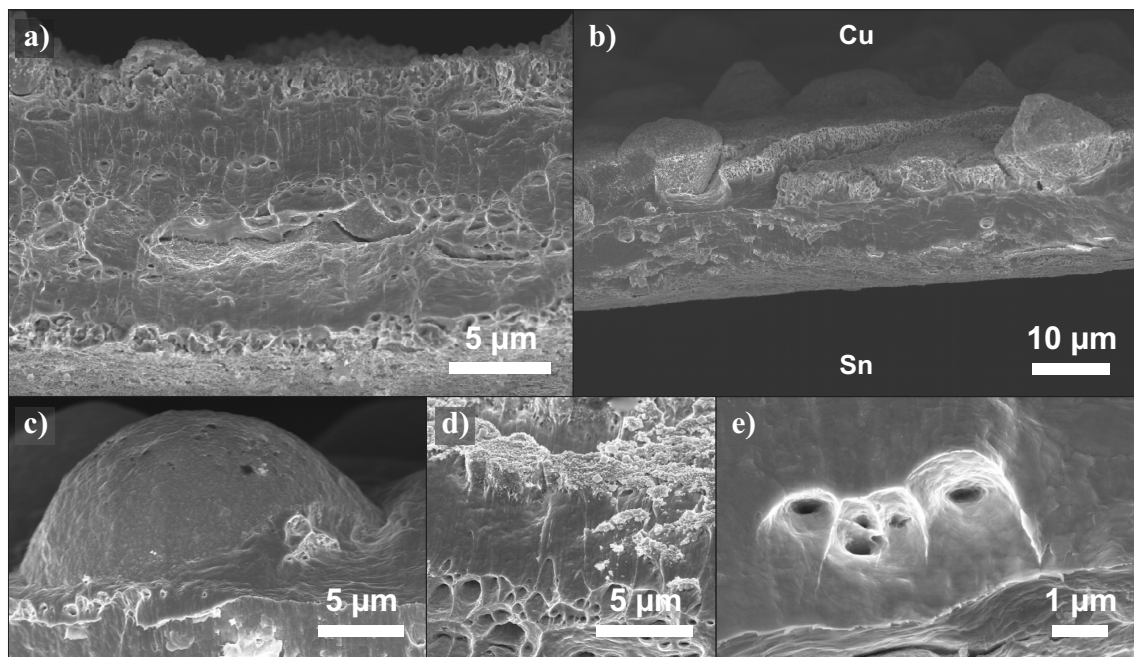


**Figure 6.9:** Typical fracture surfaces for the nanotube-reinforced as well as the pure-copper samples. Both types of samples have a smooth surface on the tin side, and a rougher surface with many knolls on the copper side. Porous surface layers can be found on both sides. a) The nanotube-reinforced samples frequently show cave-like openings in the fracture surface (sample 10) b) Such caves are almost completely absent in the nanotube-free samples (sample 3). c) The unetched sample 2 shows no porous layer. d) The porous layer fractures brittly (sample 11). e) Small circular pores are found in all samples (sample 2).

The fracture surface itself is in some places very smooth, in others it shows a honeycomb structure as shown in fig. 6.10. On the ridges of these structures, the copper often deformed to small sharp points. These can be easily mistaken for nanotubes, but they also appear in the pure-copper samples.

Upon closer inspection, there is a marked difference between nanotube-reinforced

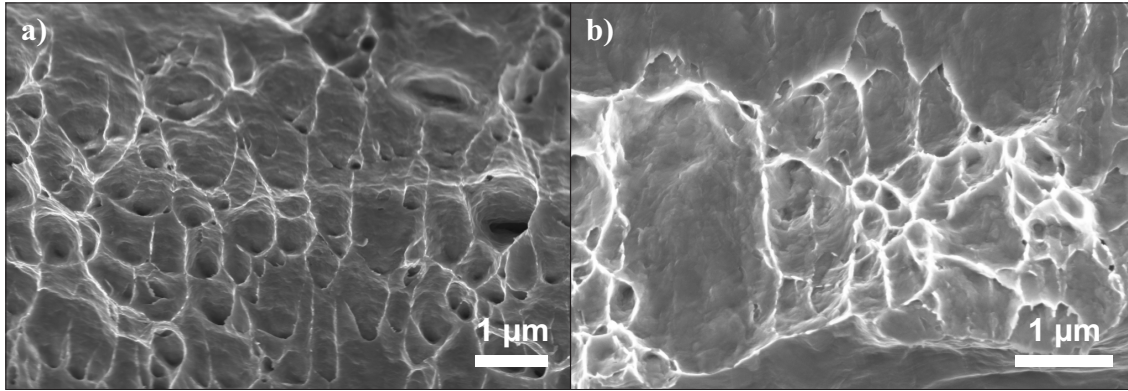


**Figure 6.10:** On the fracture surface, the copper usually forms a honeycomb structure. Along the walls of the honeycomb small tips or points form. As these occur also in the unreinforced samples, they cannot be related to carbon nanotubes. a) image from a nanotube-reinforced sample (sample 13). b) image from a nanotube-free sample (sample 2).

samples and pure-copper ones. In the nanotube-samples, often cave-like openings in the fracture surface appear. These caves usually have a curved shape and can be quite large. Their opening, however sometimes is quite small. Several of these caves are seen in fig. 6.9a as dark half moon shapes. Such caves, however, are very rare in the pure-copper samples. Instead, tongue-like protrusions were seen in each nanotube-free sample in large numbers (see fig. 6.11). No such protrusions were found in any of the other samples.

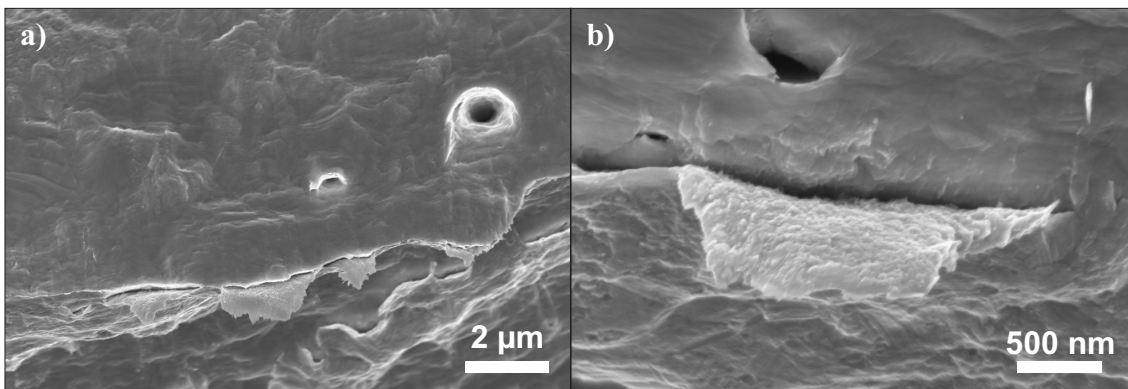


**Figure 6.11:** The samples containing no nanotubes showed very few of the cave-like openings, found commonly in the nanotube-reinforced samples. Instead, copper protrusions can be found in many places. These protrusions are absent in the nanotube-containing samples (both images sample 2).

The caves mentioned above are peculiar for another reason. In the nanotube-samples, both surfaces of these openings are filled with small pointed protrusions, looking very much like stalagmites and stalactites in a real cave (see fig. 6.12a).

Often, it is clear from the high aspect ratios of these protrusions that they formed around a nanotube (see fig. 6.12b). Caves and protrusions both were also more abundant in the samples with higher nanotube densities. In the few cases, where such a cave-like opening could be found in the nanotube-free samples, there were never any protrusions (see fig. 6.12c).

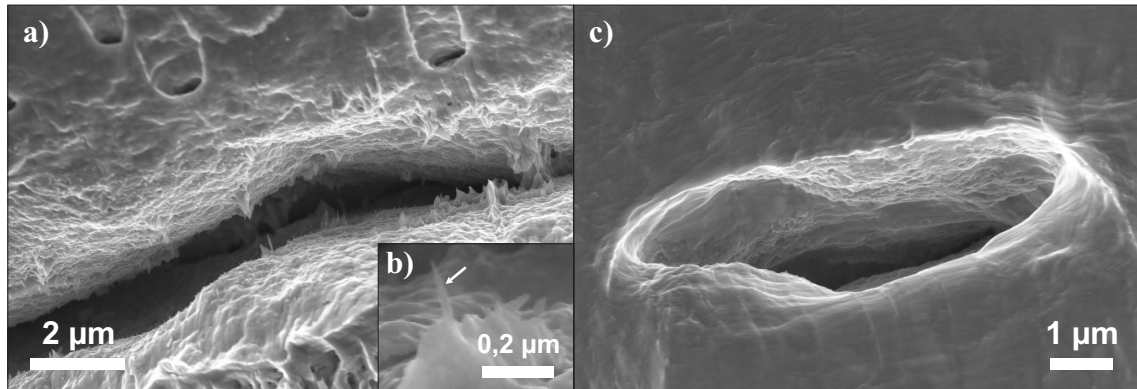


**Figure 6.12:** Especially in the nanotube-reinforced samples, cave-like openings in the fracture surface were found. a) In the samples with many nanotubes, a lot of these caves were found, showing large numbers of pointed protrusions. b) Some of these protrusions have such high aspect ratios that they seem to have formed around a nanotube (both images sample 11). c) In the samples with no nanotubes, such caves were extremely rare. If they were found, they never contained any protrusions (sample 2).

Samples 4 to 8 were made with varying sequences of reinforced and unreinforced copper layers. This had little influence on the appearance of the cross section. In the artificially cut cross-sections, no layers were visible in any sample. In the images of the fracture surface of sample 8, however, there were six raised "ridges", which extended over the full width of the sample, with five wider bands in between, which showed a rougher surface (see fig. 6.13a-c). This corresponds exactly with the six unreinforced copper layers, and the five times three reinforced layers. These layers only became visible, when the coating crystalline deposit on the fracture surface had been etched away (compare fig. 6.14b). Close-ups showed a sponge-like appearance of the reinforced layers with many thin columnar features. These might be copper-coated nanotubes which have resisted the etching as such a structure seems highly unusual for etched pure copper.

The layered structure itself is not due to etching, as samples 14 and 15, which also went through this step, showed no such layers. In sample 4 and 6, the layer



structures were also visible, but the layers could not be traced over a larger distance, and were hard to count, as they were often discontinuous. This might be due to the fact that these samples had more copper layers and thus thinner nanotube-reinforced bands.

Even if the exact sequence of layers was often not visible, some samples - 14, 15, and to a lesser extent 6 - showed large gaps or cracks, which extended over a considerable portion of the width, as is shown in fig. 6.13d. These gaps appear to be due to bad adhesion between adjacent layers, probably because of surface oxidation during the intervals between subsequent electrolytical cycles. If this is the case, these gaps would be perfectly parallel to the sample surface, and should therefore have little effect on the results of the tensile test.

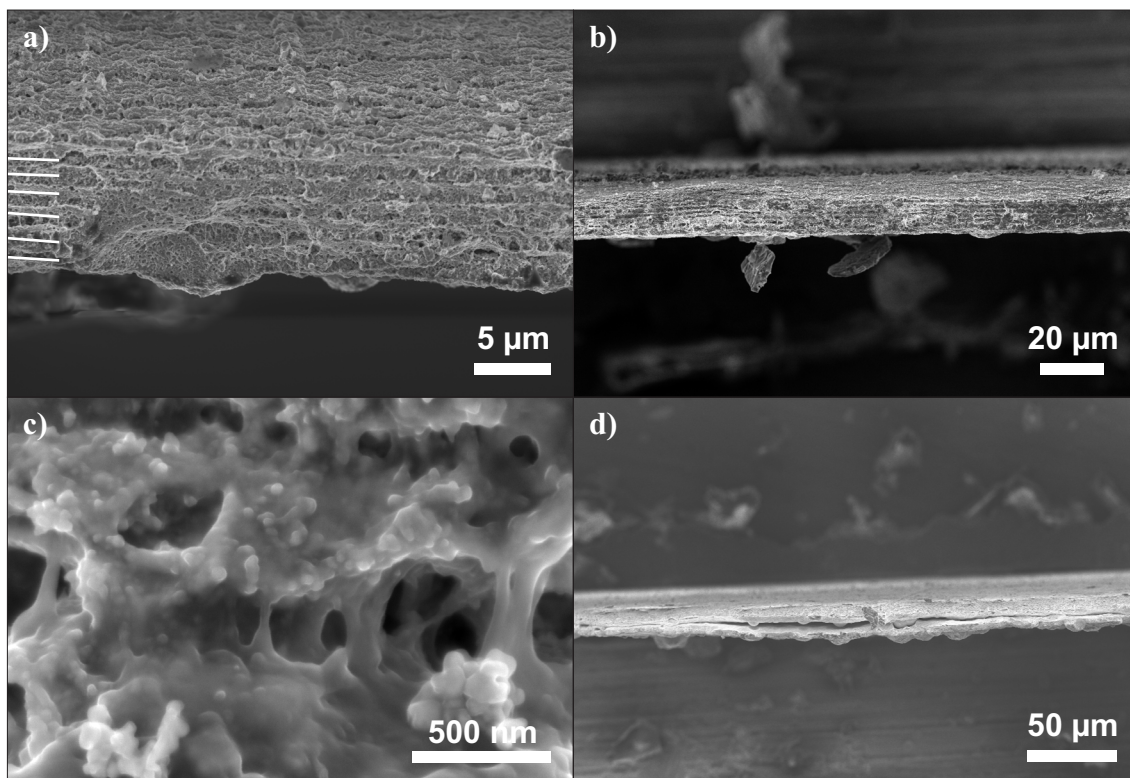


**Figure 6.13:** Images from sample 8 showing the layered structure of the sample. a) In the images of the etched fracture surface, the six unreinforced layers (marked by white lines) can be seen as raised ridges, with the wider bands of the reinforced layers in between. b) These layers are also visible in the unetched sample. c) After etching, a lot of column-like structures are found in the reinforced layers. d) This image of sample 14 shows a good example of a large gap, which formed at the interface between two adjacent layers, probably due to surface oxidation during the electrolytic cycling.

### 6.2.4 Coated and uncoated nanotubes

Nanotubes are not always easy to recognize in the images. If there are free nanotubes, i.e. not coated by metal, sticking out of the surface, it is usually no problem, but most of the nanotubes are, in fact, not free, but completely or partially coated with a thin layer of copper. For example, it is very hard to find nanotubes bridging a narrow gap or crack (some examples are presented in fig. 6.14). There are innumerable thin columns of copper in these places, but whether or not they contain any nanotubes is difficult to tell.

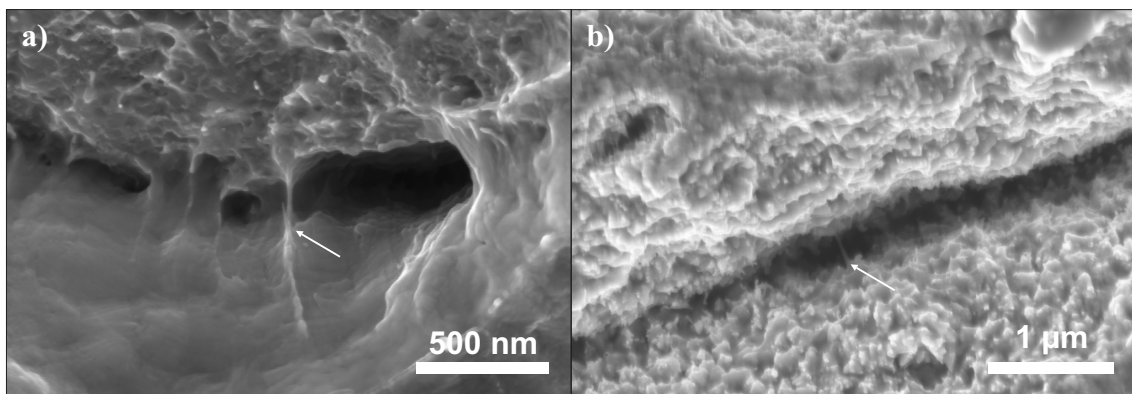


**Figure 6.14:** Sometimes, nanotubes bridging a narrow gap could be found. a) Image from sample 10. b) Image from sample 14. This image was taken before etching of the fracture surface. Therefore, the surface is still covered with some crystalline deposit.

Free nanotubes are often found in close vicinity to each other or even tangled (fig. 6.15), with large areas of the samples not showing any free nanotubes at all. This might be an indication that they were never coated to start with, maybe because of a lack in electric contact with the substrate. Most of the free nanotubes are embedded in the matrix at one end, but some can be found that are embedded at both ends (see. fig. 6.15).

Free nanotubes might also be due to a failure following the sword-in-sheath mechanism, in which one of the outer shells of the nanotube fails, and the inner core is pulled free. There was one image which suggests that such a mechanism took place at least sometimes. It is shown in fig. 6.16. Here, it appears that the outer shells which are coated with copper started to slip off the inner core, but failed to do so completely. However, this kind of structure was observed only this one time and it was not possible to detect any holes in the fracture surface which were clearly

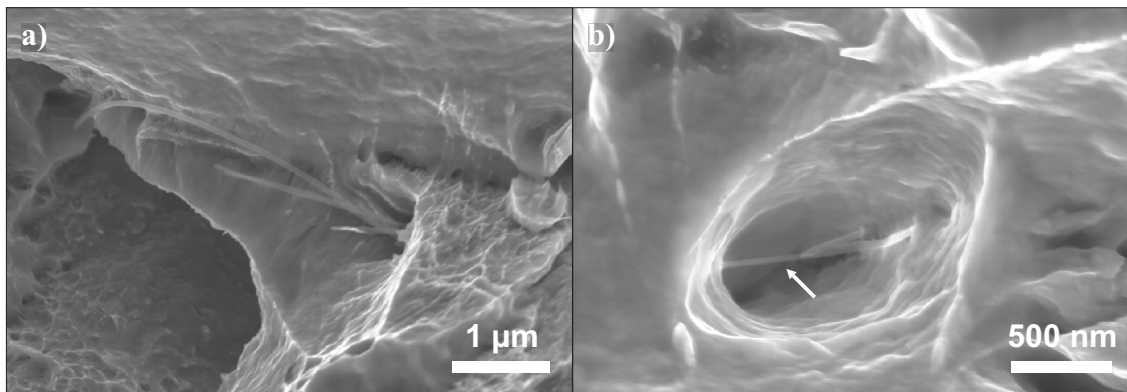


**Figure 6.15:** In most samples, nanotubes which are not coated by metal can be found. a) Often, these nanotubes occur in groups (sample 13). b) In a few cases, the nanotube seems to be embedded at both ends (sample 11). Although such uncoated nanotubes were found in most samples, their number is small when compared to that of the coated ones.

due to pulled-out nanotubes.

When comparing the total numbers of coated vs. uncoated nanotubes, the uncoated ones were a small minority, although they were found in most of the nanotube-containing samples. Coated nanotubes were, however, much more common, even when taking into account that they are a lot harder to detect. To be sure that a certain protrusion is a nanotube, one has to see any one of three signs: either the straight and perfectly parallel sides of a nanotube, the double contrast of the hollow tube (usually only visible in free NTs), or an aspect ratio markedly larger than the one found in the protrusions of the pure copper.

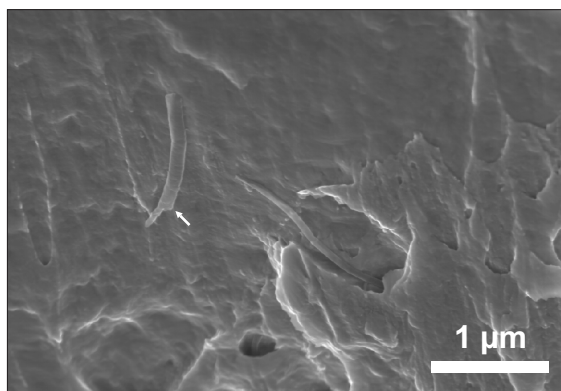


**Figure 6.16:** This structure might have been caused by a sword-in-sheath mechanism, in which one of the outer shells breaks, and is pulled off the inner core. This image might show a site, at which this pulling-off was not completed, leaving the copper-coated outer tubes still in contact with the inner core. No other sites like this could be found (sample 11).

Two examples are given in fig. 6.17. In the first image, the points on both sides of the crack are much longer than the ones found in pure copper. There has to be some kind of support to allow the copper to be drawn to protrusion of such a high aspect ratio. The second image is even clearer. The nanotube was pulled free of the matrix, but the copper adhered at its base and was deformed to a little point, similar to the images shown in the previous chapter. The tip of the nanotube, however, is either free or coated with a copper film of very uniform thickness, thus retaining the perfectly straight and parallel lines of the nanotube.

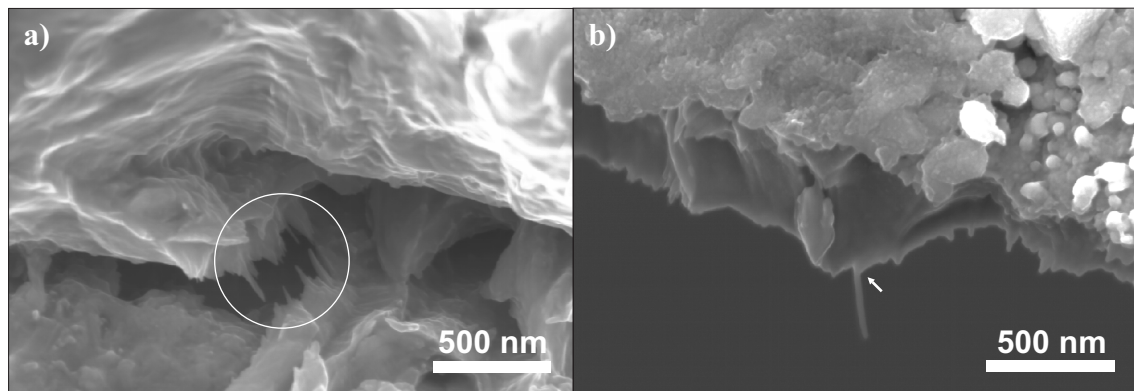


**Figure 6.17:** Examples of nanotubes still coated with copper. a) Structures similar to the protrusions in the cave-like openings were often found in small cracks. They are too long and thin to consist purely of copper. b) Here, the matrix was deformed around the base of the nanotube forming a little tip. The nanotube can be clearly identified by its straight and parallel sides (both images sample 11).

### 6.2.5 Stress-strain measurements

Fig. 6.18 shows the stress-strain curves of all the tensile samples, split into four groups for better clarity. The first diagram shows the samples with high roughness (see p. 127). These samples broke at low strains and stresses as is to be expected, since the stresses were calculated with an average thickness and the high roughness causes considerable stress concentrations, which promote early fracture. The next diagram shows the pure-copper samples. (Note that sample 1 already appeared in the first diagram.) The difference between samples 1 and 3 gives some indication as to the influence of the sample roughness, as sample 3 was very smooth. Sample 2, on the other hand, was the only one that was not etched to be removed from the



tin foil, and it is the only sample that didn't show brittle failure. In the second row are the smooth samples reinforced with nanotubes. On the left the ones with few nanotubes, on the right the ones with many (see p. 129). The samples with the highest nanotube content clearly show the highest strength and breaking strain.

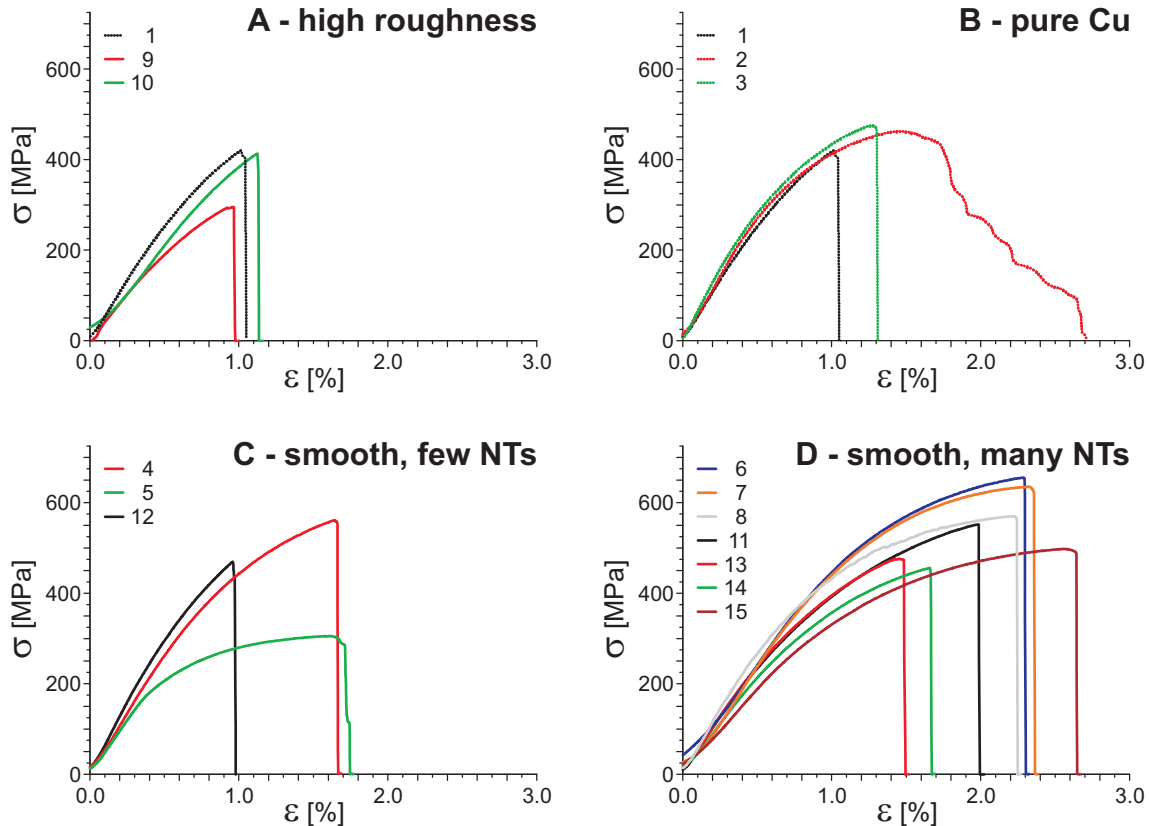


**Figure 6.18:** Stress-strain curves of all electrolytical tensile samples: A - samples with a rough surface. B - samples without any nanotubes (note that sample 1 appears both in A and B). C - smooth samples which showed few nanotubes in the SEM. D - smooth samples which showed many nanotubes in the SEM.

The energy to failure (i.e. the area under the curves) given in fig. 6.19a shows the difference in the four groups even more clearly. The values are very low for the rough samples (marked in yellow), due to their premature fracture. The samples with few nanotubes (light blue) show little improvement over the nanotube-free samples (grey). An exception is the unetched sample 2, which has a much higher energy to failure, due to its ductility. Although the samples with many nanotubes (dark blue) show the brittle failure of all etched samples, they reach on average energy values comparable to that of sample 2. Some of them reach even higher values, due to their increased strength.

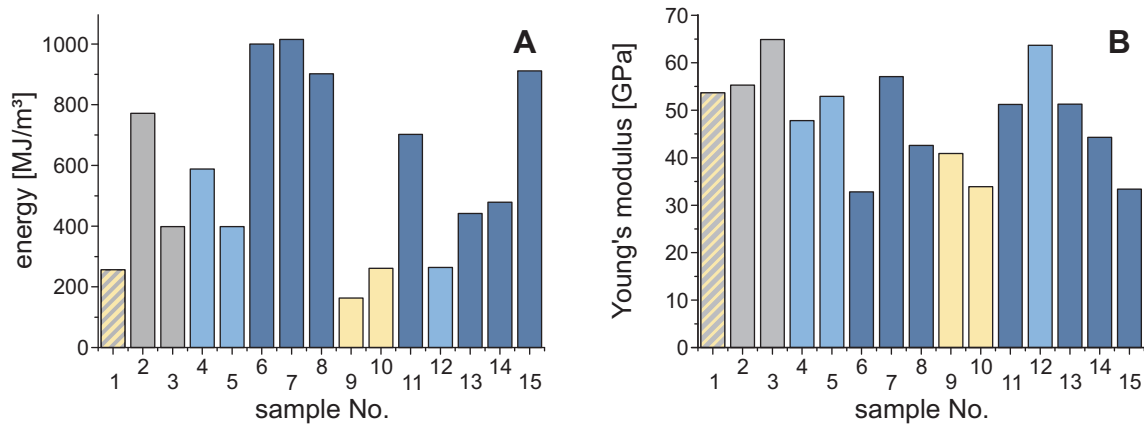


**Figure 6.19:** Energy to failure and Young's modulus for all samples. a) The rough samples (yellow) show markedly smaller energy to failure-values, as do the CN<sub>x</sub>-free samples (grey), except for no. 2, which was not etched. The samples which show many nanotubes in the SEM (dark blue) are tougher on average than the ones with few CN<sub>x</sub> (light blue). b) No such relations are apparent in the Young's modulus.

No such relations are apparent for the Young's modulus shown in fig. 6.19b. Although there is some variation, and the stiffest samples have almost twice the modulus of the weakest ones, there appears to be no correlation to the nanotube density. It should be noted, however that three of the weaker samples (6, 14, and 15) are the ones showing large cracks and gaps (see p. 134).

## 6.3 Discussion

### 6.3.1 Increased fracture resistance in reinforced samples

As can be seen from the values for the energy to failure, a rough sample surface is very detrimental to the mechanical properties, due to the stress concentrations it implies. For this reason, the samples 1, 9, and 10 will not be discussed any further. These samples were among the first to be produced (three out of the first four, the fourth being sample 11), which indicates that the processing requires a certain level of experience to result in smooth samples.

Unfortunately, it was not possible to determine the exact volume fraction of carbon nanotubes in the samples. Instead, the samples had to be classified on the basis of the microscopical images. Such a classification is rather broad, which may

explain some of the variation within the different groups. Part of the variation is also due to the fabrication of the samples, as the application of the nanotube-containing paste is done manually, with no means to ensure a constant concentration. However, as can be seen in fig. 6.19, the samples containing few nanotubes are on the left side of the figure (as they have low sample numbers), whereas the ones with many nanotubes are on the right (having higher sampler numbers). As the samples were numbered in accordance with the estimated nanotube content (as based on the percentage of reinforced layers - see table 6.2), this indicates that the level of nanotube incorporation was on average more or less constant. The only exception to this is sample 12.

Even without knowing the absolute density of the nitrogen doped nanotubes in the samples, some conclusions can be drawn. All samples, except for sample 2, showed a brittle failure, without any plastic regime apparent in the stress-strain-curves. This is clearly related to the etching step, as sample 2 is the only one, which did not undergo this process. However, there are no indications in the literature that HCl or molecular hydrogen (which develops during etching) should have such detrimental effects on copper [99]. On the other hand, the etching also seems to be responsible for the oxide layer at the sample surfaces. As these layers show a very brittle behavior, they might act as crack sources, thereby giving rise to the brittle fracture of the sample as a whole. Of the three control samples, sample 1 was very rough, whereas sample 2 was not etched, thus showing ductile fracture and a stress-strain-curve very different from the rest of the samples. This makes sample 3 the best to compare with the reinforced ones.

The samples with few nanotubes show little improvement over the nanotube-free samples. As the difference is on the order of the variation within the groups themselves, little can be said about the effectiveness of the reinforcement in these samples. The samples with many nanotubes, however, show a strong increase (up to 150%) in the energy to failure when compared to sample 3. All of them are better in that aspect than sample 3, and four of them (samples 6, 7, 8 and 15) are even better than the unetched sample 2 with its ductile behavior.

This increase in energy to failure can be explained by the micrographs from the fracture surfaces. The nanotube-rich samples all show many of the cave-like

openings and also many protrusions within these openings. As no such caves were observed in the artificially cut cross-section, they appear to have been formed during the fracture of the sample. The creation of these structures absorbs a lot of energy, due to crack deflection, debonding of tubes and pull-out of nanotubes. All these mechanisms are correlated with an increase in surface area. The increase in surface area is especially pronounced for the samples 4, 6, and 8 with their layered structure. Sample 4 did not contain enough nanotubes to show the excellent results of the other two. It is, however, the best among the samples with few nanotubes.

The Young's modulus is not influenced by the addition of nanotubes, which is to be expected for these low volume fractions, as composite theory suggest a pure rule of mixture for the effect of fiber reinforcement on the modulus. The variation between the different samples is very high, and the absolute values are only approximately one third of the bulk value of 110 GPa. It should be noted that some of the samples with the lowest Young's modulus (samples 6, 14, and 15) are the ones with large gaps due to bad inter-layer adhesion (see fig 6.13d), even if these gaps should theoretically not influence the mechanical properties of the samples under the given testing conditions.

### 6.3.2 Signs of adhesion between nanotubes and matrix

Similar to the results presented in the previous chapter, the microscopical analysis of the samples showed many indications for good adhesion between the nitrogen-doped nanotubes and the copper matrix. Some of the nanotubes found at the fracture surface were free of copper. There was one site (see fig. 6.16), which may be an case of a sword-in-sheath mechanism. As this mechanism requires a stress transfer from the matrix to the fiber, this site can be taken as an indication of good adhesion. For the other uncoated nanotubes, a sword-in-sheath mechanism cannot be proven and in the few cases, where the uncoated nanotubes is embedded in the matrix at both ends (fig. 6.15b) it is highly unlikely. Most of these nanotubes are therefore either due to bad adhesion at the interface, or were never coated at all.

However, as the uncoated nanotubes are by far outnumbered by the ones coated in copper, their influence on the mechanical properties is small. In fact, sites where

the copper forms long, thin tips around a nanotube are numerous, especially in the cave-like openings. Thus, in the vast majority of cases, the site of failure was within the copper matrix itself. This indicates that the interfacial strength is on the order of the shear strength of copper or higher. Whether the ability of the interface to transfer shear stresses is due to friction or to an actual chemical bonding is not clear. Yet as carbon nanotubes - even the nitrogen doped ones used in these samples - have an outer shell of very little roughness (pure carbon nanotubes have even been suggested as nearly friction-free linear bearings for MEMS-applications [100]), it seems more likely that the stress transfer is due to chemical bonding. The good adhesion might therefore be due to a large extent to the use of nitrogen-doped tubes. However, as the results presented in the last chapter have shown, a good adhesion is also possible with pure-carbon nanotubes.

### 6.3.3 Implications for further research

The experiments presented here have shown that it is possible to fabricate semi-bulk samples of carbon nanotube-reinforced metals via electrodeposition. The reinforced samples show a large increase in the energy absorbed before fatal fracture when compared to the nanotube-free control samples. However, a high surface roughness and the formation of a brittle oxide layer at the surface can severely weaken the samples. Further research is needed in order to establish a fabrication procedure which prevents this.

Although the experiments have shown that the stress transfer from matrix to fiber can be of the order of the shear strength of copper, the exact (maximum) value for the interfacial strength is not known, neither are the factors which influence it. One step towards this goal would be to repeat the experiments presented here with pure-carbon nanotubes, but for exact measurements experiments on the micro-scale are needed. Due to the small size of nanotubes, such experiments will not be trivial as they will have to be conducted in an SEM, AFM or the like with near certainty.

For several years already, carbon nanotubes have been discussed as reinforcement fibers for metal matrix composites. Their mechanical properties and the huge aspect ratios seem to make them an ideal material for this purpose. However, so far it was

not clear, whether carbon nanotubes could actually be bonded to the matrix strongly enough to ensure an efficient stress transfer, which is the prerequisite for a successful use as reinforcement. The experiments presented here have shown that it is indeed possible to get such good stress transfer, although much effort is still needed until carbon nanotube reinforced metals can be tailored to a specific application.

## 6.4 Summary and Conclusion

Nanotube-reinforced copper films have been produced by electrodeposition using nitrogen doped carbon nanotubes. The films were removed from the substrate through etching in hydrochloric acid and tensile tests were performed on the freestanding films. Afterwards, the fracture surfaces were studied in an SEM. Although several techniques were tried, it was unfortunately not possible to determine the actual carbon content in the samples. Therefore, estimates had to be made from the SEM images.

Samples containing many nanotubes showed a strong increase in the breaking strain and energy to failure when compared to the nanotube-free control samples. However, the etching process proved to be detrimental to the mechanical properties, nearly halving the toughness of the samples and leading to brittle fracture. Also, when compared to bulk copper, the values for the breaking strain are very low. This might be due to cracking induced by the brittle oxide layer formed during etching.

It has been shown that adhesion between the nitrogen-doped nanotubes and the copper matrix is in most cases very good and actually in the same range as the maximum shear strength of the copper. As has been shown in the last chapter (see ps. 105) such good adhesion can also be achieved with pure carbon nanotubes. It would therefore be interesting to prepare samples with pure carbon nanotubes, to see, whether their better mechanical properties would lead to an even higher increase in toughness.

As long as the nanotube densities remain low, no influence on the Young's modulus is to be expected. However, due to the good adhesion, higher moduli are to be expected, if one arrives at a way to incorporate more nanotubes in the composite.





## Chapter 7

### Summary and outlook

Carbon nanotubes offer a range of properties that make them interesting reinforcement fibers for metal matrix composites. Exceptionally high Young's modulus and tensile strength are combined with low density and high flexibility. In addition, carbon nanotubes usually have very large aspect ratios, which are necessary for an effective stress transfer from fiber to matrix. To fully evaluate the potential of carbon nanotube reinforced metals, however, it is necessary to understand the interaction of carbon nanotubes and the metal matrix, and the properties of the interface.

To make full use of the potential of carbon nanotubes as reinforcement fibers, a certain interfacial strength is needed to transfer stresses from the fiber to the matrix. Yet so far, no experimental results have been published regarding the shear strength of a metal/nanotube interface. On the contrary, it was often assumed that there would be no adhesion, as perfect carbon nanotubes have a chemically saturated surface and present therefore no anchoring points for a metallic matrix. Results from wetting experiments with conventional carbon fibers point in the same direction, wetting is only observed if a stable carbide can form at the interface. However, if the metal reacts easily with carbide, the tiny nanotubes might well be dissolved completely. To judge the potential of carbon nanotubes as reinforcement fiber for metal matrix nanotubes, it is therefore of high interest to study the interfacial strength.

To this end, two different model composites were developed. Both used nitrogen-doped carbon nanotubes as reinforcement fiber, as these tubes have a higher defect

density, thus offering more attachment sites for the matrix. These tubes were produced using an aerosol-based CVD-process with a mixture of ferrocene and benzyl amine as precursor solution. The resulting tubes showed the typical disturbed bamboo-structure of nitrogen-doped nanotubes.

In the first of the model composites, magnetron sputtering was used to deposit a thin copper film on a silicon substrate. On this film, carbon nanotubes were deposited from solution, before a second copper film was deposited, again via magnetron sputtering. Ethanol was found to be the best solvent in regard to the cleanliness of the interface between the two copper layers. However, as ethanol is not a good dispersant for carbon nanotubes, the nanotube density had to be kept low to avoid agglomerations. As long as the nanotubes were well separated, the second copper layer coated them well, with now shadowing-effects or pore-formation.

As the sputtering process is highly conformal, the location and orientation of the individual nanotubes is clearly visible. It was thus possible to cut samples with a defined orientation of the nanotube using a focused ion beam microscope. In particular, it was possible to cut TEM samples, in which the nanotube is perpendicular to the sample, thus allowing to study the structure of the interface.

Again using the FIB, columns with a diameter of approx. 600 nm were cut from these composite films and tested in microcompression. Some of these columns show deformation through twinning, which has never before been reported for microcolumns and which is also unexpected from results of macroscopic samples of unalloyed copper. Most columns show a larger strain in the upper copper layer. The extend of the strain localization, however, could not be correlated to the tapering angle of the columns. No influence of the nanotubes on the overall deformation behavior could be detected. However, in the close vicinity of the nanotubes, a funnel-shaped depression formed during deformation, indicating that there is indeed adhesion between nanotube and matrix. In addition, TEM samples were prepared from the columns. The images again show the funneling effect, indicative of good interfacial shear strength and in one case might show a case of nanotube fracture due to the transverse elongation of the column. As only two samples could be studied in the TEM, the results are preliminary but the method has proven suitable for further study.

For the second model composite, electrodeposition was used. To increase the density of nanotubes in the material, they were not dispersed in the electrolyte itself, but applied to a paper wrapped around the tin substrate. As electrolysis is a very fast deposition process, it was possible to produce films of approx. 20  $\mu\text{m}$  thickness. The tin substrate was then etched away and the resulting free-standing films were tested in a conventional tensile test.

The stress-strain curves showed no change in the Young's modulus of the samples, as was expected for the rather low nanotube content in the samples. However, the samples with the highest nanotube concentrations did show an increase of more than 100% in the energy to failure when compared to the unreinforced control samples. All samples but the one, which was not etched, showed brittle fracture, probably due to the formation of a brittle surface layer during the etching process.

The study of the fracture surfaces showed many places, in which copper adhered to the carbon nanotubes, creating stalagmite-like structures, and crack deflections in the shape of cave-like openings. These structures were especially common in the toughest samples, and absent in the nanotube-free control samples. However, if a nanotube, which had been pulled out of the matrix, is still coated with copper, the interface must be stronger than the shear strength of copper itself. Uncoated nanotubes, which might be due to a failure of the interface, were also found, but they were vastly outnumbered by the copper-coated ones.

Finally, the electrolytic process was also applied to some samples of carbon nanotube carpets (both aligned with low density and unaligned with higher density). Here, as well as in the other electrolytical samples, it was found that the copper deposits preferentially on the carbon nanotubes, especially at the tips. This is due to geometric effects, which lead to a higher electric field density at protrusions from the sample surface. With these nanotube carpets, it was possible to achieve a high nanotube density in the composite material although no fully dense films were produced. When stressing these structures using nanoindentation, again many signs of good adhesion between copper and nanotubes were found. In several places, nanotubes could be found which had been pulled out of the matrix, but which were still coated with a thin layer of copper, thus indicating that the interfacial strength can be larger than the shear strength of the copper matrix itself. In others, cracks were

seen with nanotubes which had clearly fractured due to interfacial stress transfer, showing no or only limited pull-out. This is especially noteworthy, as the nanotubes in these carpets were not nitrogen-doped and should thus possess fewer defects which might act as anchoring points for the matrix.

## Outlook

Polymer matrix composites reinforced by carbon nanotubes have been studied extensively and are now beginning to be used in commercial applications. Metal-CNT composites, on the other hand, are just beginning to be investigated. Although some promising results on the macroscopic behavior of such composites have been published, very little is known concerning the microscopic mechanisms underlying the reinforcement effect. Especially the topic of adhesion and wetting of carbon nanotubes by metals is still unclear, as few results have been published and these sometimes contradict each other. So far it was assumed that nanotubes are wetted mostly, when carbides are formed, with no or little adhesion in the case of other metals. Copper has not been studied, but for gold no adhesion was found.

In all the experiments presented here, however, evidence was found that it is possible to have good adhesion between carbon nanotubes and a copper matrix. Although not all nanotubes showed this high interfacial strength, these cases were few and far outnumbered by the ones that did. Good adhesion, however, is necessary for the transfer of mechanical stresses from the matrix to the fiber and thus crucial for a successful composite material.

There is still very little literature on carbon nanotube reinforced metals and hardly any studies on the mechanisms responsible for the strengthening effect observed. Further study is needed to understand what happens at the interface of carbon nanotubes and metals and how the interfacial strength can be influenced. The model composites presented in this work are well suited for such further studies and a few suggestions will be given here.

It would be of high interest to measure the actual interfacial shear strength between a nanotube and the matrix. The electrolytically covered nanotube carpets would be a good starting point for this. As long as the deposition time is kept low,

only the tips of the nanotubes are covered in copper. Thus, it should be possible to pick up individual nanotubes and conduct an *in-situ* tensile test, using the method described by Orso et al. [101]. Another interesting line of thought would be to try and increase the density of the carbon nanotube carpets, thus maybe achieving a copper film with a uniformly high density of nanotubes.

For the randomly reinforced electrolytic samples, it would be most important to lessen the detrimental influence of the etching step. This might be solved by switching to a different substrate, and introducing a sacrificial layer at the interface, which can be removed more easily. Also, the overall quality and reproducibility of the process could be improved to see, if these reinforced films do not only compare well to carbon-free films produced in the same way, but also to bulk copper.

The films produced by magnetron sputtering also provide opportunities for further experiments, especially in combination with the FIB. TEM studies could make use of the fact that the angle, under which the nanotube is cut, can be chosen at will. Using analytical TEM on samples with perpendicular nanotubes, much information on the chemical make-up of the interface could be won.

To understand the role of the nanotube within a deformed matrix, a follow-up of the pillar work is promising. Using different levels of deformation, much could be learned of the interaction of dislocations with the nanotube and the mechanisms of slip, axial compression and breakage of the nanotube. To this end, the TEM work would need to be intensified, using samples, in which the nanotubes have been cut at different, well-defined angles.

In the pillars, the nanotubes are mainly stressed through the transverse elongation during compression. A more direct loading could be achieved by cutting microbeams with the FIB and loading them in tension or in bending, as was demonstrated by Motz et al. [102]. Again, the conformity of the sputtering process would be very beneficial, as it allows to choose the orientation of the nanotube in regard to the beam.

Carbon nanotube in metal matrix composites remain an interesting topic of study. Much is still unclear, yet the results obtained so far, are highly encouraging. The model composites presented in this work provide a foundation for further studies on the interaction of nanotubes and metal matrices.



# List of Figures

2.1	Chirality in carbon nanotubes . . . . .	32
2.2	TEM image of a multi-walled carbon nanotube . . . . .	33
2.3	CNT-carpet grown by aerosol-based CVD . . . . .	35
2.4	Schematic representation of two models for nanotube growth . . . . .	36
2.5	Buckling in MWNTs . . . . .	41
2.6	Collective buckling in MWNT-carpets . . . . .	41
2.7	Elements and their wetting behavior concerning carbon . . . . .	44
2.8	TEM images of nitrogen-doped nanotubes . . . . .	45
2.9	Lattice sites for nitrogen dopant atoms . . . . .	45
2.10	Schematic stress-strain-curve of fiber reinforced composites . . . . .	47
2.11	Deformation mechanisms in CNT-reinforced alumina . . . . .	51
2.12	Cu/CNT composites produced by molecular mixing . . . . .	53
2.13	Pt/CNT composites produced by electrodeposition . . . . .	55
2.14	Skewered-dumpling shape of Ni/CNT composite powders . . . . .	55
3.1	Schematic cross section of a Cu/NT/Cu-composite . . . . .	60
3.2	Schematic drawing of the aerosol-generator . . . . .	61
3.3	CVD-setup for the production of carbon nanotubes . . . . .	61
3.4	Solvents tested for dispersing ability of $CN_x$ . . . . .	63
3.5	Wafer prepared according to the procedure of Lay et al. . . . .	64
3.6	Wafer prepared by the solution-drying method . . . . .	65
3.7	Wafer prepared by the drop-drying method . . . . .	66
3.8	Wafer cleanliness and NT concentration vs. no. of spraying cycles . .	68



3.9	Nanotube density vs. number of spraying cycles . . . . .	69
3.10	Agglomeration of NTs on a wafer(cyclic spraying method) . . . . .	69
3.11	Visibility of NTs with/without Cu top layer . . . . .	70
3.12	Cross section of a wafer with a 1 $\mu\text{m}$ -thick copper top layer . . . . .	70
3.13	TEM image of a nanotube at the interface of the two copper layers . . . . .	72
4.1	Geometry of the microcolumns . . . . .	78
4.2	Redeposition during FIB milling . . . . .	81
4.3	SEM images of all columns after deformation . . . . .	83
4.4	Stress-strain curves with/without nanotubes . . . . .	84
4.5	Stress-strain curves of evenly/inhomogeneously deformed columns . . . . .	86
4.6	Strain in upper and lower Cu layer in relation to taper angle . . . . .	87
4.7	Grain growth during FIB milling . . . . .	88
4.8	TEM image of columns 6 and 3 - overview . . . . .	90
4.9	Schematic drawing of deformation via slip and twinning . . . . .	91
4.10	Stress-strain curves of slip- vs. twin-deformed columns . . . . .	93
4.11	High resolution TEM images of nanotubes . . . . .	94
4.12	Position of the nanotubes in column 3 . . . . .	95
4.13	SEM images of funnel-shaped depressions around the nanotubes . . . . .	96
4.14	TEM images of the funnel-like depressions . . . . .	97
4.15	Composite image showing a possible nanotube fracture . . . . .	98
4.16	Images used for orientation calculations for column 6 . . . . .	102
4.17	Schematic drawing of the orientation calculations for column 6 . . . . .	103
4.18	Orientation of the TEM lamella of column 6 . . . . .	104
5.1	Sample with highly oriented CNTs before the electrodeposition . . . . .	107
5.2	Preferential deposition of Cu on nanotubes . . . . .	109
5.3	Samples with aligned CNTs after electrodeposition . . . . .	110
5.4	Nanotubes at cracks formed during electrodeposition . . . . .	112
5.5	Nanotubes at deformed regions . . . . .	113

---

5.6	Samples with tangled CNT-carpets . . . . .	114
6.1	Tensile test: sample dimensions and holder . . . . .	123
6.2	SEM images of the sample surfaces . . . . .	124
6.3	Crystals found after edging . . . . .	125
6.4	EDX-measurements from sample surface . . . . .	126
6.5	Small crystals at fracture surface . . . . .	127
6.6	Smoothness of the tensile test samples . . . . .	128
6.7	SEM images of sample with many nanotubes . . . . .	129
6.8	Cracking near fracture site . . . . .	130
6.9	Typical fracture surface of the tensile test samples . . . . .	131
6.10	Honeycomb structures on the fracture surface . . . . .	132
6.11	Copper protrusion in nanotube-free samples . . . . .	132
6.12	Cave-like openings in the fracture surface . . . . .	133
6.13	Layered structure of large gaps . . . . .	134
6.14	Bridging nanotubes . . . . .	135
6.15	Nanotubes not coated with metal . . . . .	136
6.16	Possible evidence for sword-in-sheath mechanism . . . . .	136
6.17	Coated nanotubes . . . . .	137
6.18	Stress-strain curves from the tensile tests . . . . .	138
6.19	Energy to failure and Young's modulus of the tensile test samples . .	139



# List of Tables

2.1	Literature values for Young's modulus of CNTs . . . . .	38
2.2	Properties of CNTs . . . . .	40
2.3	Fibers used in metal matrix composites . . . . .	50
2.4	Publications on MMCs reinforced with CNTs . . . . .	52
3.1	CN <sub>x</sub> -samples used in this study . . . . .	62
3.2	Parameters for DC-magnetron sputtering . . . . .	62
4.1	List of all columns evaluated . . . . .	80
4.2	Stacking fault energy of different materials . . . . .	92
6.1	Chemical composition of electrolyte . . . . .	120
6.2	Tensile samples fabricated by electrodeposition . . . . .	122
6.3	Energies of EDX peaks . . . . .	126



# Bibliography

- [1] S. Iijima. Helical microtubules of graphitic carbon. *Nature*, 354:56–58, 1991.
- [2] P. J.F. Harris. *Carbon Nanotubes and Related Structures: new materials for the 21st century*, chapter 4 - The physics of nanotubes, pages 111–151. Cambridge University Press, Cambridge, 1999.
- [3] K. Hata, N.D. Futaba, K. Mizuno, T. Namai, M. Yumura, and S. Iijima. Water-assisted highly efficient synthesis of impurity-free single-walled carbon nanotubes. *Science*, 306:1362–1364, 2004.
- [4] P. J.F. Harris. *Carbon Nanotubes and Related Structures: new materials for the 21st century*, chapter 3 - Structure, pages 61–110. Cambridge University Press, Cambridge, 1999.
- [5] C. Berger, Y. Yi, Z.L. Wang, and W.A. de Heer. Multiwalled carbon nanotubes are ballistic conductors at room temperature. *Applied Physics A*, 74:10.1007/s003390201279, 2002.
- [6] G.-Y. Xiong, D.Z. Wang, and Z.F. Ren. Aligned millimeter-long carbon nanotube arrays grown on single crystal magnesia. *Carbon*, 44:969–973, 2006.
- [7] M. Terrones. Science and technology of the twenty-first century; synthesis, properties and applications of carbon nanotubes. *Annu. Rev. Mater. Res.*, 33:419–501, 2003.
- [8] P. J.F. Harris. *Carbon Nanotubes and Related Structures: new materials for the 21st century*, chapter 2 - Synthesis: Preparation methods, growth mechanisms and processing techniques, pages 16–55. Cambridge University Press, 1999.

- [9] M. Endo, K. Takeuchi, S. Igarashi, M. Shiraishi, and H.W. Kroto. The production and structure of pyrolytic carbon nanotubes (PCNTs). *Journal of Physics and Chemistry of Solids*, 54:1841, 1993.
- [10] N. Grobert, M. Terrones, S. Trasobares, K. Kordatos, H. Terrones, J. Olivares, J. P. Zhang, Ph. Redlich, W. K. Hsu, C. L. Reeves, D. J. Wallis, Y. Q. Zhu, J. P. Hare, H. W. Kroto, and D. R. M. Walton. A novel route to aligned nanotubes and nanofibres using laser-patterned catalytic substrates. *Applied Physics A*, 70:175–183, 2000.
- [11] M. Mayne, N. Grobert, M. Terrones, R. Kamalakaran, M. Rühle, H. W. Kroto, and D. R. M. Walton. Pyrolytic production of aligned carbon nanotubes from homogeneously dispersed benzene-based aerosols. *Chemical Physics Letters*, 338:101–107, 2001.
- [12] R. Kamalakaran, M. Terrones, T. Seeger, Ph. Kohler-Redlich, M. Rühle, Y. A. Kim, T. Hayashi, and M. Endo. Synthesis of thick and crystalline nanotube arrays by spray pyrolysis. *Applied Physics Letters*, 77:3385–3387, 2000.
- [13] Y.-L. Li, I.A. Kinloch, and A.H. Windle. Direct spinning of carbon nanotube fibers from chemical vapor deposition synthesis. *Science*, 304:276–278, 2004.
- [14] R. T. K. Baker and P. S. Harris. The formation of filamentous carbon. *Chem. Phys. Carbon*, 14:83, 1978.
- [15] R.T.K. Baker and P.S Harris. *Chemistry and Physics of Carbon*, page 83. Dekker, New York, 1978.
- [16] S. Helveg, C. López-Cartes, J. Sehested, P.L. Hansen, B.S. Clausen, J.R. Rostrup-Nielsen, F. Abild-Pedersen, and J.K. Nørskov. Atomic-scale imaging of carbon nanofibre growth. *Nature*, 427:426–429, 2004.
- [17] Z. Xia, L. Riestler, W. A. Curtin, H. Li, B. W. Sheldon, J. Liang, B. Chang, and J. M. Xu. Direct observation of toughening mechanisms in carbon nanotube ceramic matrix composites. *Acta Materialia*, 52:931–944, 2004.



- [18] P. J.F. Harris. *Carbon Nanotubes and Related Structures: new materials for the 21st century*, chapter 6 - The ultimate carbon fibre? The mechanical properties of carbon nanotubes, pages 186–212. Cambridge University Press, 1999.
- [19] J.Y. Huang, S. Chen, Z.Q. Wang, L.K. Kempa, Y.M. Wang, S.H. Jo, G. Chen, M.S. Dresselhaus, and Z.F. Ren. Superplastic carbon nanotubes. *Nature*, 439:281, 2006.
- [20] M. M. J. Treacy, T. W. Ebbesen, and J. M. Gibson. Exceptionally high young's modulus observed for individual carbon nanotubes. *Nature*, 381:678–680, 1996.
- [21] E.W. Wong, P.E. Sheehan, and C.M. Lieber. Nanobeam mechanics: Elasticity, strength, and toughness of nanorods and nanotubes. *Science*, 277:1971–1975, 1997.
- [22] B. G. Demczyk, Y. M. Wang, J. Cumings, M. Hetman, W. Han, A. Zettl, and R. O. Ritchie. Direct mechanical measurement of the tensile strength and elastic modulus of multiwalled carbon nanotubes. *Materials Science and Engineering A*, 334:173–178, 2002.
- [23] J.-P. Salvetat, J.-M. Bonard, N. H. Thomson, A. J. Kulik, L. Forró, W. Benoit, and L. Zuppiroli. Mechanical properties of carbon nanotubes. *Applied Physics A*, 69:255–260, 1999.
- [24] M.-F. Yu, O. Lourie, M.J. Dyer, K. Moloni, T.F. Kelly, and R.S. Ruoff. Strength and breaking mechanism of multiwalled carbon nanotubes under tensile load. *Science*, 287:637–640, 2000.
- [25] A. Cao, P.L. Dickrell, W.G. Sawyer, M.N. Ghasemi-Nejhad, and P.M. Ajayan. Super-compressible foamlike carbon nanotube films. *Science*, 310:1307–1310, November 2005.
- [26] J.P. Lu. Elastic properties of carbon nanotubes and nanoropes. *Physical Review Letters*, 79:1297–1300, 1997.

- [27] K. M. Liew, X. Q. He, and C. H. Wong. On the study of elastic and plastic properties of multi-walled carbon nanotubes under axial tension using molecular dynamics simulation. *Acta Materialia*, 52:2521–2527, 2004.
- [28] B.T. Kelley. *Physics of Graphite*. Applied Science, 1981.
- [29] C. Wei, K. Cho, and D. Srivastava. Tensile strength of carbon nanotubes under realistic temperature and strain rate. *Physical Review B*, 67:115407, 2003.
- [30] Z. L. Wang, R. P. Gao, P. Poncharal, W. A. de Heer, Z. R. Dai, and Z. W. Pan. Mechanical and electrostatic properties of carbon nanotubes and nanowires. *Materials Science and Engineering C*, 16:3–10, 2001.
- [31] Weidian Shen and Bin Jiang. Investigation of the radial compression of carbon nanotubes with a scanning probe microscope. *Physical Review Letters*, 84:3634–3637, 2000.
- [32] O. Lourie, D. M. Cox, and H. D. Wagner. Buckling and collapse of embedded carbon nanotubes. *Physical Review Letters*, 81:1638–1641, 1998.
- [33] S. Zhang, S.L. Mielke, R. Khare, D. Troya, R.S. Ruoff, G.C. Schatz, and T. Belytschko. Mechanics of defects in carbon nanotubes: Atomistic and multiscale simulations. *Physical Review B*, 71:115403, 2005.
- [34] D.E. Soule and C.W. Nezbeda. Direct basal-plane shear in single-crystal graphite. *Journal of Applied Physics*, 39:5122–5139, 1968.
- [35] E. Bichoutskaia, A.M. Popov, A. El-Barbary, M. I. Heggie, and Y. E. Lozovik. Ab initio study of relative motion of walls in carbon nanotubes. *Physical Review B*, 71(11):113403, 2005.
- [36] E. Dujardin, T. W. Ebbesen, H. Hiura, and K. Tanigaki. Capillarity and wetting of carbon nanotubes. *Science*, 265:1850–1852, 1994.
- [37] T.W. Ebbesen. Wetting, filling and decorating carbon nanotubes. *Journal of Physics and Chemistry of Solids*, 57:951–955, 1996.

- [38] C.R. Barrett, W.D. Nix, and A.S. Tetelman. *The principles of engineering materials*, chapter Interfacial imperfections in solids, page 87. Prentice-Hall, Inc. Englewood Cliffs, New Jersey, 1973.
- [39] D. Ugarte, A. Chatelain, and W.A. deHeer. Nanocapillarity and chemistry in carbon nanotubes. *Science*, 274:1897–1899, 1996.
- [40] J.Y. Chen, A. Kutuna, C.P. Collier, and K.P. Giapis. Electrowetting in carbon nanotubes. *Science*, 310:1480–1483, 2005.
- [41] Y. Zhang, N.W. Franklin, R.J. Chen, and H. Dai. Metal coating on suspended carbon nanotubes and its implication to metal-tube interaction. *Chemical Physics Letters*, 331:35–41, 2000.
- [42] Z. Zhong, B. Liu, L. Sun, J. Ding, J. Lin, and K.L. Tan. Dispersing and coating of transition metals co, fe and ni on carbon materials. *Chemical Physics Letters*, 362:135–143, 2002.
- [43] A. Maiti and A. Ricca. Metal-nanotube interactions - binding energies and wetting properties. *Chemical Physics Letters*, 395:7–11, 2004.
- [44] F. Delannay, L. Froyen, and A. Deruyttere. The wetting of solids by molten metals and its relation to the preparation of metal-matrix composites. *Journal of Material Science*, 22:1–16, 1987.
- [45] W.-Q. Han, P. Kohler-Redlich, T. Seeger, F. Ernst, N. Grobert, W.-K. Hsu, B.-H. Chang, Y.-Q. Zhu, H.W. Kroto, D.R.M. Walton, M. Terrones, and H. Terrones. Aligned  $CN_x$  nanotubes by pyrolysis of ferrocene/ $C_{60}$  under  $NH_3$  atmosphere. *Applied Physics Letters*, 77:1807–1809, 2000.
- [46] C. H. Poa, S. R. P. Silva, P. C. P. Watts, W. K. Hsu, H. W. Kroto, and D. R. M. Walton. Field emission from nonaligned carbon nanotubes embedded in a polystyrene matrix. *Applied Physics Letters*, 80:3189–3191, 2002.
- [47] M. Reyes-Reyes, N. Grobert, R. Kamalakaran, T. Seeger, D. Golberg, M. Rühle, Y. Bando, H. Terrones, and M. Terrones. Efficient encapsulation

- of gaseous nitrogen inside carbon nanotubes with bamboo-like structure using aerosol thermolysis. *Chemical Physics Letters*, 396:167–173, 2004.
- [48] L.M. Cao, X.Y. Zhang, C. X. Gao, W.K. Wang, Z.L. Zhang, and Z. Zhang. High-concentration nitrogen-doped carbon nanotube arrays. *Nanotechnology*, 14:931–934, 2003.
- [49] M. He, S. Zhou, J. Zhang, Z. Liu, and C. Robinson. CVD growth of N-doped carbon nanotubes on silicon substrates and its mechanism. *Journal of Physical Chemistry B*, 109:9275–9279, 2005.
- [50] M. Terrones, R. Kamalakaran, T. Seeger, and M. Rühle. Novel nanoscale gas-containers: encapsulation of  $N_2$  in  $CN_x$  nanotubes. *Chemical Communications*, 23:2335–2336, 2000.
- [51] J. Kotakoski, A.V. Krasheninnikov, Y. Ma, A.S. Foster, K. Nordlund, and R.M. Nieminen. B and N ion implantation into carbon nanotubes: Insight from atomistic simulations. *Physical Review B*, 71:205408, 2005.
- [52] M. Terrones, P. M. Ajayan, F. Banhart, X. Blase, D. L. Carroll, J. C. Charlier, R. Czerw, B. Foley, N. Grobert, R. Kamalakaran, P. Kohler-Redlich, M. Rühle, T. Seeger, and H. Terrones. N-doping and coalescence of carbon nanotubes: synthesis and electronic properties. *Applied Physics A*, 74:355–361, 2002.
- [53] H.C. Choi, S.Y. Bae, J. Park, K. Seo, C. Kim, B. Kim, H.J. Song, and H.J. Shin. Experimental and theoretical studies on the structure of N-doped carbon nanotubes: Possibility of intercalated molecular  $N_2$ . *Applied Physics Letters*, 85:5742–5744, 2004.
- [54] A.H. Nevidomskyy, G. Csányi, and M.C. Payne. Chemically active substitutional nitrogen impurity in carbon nanotubes. *Physical Review Letters*, 91:105502, 2003.
- [55] Kuiyang Jiang, Ami Eitan, Linda S. Schadler, Pulickel M. Ajayan, and Richard W. Siegel. Selective attachment of gold nanoparticles to nitrogen-doped carbon nanotubes. *Nano Letters*, 3:275–277, 2003.

- [56] E.M. Kotsalis, E. Demostenous, J.H. Walther, S.C. Kassinos, and P. Koumoutsakos. Wetting of doped carbon nanotubes by water droplets. *Chemical Physics Letters*, 412:250–254, 2005.
- [57] T.H. Courtney. *Mechanical Behavior of Materials*, chapter 6 - Composite Materials, pages 244–292. McGraw-Hill, 2000.
- [58] T.H. Courtney. *Mechanical Behavior of Materials*, chapter 10 - Toughening Mechanisms and the Physics of Fracture, pages 454–521. McGraw-Hill, 2000.
- [59] Assessment of Metal Matrix Composites for Innovations. What are MMC's? Terminology and examples. <http://mmc-assess.tuwien.ac.at/2index.htm>, 2001.
- [60] P. Calvert. A recipe for strength. *Nature*, 399:210–211, 1999.
- [61] P. J. F. Harris. Carbon nanotube composites. *International Materials Reviews*, 49:31–43, 2004.
- [62] G. Oger. French firm hopes to get PR bounce out of nanotubes in tennis rackets. <http://www.smalltimes.com/>, 2001.
- [63] M. Cronin. Nanotennis anyone? Tiny, sporty materials have their day on court. <http://www.smalltimes.com/>, 2004.
- [64] R. Z. Ma, J. Wu, B. Q. Wei, J. Liang, and D. H. Wu. Processing and properties of carbon nanotubes-nano-SiC ceramic. *Journal of Material Science*, 33:5243–5246, 1998.
- [65] E. Flahaut, A. Peigney, Ch. Laurent, Ch. Marlière, F. Chastel, and A. Rousset. Carbon nanotube-metal-oxide nanocomposites: Microstructure, electrical conductivity and mechanical properties. *Acta Materialia*, 48:3803–3812, 2000.
- [66] J. Ning, J. Zhang, Y. Pak, and J. Guo. Fabrication and mechanical properties of SiO<sub>2</sub> matrix composites reinforced by carbon nanotube. *Materials Science and Engineering A*, 357:392–396, 2003.

- [67] T. Kuzumaki, O. Ujiie, H. Ichinose, and K. Ito. Mechanical characteristics and preparation of carbon nanotube fiber-reinforced Ti composite. *Advanced Engineering Materials*, 2:416–418, 2000.
- [68] Z. Bian, R.J. Wang, M.X. Pan, D.Q. Zhao, and W.H. Wang. Excellent wave absorption by zirconium-based bulk metallic glass composites containing carbon nanotubes. *Advanced Materials*, 15:616–621, 2003.
- [69] K. T. Kim, K. H. Lee, S. I. Cha, C.-B. Mo, and S. H. Hong. Characterization of carbon nanotubes/Cu nanocomposites processed by using nano-sized cu powders. *Mat. Res: Soc. Symp. Proc.*, 821:3.25.1–3.25.6, 2004.
- [70] A.I. Cha, K.T. Kim, S.N. Arshad, C.B. Mo, and S.H. Hong. Extraordinary strengthening effect of carbon nanotubes in metal-matrix nanocomposites processed by molecular-level mixing. *Advanced Materials*, 17:1377–1381, 2005.
- [71] C. Edtmaier and R. Haubner. Copper based carbon nanotube heat-sinks. In *Proceedings from the International Plansee Seminar*, 2005.
- [72] A.H. Chen, J.C. Peng, X.Q. Li, F.M. Deng, J.X. Wang, and W.Z. Li. Tribological behavior of carbon nanotubes-reinforced nickel matrix composite coatings. *Journal of Materials Science Letters*, 20:2057–2060, 2001.
- [73] X.H. Chen, F.Q. Cheng, S.L. Li, L.P. Zhou, and D.Y. Li. Electrodeposited nickel composites containing carbon nanotubes. *Surface & Coatings Technology*, 155:274–278, 2002.
- [74] W.X. Chen, J.P. Tu, L.Y. Wang, H.Y. Gan, Z.D. Xu, and X.B. Zhang. Tribological application of carbon nanotubes in a metal-based composite coating and composites. *Carbon*, 41:215–222, 2003.
- [75] X. Chen, G. Zhang, C. Chen, L. Zhou, S. Li, and X. Li. Carbon nanotube composite deposits with high hardness and high wear resistance. *Advanced Engineering Materials*, 5:514–518, 2003.

- [76] X. Chen, J. Xia, J. Peng, W. Li, and S. Xie. Carbon-nanotube metal-matrix composites prepared by electroless plating. *Composites Science and Technology*, 60:301–306, 2000.
- [77] Y.L. Shi, Z. Yang, M.K. Li, and H.L. Li. Preparation of electroplated Ni-P-ultrafine diamond, Ni-P-carbon nanotubes composite coatings and their corrosion properties. *Journal of Material Science*, 39:5809–5815, 2004.
- [78] S. Arai, M. Endo, and N. Kaneko. Ni-deposited multi-walled carbon nanotubes by electrodeposition. *Carbon*, 42:641–644, 2004.
- [79] H. Tang, J. Chen, S. Yao, L. Nie, Y. Kuang, Z. Huang, D. Wang, and Z. Ren. Deposition and electrocatalytic properties of platinum on well-aligned carbon nanotube (CNT) arrays for methanol oxidation. *Materials Chemistry and Physics*, 92:548–553, 2005.
- [80] S. R. Dong, J. P. Tu, and X. B. Zhang. An investigation of the sliding wear behaviour of Cu-matrix composite reinforced by carbon nanotubes. *Materials Science and Engineering A*, 313:83–87, 2001.
- [81] M. Werner. Nanotechnologie und Nanomaterialien - Applikationen und Marktpotential. Script to lecture at the symposium "Nano meets Umwelttechnik" organized by the Fraunhofer Institut für Arbeitswirtschaft und Organisation, Stuttgart, 2004.
- [82] M. D. Lay, J. P. Novak, and E. S. Snow. Simple route to large-scale ordered arrays of liquid-deposited carbon nanotubes. *Nano Letters*, 4:603–606, 2004.
- [83] M.D. Uchic, D.M. Dimiduk, J.N. Florando, and W.D. Nix. Sample dimensions influence strength and crystal plasticity. *Science*, 305:986–989, 2004.
- [84] D.M. Dimiduk, M.D. Uchic, and T.A. Parthasarathy. Size-affected single-slip behavior of pure nickel microcrystals. *Advanced Materials*, 53:4065–4077, 2005.
- [85] M.D. Uchic, D.M. Dimiduk, R. Wheeler, P.A. Shade, and H.L. Fraser. Application of micro-sample testing to study fundamental aspects of plastic flow. *Scripta Materialia*, 54:759–764, 2006.



- [86] J.R. Greer and W.D. Nix. Nanoscale gold pillars strengthened through dislocation starvation. *Physical Review B*, 73:245410, 2006.
- [87] C.A. Volkert and E.T. Lilleodden. Size-effects in the deformation of sub-micron Au columns. *Philosophical Magazine*, 2006. in press.
- [88] H. Zhang, B.E. Schuster, Q. Wei, and K.T. Ramesh. The design of accurate micro-compression experiments. *Scripta Materialia*, 54:181–186, 2006.
- [89] C. Frick. personal communication, september 2006.
- [90] A. Rohatgi, K.S. Vecchio, and G.T. Gray. The influence of stacking fault energy on the mechanical behavior of Cu and Cu-Al alloys: Deformation twinning, work hardening, and dynamic recovery. *Metallurgical and Materials Transactions A*, 32:135–145, 2001.
- [91] S. Kalidindi, A.A. Salem, and R.D. Doherty. Role of deformation twinning on strain hardening in cubic and hexagonal polycrystalline metals. *Advanced Engineering Materials*, 5:229–232, 2003.
- [92] T.H. Courtney. *Mechanical Behavior of Materials*, chapter 3.5 - Dislocations: Twinning, page 105. McGraw-Hill, 2000.
- [93] A. Wanner and G. Garcés. Creep of multidirectionally reinforced composites. *Philosophical Magazine A*, 84:3019–3038, 2004.
- [94] A. Wanner and E. Arzt. *Damage and its Evolution in Fiber-Composite Materials: Simulation and Non-Destructive Evaluation*, chapter Short Fiber Reinforced Metal Matrix Composites - Investigations by Acoustic Emission and Neutron Diffraction., pages 193–202. ISD Verlag, 2006.
- [95] C. Thompson and G. Nessim. Personal communication, may 2006.
- [96] D. Qian, E.C. Dickey, R. Andrews, and T. Rantell. Load transfer and deformation mechanisms in carbon nanotube-polystyrene composites. *Applied Physics Letters*, 76:2868–2870, 2000.

- [97] O. Lourie and H.D. Wagner. Transmission electron microscopy observations of fracture of single-wall carbon nanotubes under axial tension. *Applied Physics Letters*, 73:3527–3529, 1998.
- [98] R. Woldseth. *X-Ray Energy Spectroscopy*. Kevex Corporation, Burlingame, CA, 1973.
- [99] W.A. Spitzig, D.T. Peterson, and F.C Laabs. Effect of hydrogen on the mechanical properties of a deformation processed Cu-20% Nb composite. *Journal of Material Science*, 26:2000–2006, 1991.
- [100] J. Cumings and A. Zettl. Low-friction nanoscale linear bearing realized from multiwall carbon nanotubes. *Science*, 289:602–604, 2000.
- [101] S. Orso, U. G. K. Wegst, C. Eberl, and E. Arzt. Micrometer-scale tensile testing of biological attachment devices. *Advanced Materials*, 18:874–877, 2006.
- [102] C. Motz, T. Schöberl, and R. Pippan. Mechanical properties of micro-sized copper bending beams machined by the focused ion beam technique. *Advanced Materials*, 53:4269–4279, 2005.

